

Material Matters™

Volume 11, Number 1

ALDRICH
Materials Science

Next Generation Nanomaterials for Energy and Electronics

Nanomaterials—Making Big Advances

RECENT ADVANCES IN
HYBRID HALIDE PEROVSKITES-BASED SOLAR CELLS

GRAPHENE AND OTHER 2D CRYSTALS
FOR RECHARGEABLE BATTERIES

NANOSTRUCTURED OLIVINE-BASED CATHODE MATERIALS
FOR LITHIUM-ION BATTERIES

AGGREGATION-INDUCED EMISSION LUMINOGENS
FOR NON-DOPED ORGANIC LIGHT-EMITTING DIODES

Introduction

Welcome to the first issue of *Material Matters*™ for 2016, focusing on Next Generation Nanomaterials for Energy and Electronics.

In the last decade, developments in nanotechnology have been fueled by significant advances in nanomaterials fabrication and synthesis as well as promising application data for the biomedical, electronics, and energy fields. Nanomaterials technology has the potential to address a number of today's biggest scientific challenges, ranging from the need for more efficient alternative energy technologies, faster and flexible electronics, and improved disease diagnosis and treatment. The unique properties of nanomaterials include large surface-to-volume ratios, favorable conductivity, unique optical and confinement effects, as well as many others. These characteristics have been extensively studied for energy- and electronics-related applications, in particular for use in solar cells, lithium-ion batteries, supercapacitors, lighting, and printed and flexible electronics. While in principle nanomaterials hold enormous potential to improve performance and lower costs in various devices, the full realization of such benefits has yet to be achieved in many cases. In order to realize the full potential of the nanomaterial revolution, a better understanding of the fundamental processes associated with energy conversion and storage and electron transport processes, as well as solutions to more practical challenges such as device integration and cost-effective large-scale production is still needed. In this edition of *Material Matters* both the fundamental and practical challenges involved in the development of nanomaterials are reflected.

In our first article, Prof. Michael Grätzel (Swiss Federal Institute of Technology at Lausanne, EPFL, Switzerland) provides an historical perspective on the rapid development of perovskite solar cells from a curiosity to a potential disruptor of silicon-based solar cell technologies. The article highlights the various milestones in the rapid development of perovskite solar cells, outlines several different approaches to the technology, and discusses the challenges to scale-up, manufacture, and commercialization of these devices.

Prof. Francesco Bonaccorso (Istituto Italiano di Tecnologia, Italy), in the second article, provides a brief review of 2D nanomaterials (graphene and inorganic 2D crystals) that show promise for use in energy storage systems. The authors describe the potential of these materials, both as functional composites and on their own, in improving the performance of lithium-ion batteries. The article relates how these materials increase energy and power densities, cyclability, and reduce cost, as well as enable the development of next-generation batteries such as lithium-air and flexible batteries.

Prof. Palani Balaya (National University of Singapore, Singapore) highlights, in the third article, the impact of nanostructuring and introduces methods for producing conductive carbon wiring on the surface of nanostructured cathode material for improving the electrochemical performance of lithium-ion batteries. The authors also present a scalable synthesis method for nanostructured olivine-type cathode materials.

In the final article, Prof. Ben Zhong Tang (South China University of Technology, China) demonstrates the application of thin films of luminescent organic semiconductors for fabrication of organic light emitting diodes (OLEDs) and next-generation electronic devices. The article describes the unique phenomena of aggregation-induced emission (AIE) and how it addresses problems caused by fluorescence quenching and creates new avenues for developing efficient solid-state emitters. Luminogens exhibiting AIE characteristics are used to fabricate stable and efficient non-doped OLEDs and also high-performance white OLEDs.

As always, each article in this publication is accompanied by a list of relevant materials available from Aldrich® Materials Science. For additional product information, visit us at aldrich.com/matsci. Please bother us with your new product suggestions, as well as thoughts and comments for *Material Matters*™ at matcsi@sial.com.

About Our Cover

Sustainable energy generation and storage is a preeminent challenge for the 21st century. Materials scientists are now focusing much of their efforts on the nano-scale to identify and develop groundbreaking solutions. The unique electronic, optical, and bioactive properties of nanomaterials make them an important class of materials for addressing our growing energy and environmental challenges. The cover art for this issue is a conceptual image of nanomaterials as a central component of a dynamic energy flow.



Bryce P. Nelson, Ph.D.
Aldrich Materials Science
Initiative Lead

Material Matters™

Vol. 11, No. 1

**Aldrich Materials Science
Sigma-Aldrich Co. LLC**
6000 N. Teutonia Ave.
Milwaukee, WI 53209, USA

To Place Orders

Telephone 800-325-3010 (USA)
FAX 800-325-5052 (USA)

International customers, contact your local Sigma-Aldrich office
(sigma-aldrich.com/worldwide-offices).

Customer & Technical Services

Customer Inquiries	800-325-3010
Technical Service	800-325-5832
SAFC®	800-244-1173
Custom Synthesis	800-244-1173
Flavors & Fragrances	800-227-4563
International	314-771-5765
24-Hour Emergency	314-776-6555
Safety Information	sigma-aldrich.com/safetycenter
Website	aldrich.com
Email	aldrich@sial.com

Subscriptions

Request your **FREE** subscription to *Material Matters*:

Phone	800-325-3010 (USA)
Mail	Attn: Marketing Communications Aldrich Chemical Co., Inc Sigma-Aldrich Co. LLC P.O. Box 2060 Milwaukee, WI 53201-2060
Website	aldrich.com/mm
Email	sams-usa@sial.com

Online Versions

Explore previous editions
of *Material Matters* aldrich.com/materialmatters



Available for your iPad®
aldrich.com/mm

Material Matters (ISSN 1933-9631) is a publication of Aldrich Chemical Co., Inc. Aldrich is a member of the Sigma-Aldrich Group.

©2016 Sigma-Aldrich Co. LLC. All rights reserved. SIGMA, SAFC, SIGMA-ALDRICH, ALDRICH and SUPELCO are trademarks of Sigma-Aldrich Co. LLC, registered in the US and other countries. Material Matters is a trademark of Sigma-Aldrich Co. LLC. Dyesol is a registered trademark of Dyesol Ltd. iPad is a registered trademark of Apple Inc. Sigma-Aldrich, Sigma, Aldrich, Supelco, and SAFC brand products are sold by affiliated Sigma-Aldrich distributors. Purchaser must determine the suitability of the product(s) for their particular use. Additional terms and conditions may apply. Please see product information on the Sigma-Aldrich website at www.sigmaaldrich.com and/or on the reverse side of the invoice or packing slip. Sigma-Aldrich Corp. is a subsidiary of Merck KGaA, Darmstadt, Germany.

Table of Contents

Articles

Recent Advances in Hybrid Halide Perovskites-based Solar Cells	3
Graphene and Other 2D Crystals for Rechargeable Batteries	15
Nanostructured Olivine-based Cathode Materials for Lithium-ion Batteries	23
Aggregation-induced Emission Luminogens for Non-doped Organic Light-emitting Diodes	29

Featured Products

Quantum Dots A selection of core-type, core-shell type and alloyed quantum dots	11
Precursors for Organometallic Perovskites A list of high purity perovskites precursors for photovoltaic	12
Titania Nanomaterials for Support A selection of titanium nanomaterials for photovoltaics	13
Inorganic 2D Materials A selection high quality 2D crystals	13
Organic Hole Transport Materials A selection of hole transport small organic materials and polymers	14
Hole Conductor Cobalt Dopants A list of cobalt-based dopants for use in solar cell applications	14
Fluorine-doped Tin Oxide Coated Glass Slides A list of FTO slides	14
Graphene A list of graphene materials and graphene based nanoplatelets, nanoribbons, inks, films, and field effect transistor chips	20
Reduced Graphene Oxides and Graphene Oxides A selection of reduced graphene oxide, graphene oxide, and their derivatives	21
Graphene Nanocomposites A list of graphene-based and reduced graphene oxide-based nanocomposite materials	22
Electrode Materials A selection of ready-to-use electrode sheets and electrode materials for LIBs	25
Electrolyte Solutions Ready-to-use electrolytes for LIBs	26
Electrolyte Materials A selection of high purity electrolyte materials for LIBs	27
Solvents and Additives A selection of high-purity and anhydrous solvents and additives for LIBs	27
Aggregation-induced Emission Luminogens A selection of AIE luminogens and their application	33
Hole Transport/Injection Layer Materials A selection of hole transport materials and injection layer materials	34
Electron Transport/Injection Layer Materials A selection of electron transport materials and injection layer materials	37

Your Materials Matter



J. Zihlmann

Josef Zihlmann
Head, Lab and Specialty Chemicals
Research Solutions Strategic Marketing & Innovation
MilliporeSigma

We welcome fresh product ideas. Do you have a material or compound you wish to see featured in the Aldrich® Materials Science line? If it is needed to accelerate your research, it matters. Send your suggestion to matsci@sial.com for consideration.

Prof. Michael Grätzel and Dr. Shaik M. Zakeeruddin of the Swiss Federal Institute of Technology at Lausanne (EPFL) recommended the addition of FK209 Co(III) TFSI (Prod. No. 805394) to our catalog for use as a p-dopant in photovoltaic devices. The FK209 Co(III) TFSI dopant is part of a newly reported class of p-type dopants based on cobalt (III) polypyridyl complexes for organic hole transport materials (HTMs).^{1,2}

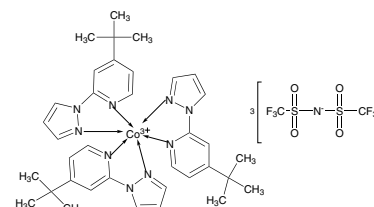
To attain p-type doping of the bulk HTM, deposition of the dopant together with the hole conductor is required. These materials are designed to be processed from solution and are particularly interesting due to their ambient stability, ease of preparation, and tunability of their chemical and physical properties.¹ A key factor for efficient doping is the electron affinity, or ionization potential position of the dopant with respect to the energy levels of the host material. As a p-type dopant, FK209 can be efficiently used to dope a triarylamine-based HTM such as 2,2',7',7'-tetrakis(*N,N*-di-*p*-methoxyphenylamine)-9,9'-spirobifluorene (spiro-MeOTAD, Prod. No. 792071), a hole-transporter commonly used in solid-state dye-sensitized solar cells (ssDSCs),¹⁻² organic-inorganic hybrid perovskite solar cells (PSCs),¹⁻⁴ and potentially in OLEDs⁵ and novel photoamplifiers.⁶ The use of the p-dopant FK209 Co(III) TFSI has been shown to increase the conductivity of spiro-MeOTAD, which contributes to enhanced performance of photovoltaic devices by increasing the fill factor and charge collection efficiency.

References

- (1) Burschka, J.; Dualeh, A.; Kessler, F.; Baranoff, E.; Cevey-Ha, N.-L.; Yi, C.; Nazeeruddin, M.; and Grätzel, M. *J. Am. Chem. Soc.* **2011**, *133*, 18042.
- (2) Burschka, J.; Kessler, F.; Nazeeruddin, M.; and Grätzel, M. *Chem. Mater.* **2013**, *25*, 2986–299.
- (3) Burschka, J.; Pellet, N.; Moon, S.-J.; Humphry-Baker, R.; Gao, P.; Nazeeruddin, M.; and Grätzel, M. *Nature.* **2013**, *499*, 316.
- (4) Bi, D. et al. *Sci. Adv.* **2016**, *2*; doi: 10.1126/sciadv.1501170.
- (5) Fantacci, S.; De Angelis, F.; Nazeeruddin, M.; and Grätzel, M. *J. Phys. Chem. C.* **2011**, *115*, 23126–23133.
- (6) Moehl, T. et al. *J. Phys. Chem. Lett.* **2014**, *5*, 3931–3936.

FK 209 Co(III) TFSI salt

C₄₂H₄₅CoF₁₈O₁₂N₁₂S₆
FW 1503.17



tris(2-(1*H*-pyrazol-1-yl)-4-*tert*-butylpyridine)cobalt(III)
tri[bis(trifluoromethane)sulfonimide] 98%

powder

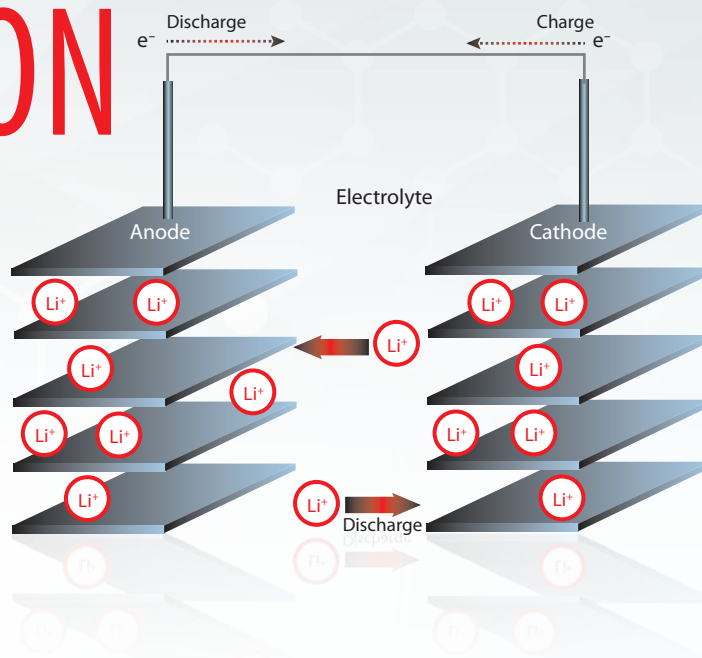
Product of Dyesol®

mp 281.5 °C (exp.)

805394-5G

5G

MAKE YOUR OWN LITHIUM-ION BATTERIES



Applications of lithium-ion batteries (LIBs) extend from modern electronics to automobiles. Order ready-to-use electrolyte solutions and electrode sheets in battery grade to fabricate your LIB.

Electrolyte Solutions

Name	Specifications	Prod. No.
2.0 M LiPF ₆ in EC/DMC=50/50 (v/v)	in ethylene carbonate and dimethyl carbonate, battery grade	809357
2.0 M LiPF ₆ in EC/EMC=50/50 (v/v)	in ethylene carbonate and ethyl methyl carbonate, battery grade	809365
2.0 M LiPF ₆ in EC/DEC=50/50 (v/v)	in ethylene carbonate and diethyl carbonate, battery grade	809349
2.0 M LiPF ₆ in DMC	in dimethyl carbonate, battery grade	809411
2.0 M LiPF ₆ in EMC	in ethyl methyl carbonate, battery grade	809403
2.0 M LiPF ₆ in DEC	in diethyl carbonate, battery grade	809543
2.0 M LiPF ₆ in PC	in propylene carbonate, battery grade	809470

Electrode Sheets

Name	Specifications	Composition	Prod. No.
Lithium nickel manganese cobalt oxide	aluminum substrate, size 5 in. x 10 in., loading >80%, thickness 25–50 μm	LiNi _{0.33} Mn _{0.33} Co _{0.33} O ₂	765163
Lithium nickel cobalt aluminum oxide	aluminum substrate, size 5 in. x 10 in., loading >80%, thickness 12–25 μm	LiNi _{0.8} Co _{0.15} Al _{0.05} O ₂	765171
Lithium manganese nickel oxide	aluminum substrate, size 5 in. x 10 in., loading >80%, thickness 25–50 μm	Li ₂ Mn ₂ NiO ₈	765198
Lithium manganese oxide	aluminum substrate, size 5 in. x 10 in., loading >80%, thickness 25–40 μm	LiMn ₂ O ₄	765201
Lithium titanate spinel	aluminum substrate, size 5 in. x 10 in., loading >80%, thickness 25–50 μm	Li ₄ Ti ₅ O ₁₂	765155

For a complete list of LIB materials, including electrode powders, electrolytes, solvents and additives, visit aldrich.com/lib

RECENT ADVANCES IN HYBRID HALIDE PEROVSKITES-BASED SOLAR CELLS



Kuppuswamy Kalyanasundaram, Shaik. M. Zakeeruddin, Michaël Grätzel*
Laboratory for Photonics and Interfaces (LPI)
Swiss Federal Institute of Technology at Lausanne (EPFL)
1015 Lausanne, Switzerland
*Email: michael.gratzel@epfl.ch

Introduction

For several decades, the need for an environmentally sustainable and commercially viable source of energy has driven extensive research aimed at achieving high efficiency power generation systems that can be manufactured at low cost. Photovoltaic solar cells allow for the direct conversion of solar radiation to electricity using light absorbers, and recent advances in solar conversion technology have convinced many researchers that it may finally be delivering on its promise. Solar cells can be divided into three main categories based on the morphology of the light absorbers and on the device configuration.¹ First- and second-generation solar cell devices include wafer-based silicon devices and thin film solar cells made from cadmium telluride (CdTe) or copper-indium-gallium-selenide (CIGS). The technology used in these devices is considered mature and many large area modules and panels are already commercially available. These systems deliver at least 15–18% solar power conversion efficiency (PCE) with a guaranteed performance lifetime of at least 20 years. Third-generation thin film solar cells use recent advances in nanoscience and technology in order to fabricate more efficient materials and devices using low-cost solution processing methods at ambient conditions.

Devices using wide bandgap semiconductors sensitized with organic or inorganic dye molecules have attracted considerable research interest over the past two decades.² However, the use of monolayer films of adsorbed dyes resulted in limited light absorption and caused the PCE of dye-sensitized solar cells (DSSC) to be very poor (<1%). Sol-gel chemistry permits the preparation of mesoporous oxide semiconductor thin films with controllable optical and electronic properties using synthesis of the targeted colloidal semiconductor. In 1991, O'Regan and Grätzel³ proposed use of the mesoporous semiconducting form of titania (TiO₂) as a high surface area scaffold to deposit the dye in order to improve the PCE of dye-sensitized solar cells (DSSC). This new concept generated a surge in the development of DSSCs. Two device configurations of DSSCs have been studied and optimized: liquid electrolyte DSSCs where a redox electrolyte such as (I⁻/I₃⁻) present in an organic solvent functions as an electron-transfer shuttle between the counter-electrode and the photoanode, and a solid-state version of DSSC (ss-DSSC) where an organic hole transport material (HTM) is incorporated into the mesoporous oxide

layer carrying the semiconductor and plays the role of the redox shuttle. To date, the highest reported solar-to-electric PCE is approximately 14.3%;⁴ a number of DSSC-based commercial products are already available.

Early Reports on Perovskites Solar Cells (PSC)

Perovskites are a group of structurally related materials with the generic formula ABX₃ (**Figure 1**) where A, B, and X stand for an organic cation, metal cation, and a halide anion, respectively. For example, A = Cs⁺, CH₃NH₃⁺ (MA), or NH=CHNH₂⁺ (FA); B = Pb or Sn; and X = Br, I. The perovskite family of oxides such as CaTiO₃ has been known since 1893.^{5a} In 1957, Christian Møller investigated the photoconductivity of alkali-metal mixed halides such as CsPbX₃ (X= Cl, Br or I) and noted their semiconducting behavior.^{5b} Later, Weber reported that organic analogs of ABX₃, where A is an alkylammonium cation and B = Sn(II) or Pb(II) also form perovskites that exhibit interesting optical and electronic properties.^{5c} David Mitzi provided a comprehensive review of this topic.^{5d} By varying the alkyl chain length of the organic cation, it is possible to derive a series of organo-lead perovskites with highly tunable properties, including the optical absorption bandgap.

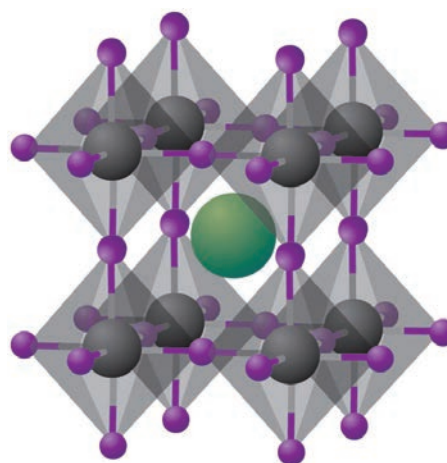


Figure 1. Cuboid structure of the hybrid halide perovskites of the type ABX₃. The organic or inorganic cations occupy position A (green), whereas metal cations and halides occupy the B (grey) and X (purple) positions, respectively.

In 2009, Kojima and Miyasaka⁶ suggested the use of the perovskite methylammonium-lead triiodide, CH₃NH₃PbI₃ (MAPI, **Prod. No. 793833**), as a photosensitizer for liquid electrolyte-based DSSCs. Lead-halide perovskites were prepared *in situ* by mixing the precursors lead halide and alkyl ammonium salts in an organic electrolyte, resulting in a low PCE of 3.8%. By varying the electrolyte composition and method of deposition, Park et al.⁷ reported improved device stability and a PCE of 6.5%, further indicating the potential of halide-perovskite photosensitizers.

Within a year of the initial advances in performance and stability of liquid-electrolyte perovskite DSSCs, a solid-state version of perovskite solar cells was reported. This new configuration used CsSnI₃⁸ and 2,2,7,7-tetrakis(*N,N*-di-*p*-methoxyphenylamine)-9,9-spirobifluorene⁹ (spiro-OMeTAD, **Prod. No. 792071**) as HTM and resulted in an increase in PCE to 9.7% with further substantial improvement in the PSC stability. Based on these results, many laboratories across the globe took keen interest in further studying this configuration, and within a span of six years the PCE of perovskite-based solar cells (PSCs) with a typical layout of FTO/c-TiO₂/meso-TiO₂/perovskite/HTM/CE rapidly increased from roughly 4% to 21%.¹⁰ In this short review we shall attempt to capture the key points in the remarkable improvement in the performance of PSCs. Discussions here will focus on the research work carried out in our own laboratories in Lausanne. For a more in-depth discussion, we recommend a number of recent reviews of PSC development.¹¹

Materials and Preparation

Three halide perovskites and their variants have been found to be efficient light absorbers: MAPI, formamidinium iodide (FAI) and the mixed halides (FA,MA)PbI₃ (FAMAPI). Of these, MAPI shows a bandgap of 1.55–1.59 eV and FAI shows a bandgap of 1.45 eV. Organic-inorganic halide perovskites have several attractive features for use as light absorbers in solar cells: e.g., strong light absorption, long charge carrier lifetime (exceeding 300 ns), diffusion lengths exceeding 1 μm for electrons and holes, photoluminescence quantum efficiency as high as 70%, and ambipolar charge transport capability. Unless stated otherwise, the perovskite discussed in this paper refers to MAPI.

A very appealing feature of organic halide perovskites is their facile *in situ* synthesis directly on a substrate. The hybrid perovskite forms readily upon the mixing of the precursors lead halide and the alkylammonium halide in a suitable organic solvent such as dimethylformamide (DMF) under mild warm conditions. As in any sol-gel nanoparticle synthesis, considerable tunability of the electronic and morphological properties of the perovskite can be obtained by varying the synthetic conditions: e.g., the nature of the solvent, concentration of the lead salt and mixing ratio of the precursors, presence of other additives, deposition temperature, and post-annealing steps.

Three different experimental protocols have been used to prepare the perovskite layer on the substrate (as planar layers or on mesoporous oxide layers used as scaffolds): a) single step deposition using pre-mixed solutions of the reactants MAI and PbI₂ in solvents such as γ -butyrolactone, DMF or DMSO;⁹ b) sequential or 2-step deposition of PbX₂ by spin coating followed by immersion in the solution of MAI in suitable organic solvents;¹² and c) vapor phase deposition of the reactants.¹³ A hybrid approach combining the solution-processing and vacuum-based methods has also been used to obtain thermodynamically stable compact films with well-defined grains. Each method has its own merits, yielding PSC with high PCE >15%. MAPI is formed readily in a few seconds and can fully infiltrate the mesoporous oxide scaffolds. Near quantitative absorption of the visible light can be achieved with ca. 400–600 nm thick perovskite layers. Regardless of which approach is ultimately used, the strong potential for cost-effective scale and manufacture of PSC technology is one of many highly appealing aspects of PSC technology.

Device Configurations

To date, the highest performing perovskite solar cells now use a high surface area mesoporous TiO₂ layer as a scaffold to enhance the deposition of the perovskite light absorber. In view of the very strong absorption coefficient of hybrid halide perovskites in the visible region, the oxide layer can be substantially thinner than that used for liquid electrolyte DSSCs (150–400 nm vs. \approx 10 μm in liquid-electrolyte DSSC and

\approx 2 μm in ss-DSSC). Mesoporous TiO₂ serves as a large area scaffold for the uniform infiltration of the perovskite and also as an electron-transport layer (ETL) that collects and passes photogenerated electrons to the fluorine-doped tin oxide (FTO) collector electrode. PSC with the layout FTO/c-TiO₂/meso-TiO₂-MAPI/MAPI/spiro-OMeTAD/Au can be considered an n-i-p photovoltaic device with an operating mechanism similar to ss-DSSC. Upon light absorption by the halide perovskite, electrons are injected in the mesoporous layer where they percolate and eventually reach the collector electrode. The holes (h⁺) hop through the hole-conducting material layer to reach the Au or Ag cathode.

An important property of hybrid halide perovskites is the ambipolar nature of charge carrier transport. Here, both electrons and holes exhibit very good mobility, and efficient PSCs can be fabricated even without the use of an HTM. Two experimental results support this concept. Etgar et al.¹⁴ found that solar cells made solely with the meso-TiO₂/MAPI heterojunction (without any HTM layer deposition) also show a moderate PCE of 5.5%. Snaith and co-workers¹⁵ showed that a PSC made with the wider bandgap mesoporous oxide Al₂O₃ can achieve a satisfactory PCE as well. Both results can be rationalized only in a model where the photogenerated holes and electrons migrate efficiently to the collector (Au, TiO₂) electrode, even without passing through the hole or electron-transport layer such as spiro-OMeTAD and TiO₂.

In an important study, Liu and Kelly¹⁶ found that a thin layer of ZnO under a planar halide perovskite layer is sufficient to construct a high performing solar cell using the configuration FTO/ZnO ETL/planar MAPI/spiro-OMeTAD/Au. Even in the absence of a mesoscopic oxide scaffold to aid uniform distribution of the perovskite absorber, the PSC showed a PCE of 15.7% under standard AM1.5 light conditions. Several studies¹⁷ have established that halide perovskites exhibit unusually long diffusion lengths, reaching over 100 nm for MAPI, about 1,000 nm for “MAPI_{3-x}Cl_x” absorber layers, and even up to 175 μm for single crystals of MAPI. The long charge carrier diffusion length renders perovskites effective as planar absorber layers. However, somewhat disconcertingly, ZnO layers have also been associated with thermal decomposition of perovskites. For example, while perovskite films deposited onto ZnO appear to be stable up to temperatures of 120 °C for short periods with little change in the absorption spectrum, the film decomposes into a yellow-colored byproduct upon heating at 100 °C for a prolonged period or even for short periods when heated to 150 °C. The absorption spectrum of these decomposed films is consistent with that of PbI₂.

Snaith et al.¹⁸ first reported on an “inverted PSC design” (p-i-n architecture) using a number of organic HTM (PEDOT:PSS, V₂O₅ and NiO) in a solar cell with the layout FTO/PEDOT:PSS/MAPI_{3-x}Cl_x/PCBM/TiO₂/Al. While in this configuration, holes are collected at the front transparent glass electrode via the HTM layer, electrons are collected via the ETL at the top counter electrode. In the p-i-n type devices, photocurrent flows in the reverse direction (photoinduced holes instead of electrons collected through the front conductive glass substrate) and hence the name “inverted structure.” In the initial work, the PSC with PEDOT:PSS showed a PCE of 10% on glass substrates and 6% on flexible polymer substrates. Since the initial studies, the PCE has been improved to 18%.^{17d}

Four Main Solar Cell Design Layouts

During the past three years there have been several hundred reports of solar cells fabricated using halide perovskites. Based on the components and their layout, PSCs can be broadly divided into the following four categories: a) those based on mesoporous TiO₂ or similar scaffolds (labeled mesoporous-active); b) those based on mesoporous Al₂O₃ scaffolds or similar oxides (labeled as mesoporous-passive or mesoporous-superstructure); c) those based on planar absorber layers with electron-transport layer deposited on the transparent FTO/ITO (n-i-p type, labeled as planar-regular); and d) those based on an inverted layout where the

hole-transport layer is deposited on FTO/ITO anode (labeled as planar-inverted). Typical device layout of these four categories are shown in Figure 2.

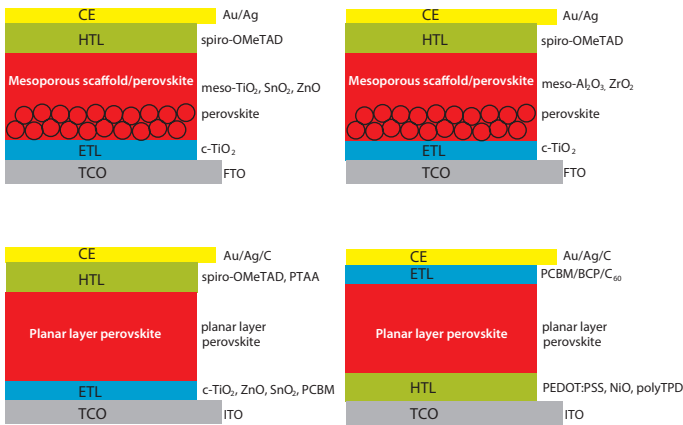


Figure 2. Schematic representation of the four main configurations of perovskite solar cells. **A)** Mesoporous-active: FTO/c-TiO₂/mesoTiO₂/perovskite/HTL/CE (Au or Ag). **B)** Mesoporous-passive: FTO/c-TiO₂/meso Al₂O₃/perovskite/HTL/CE (Au or Ag). **C)** Planar-regular: ITO/c-TiO₂(ETL)/planar perovskite/HTL/CE (Au or Ag). **D)** planar-inverted: ITO/HTL (PEDOT:PSS)/planar perovskite/ETL (PCBM-C₆₀)/Ag.

PSC devices based on mesoporous oxide scaffolds and compact-TiO₂ layers require high temperature processing, typically >400 °C. This, in turn, requires the use of rather expensive FTO in the transparent electrode. Hence, there has been a sustained search for designs that use inexpensive oxides such as ZnO to allow processing at lower temperatures (≤150 °C) or those that use low-temperature, processable organic electron- and hole-transport materials. Solar cells with planar perovskite layers (planar-regular and planar-inverted) use low cost indium-doped tin oxide (ITO) electrodes. **Tables 1 and 2** show data from the best performing perovskite solar cells that use mesoscopic active and passive scaffolds with PCE >15% reported in the past two years.^{19–22} The highest PCE (20.8%) was obtained using a mesoporous TiO₂-based PSC based on a mixed cation mixed-halide perovskite film prepared in a single step from a solution of FAI, PbI₂, MABr, and PbBr₂ in a mixed solvent containing dimethyl formamide (DMF) and dimethyl sulfoxide (DMSO). To date, PSCs with the structure (Au/spiro-OMeTAD/perovskite/meso-TiO₂/c-TiO₂/FTO) deliver the highest photocurrent and photovoltage, also with minimal hysteresis.

Table 1. Data highlighting several high-performing perovskite solar cells that use mesoporous scaffold layers

Cell Layout	V _{oc} (V)	I _{sc} (mA/cm ²)	FF	PCE (%)	Ref.
Cell Type: Meso-ETL					
ITO/c-TiO ₂ /mesoTiO ₂ /MA-FAPIBr/spiroOMeTAD/Au	1.16	24.6	0.73	20.8	19a
ITO/c-TiO ₂ /mesoTiO ₂ /FAPI/PTAA/Au	1.06	24.7	0.775	20.1	19b
FTO/cTiO ₂ /mesoTiO ₂ /MAPI/spiroOMeTAD/Ag	1.086	23.83	0.76	19.71	19c
FTO/c-TiO ₂ /mesoTiO ₂ -MAPI/spiroOMeTAD/Au	1.094	21.21	0.78	18.36	19d
FTO/c-TiO ₂ /mesoTiO ₂ /MAPI/spiroOMeTAD/Au	1.06	21.39	0.76	17.19	19e
ITO/c-TiO ₂ /mesoTiO ₂ -MAPI/MAPI/spiroOMeTAD/Au	1.056	21.64	0.74	17.01	19f
FTO/c-TiO ₂ /mesoTiO ₂ -MAPI/MAPI/V886/Au	1.085	21.38	0.73	16.91	19d
FTO/c-TiO ₂ /mesoTiO ₂ -MAPI/spirom-mp/Au	1.02	21.2	0.78	16.7	19g
FTO/c-TiO ₂ /mesoTiO ₂ /MAPI/CW4spiro/Au	1.05	21.75	0.72	16.56	19o
FTO/c-TiO ₂ /mesoTiO ₂ -MAPI/azuleneHTM/Au	1.08	21.7	0.71	16.5	19p
FTO/c-TiO ₂ /mesoTiO ₂ /MAPI-Br/PTAA/Au	1.09	19.50	0.76	16.22	19i
FTO/amor-TiO ₂ /MAPICl/spiroOMeTAD/Au	1.03	21.68	0.72	16.08	19h
FTO/c-TiO ₂ /FAPI-MAPI/spiroOMeTAD/	1.03	20.97	0.74	16.01	19q
FTO/c-TiO ₂ /mesoTiO ₂ -MAPI (Zrac2)/spiroOMeTAD/Au	1.02	20.1	0.76	15.6	19j
FTO/c-TiO ₂ /mesoTiO ₂ -MAPI/OMeTAD/Au	1.00	20.4	0.74	15.2	19g
FTO/cTiO ₂ /mesoTiO ₂ -MAPI/spiroOMeTAD/Au	0.993	20.0	0.73	15.0	19l
FTO/c-TiO ₂ /mesoTiO ₂ -MAFAPI/spiroOMeTAD/Au	1.03	21.2	0.70	14.9	19m

Cell Layout	V _{oc} (V)	I _{sc} (mA/cm ²)	FF	PCE (%)	Ref.
FTO/c-TiO ₂ /mesoTiO ₂ /MAPI/CuSCN/Au	1.02	19.7	0.62	12.4	19n
Cell Type: Meso-SS					
FTO/c-TiO ₂ /mesoAl ₂ O ₃ /MAPICl/spiroOMeTAD/Ag	1.02	21.5	0.71	15.9	20a
FTO/c-TiO ₂ /mesoAl ₂ O ₃ -IPFB-perov/spiro+buffer/Au	1.03	20.62	0.62	13.07	20b
FTO/c-TiO ₂ /mesoAl ₂ O ₃ /MAPICl/spiroOMeTAD/Ag	1.02	18.0	0.67	12.3	20c
FTO/c-TiO ₂ /mesoZrO ₂ /MAPI/spiroOMeTAD/Au	1.07	17.3	0.59	10.8	20d

Table 2. Data highlighting several high-performing perovskite solar cells that use planar perovskite layers

Cell Layout	V _{oc} (V)	I _{sc} (mA/cm ²)	FF	PCE (%)	Ref.
Cell Type: Planar-R					
ITO-PEIE/Y-TiO ₂ -MAPICl/spiroOMeTAD/Au	1.13	22.75	0.75	19.3	21a
FTO/c-SnO ₂ /MAPBr-FAPI/spiroOMeTAD/au	1.14	21.30	0.74	18.4	21b
FTO/cTiO ₂ /MAPI/spiroOMeTAD/Au	1.05	22.2	0.75	17.5	21c
ITO/TiO ₂ -PC60BM/MAPI/spiroOMeTAD/Au	1.11	21.0	0.77	17.6	21d
FTO/cTiO ₂ /MAPI/spiroOMeTAD/Ag	1.04	21.9	0.735	16.8	21e
ITO/TiO ₂ -PCBB-2CN-2C8/MAPI/spiroOMeTAD/Au	1.06	19.85	0.78	16.45	21f
FTO/cTiO ₂ /MAPICl/DERDTS-TBDT/MoO ₃ /Ag	1.05	21.2	0.73	16.2	21p
FTO/cSnO ₂ /MAPI/spiroOMeTAD/Au	1.11	22.83	0.64	16.02	21g
FTO/cZnO/MAPI/spiroOMeTAD/Ag	1.03	20.4	0.75	15.7	21h
FTO/cTiO ₂ /MAPI/spiroOMeTAD/Ag	1.07	21.5	0.67	15.4	21i
FTO/PEI/PCBM/MAPI/PTAA (polytriethylamine)/Au	0.98	21.8	0.72	15.3	21o
FTO/cTiO ₂ /MAPI/spiroOMeTAD/MoO ₃ /Ag	1.00	22.7	0.67	15.2	21j
FTO/ZnO/MAPI/spiroOMeTAD/Ag	1.08	20.04	0.70	14.99	21k
FTO/TiO ₂ -C60SAM/MAPI/spiroOMeTAD/Ag	1.01	20.00	0.73	14.8	21l
FTO/ZnO/MAPI/spiroOMeTAD/Ag	1.06	19.44	0.79	14.35	21m
FTO/ZnO-C3SAM/MAPI/spiroOMeTAD/MoO ₃ /Ag	1.07	22.51	0.65	14.25	21n
Cell Type: Planar-I					
ITO/PEDOT:PSS/Perov1/PC71BM/Ca-Al	1.03	20.6	0.85	18.0	22a
ITO/PEDOT:PSS/MAPI/PC61BM/PFN/al	1.05	20.3	0.80	17.1	22b
ITO/PEDOT:PSS/MAPI-D/PC61BM/MUTAB/Ag	1.03	20.06	0.80	16.50	22c
ITO/PEDOT:PSS/MAPI/ZnO ALD/Ag	1.02	20.73	0.76	16.15	22d
ITO/PEDOT:PSS/MAPI/PC61BM/Al	0.87	22.31	0.80	15.58	22e
ITO/Cu:NiOx/Perov/PC61BM/C60surf/Ag	1.11	19.01	0.73	15.40	22f
ITO/polyTPD/MAPI/PCBM/C60/BCP/Ag	1.10	22.0	0.70	15.3	22g
ITO/VB-DAAF/MAPI/C ₆₀ /BCP/Al	1.02	18.92	0.78	15.17	22h
ITO/PEDOT:PSS-GeO ₂ /MAPI/PCBM/Ag	0.96	20.57	0.74	15.15	22i
ITO/PEDOT:PSS/MAPI/PCBC fullerene/Al	0.98	22.08	0.70	15.08	22j
ITO/PEDOT:PSS/MAPI/PCBM/BCP/Ag	0.99	20.8	0.73	15.00	22k

Mechanistic Studies

In addition to extensive performance evaluations, the optical, electronic, and photoluminescence properties of perovskite sensitizers have been extensively studied and revealed several attractive features of this family of light absorbers. The excitons produced by light absorption have a weak binding energy of about 30 mV, indicating that most of them dissociate very rapidly as free carriers at room temperature. Solar cells based on such sensitizers have the potential to deliver photovoltage close to the bandgap energy. The resulting electrons and holes exhibit a small effective mass, yielding high carrier mobilities ranging from 7.5 cm²V⁻¹s⁻¹ for electrons to 12.5 cm²V⁻¹s⁻¹ for the holes. Snaith et al.^{17d} measured effective mobilities of 11.6 cm²V⁻¹s⁻¹ for MAPI_{3-x}Cl_x and ~8 cm²V⁻¹s⁻¹ for MAPI, exceptionally high for solution-processed materials. This surpasses charge mobilities reported for the mesoporous TiO₂ used in DSSC by at least a factor of 20, and those of typical π-conjugated molecular semiconductors by several orders of magnitude. The recombination of the charge carriers occurs relatively slowly at hundreds of nanoseconds and results in long carrier diffusion lengths (100 nm to 1,000 nm).¹⁷ The long diffusion length implies that charges can be transported over much longer distances than the absorption length of light in the material, rendering highly efficient collection.

Conceptually, the operational principle of PSCs is similar to that of both dye-sensitized and inorganic solar cells. Optical excitation within the perovskite film is followed by electron transfer to the TiO₂ scaffold and/or hole transfer to the HTM. These processes must be kinetically fast in comparison to the recombination rates of the photogenerated species and also compared to the rate of back electron transfer at the interfaces between the TiO₂/HTM/perovskite materials. For mesoscopic systems, interfacial properties largely determine the device performance. Halide perovskites have small exciton binding energy (≤ 50 mV) and in planar devices photogenerated bound excitons readily dissociate (in few ps) to free charge carriers. The free electrons and holes both have high mobilities ($\approx 10\text{--}30$ cm²V⁻¹s⁻¹) to diffuse apart. Optimal separation and collection of electrons and holes at the collector electrode requires their diffusion lengths to be several times longer than the film thickness required for quantitative light absorption. The high efficiency observed in several planar devices indicates that for these processes a typical absorber layer thickness of 400 nm is required.

Charge Carrier Dynamics

A comparative study of charge transport processes in the three different device architectures (mesoporous TiO₂ scaffold, mesoporous Al₂O₃, and planar) was made using visible pump, visible-NIR probe transient absorption spectroscopy.²³ In PSCs composed of mesoporous Al₂O₃, electron injection from the excited perovskite to the oxide is blocked by virtue of the high-energy conduction band level. In this case, the interfacial charge separation is effected by hole transfer to the HTM; injected electrons are transported through the perovskite absorber. In the planar layer case, no electron injection takes place because the photogenerated charge carriers migrate through the perovskite layer to reach the electron and hole-selective interfaces and get separated across these heterojunctions. In all three cases, hole transfer to the HTM takes place. When exposed to ambient conditions, coated mesoporous-Al₂O₃ and planar systems show a rapid and significant degradation in the yield of long-lived charge separation. This process occurs when both light and oxygen are present but does not affect the mesoporous TiO₂ scaffold case.

Hysteresis in the I-V Curves

A lingering issue with PSCs is the observation of a scan-rate dependent hysteresis phenomenon in the current-voltage curves.²⁴ Specifically, photocurrent variation with voltage in the forward and reverse sweep directions is not the same. The magnitude of hysteresis depends on the sweep onset voltage and the direction (from positive to negative values during backward scan or in the opposite forward scan). The hysteresis is observed to varying degrees in all three device architectures and regardless of the morphology of the perovskite layer. It is not caused by the presence of a compact TiO₂ layer or due to the hole transport material used and appears to be inherent to the perovskites and associated interfaces. This hysteresis renders standard PCE measurements ambiguous (overall PCE is higher with faster scan rates). Several explanations have been proposed for this phenomenon: very slow trapping and de-trapping of charges, ferroelectric behavior of the perovskites on nanosecond timescale, slow ion migration or displacement, and chemical structural changes. Accurate measurements of PCE must, therefore, be made using extremely slow scan rates or by measuring the stabilized power output at maximum power-point and by tracking the power output until it reaches a constant value. Additionally, few hysteresis-free PSC devices with inverted structure (FTO/PEDOT:PSS/MAPI/PCBM/BAP/Ag) having a PCE of 18.1% have been reported.^{24f}

Optimization of Individual Components of PSC

Here we will review some of the optimization studies where alternatives have been tested by replacing one or more of the key components of the perovskite. These include the oxide layer, the metal ion, the halide and organic cation of the perovskite, the electron-transport and hole transport layers, and the counter electrode.

Alkyl Ammonium Halides

A majority of perovskite solar cell studies utilize the hybrid perovskite MAPI. Several studies have also used the mixed halide (labeled as CH₃NH₃I_{3-x}Cl_x) that forms when PbCl₂ is used as a reactant for the methylammonium halide. This mixed halide has a bandgap comparable to the MAPI, but it exhibits an order of magnitude longer carrier diffusion length and performs equally well.

The tribromide analog CH₃NH₃PbBr₃ (MAPBr) has a higher bandgap (2.3 eV) compared to MAPI. Hence, any device based on MAPBr is expected to deliver a lower PCE. This expectation has, indeed, been confirmed in a passive PSC with mesoporous alumina Al₂O₃ scaffold. A graded series of mixed halide perovskites were prepared by mixing different ratios of MAI and MABr to yield perovskites with bandgaps between 1.55 and 2.3 eV. The mixed perovskite MAPI₂Br yields a 200 mV higher bandgap than MAPI (1.78 eV). Ultraviolet photoelectron spectroscopy studies indicate that the valence band edge of MAPI₃ and MAPI₂Br are similar (-5.40 eV) but their conduction band edges are different (-3.86 eV for MAPI₃ vs. -3.62 eV for MAPI₂Br). As expected for a solar cell device based on TiO₂ nanorods, the PCE for the devices increases from 4.29% for MAPI₃ to 4.89% for the MAPI₂Br.²⁵

Similarly, the mixed-organic-cation perovskite MA_{0.6}FA_{0.4}PbI₃ performed better (14.9% PCE) than both unmixed PSCs.^{19m} The methylammonium cation can be replaced by the larger formamidinium cation, [NH₂CH=NH₂]⁺ (FA), and the resulting formamidinium triiodide (FAPI) shows a smaller bandgap (1.48 eV FAPI vs. 1.55 eV for MAPI).²⁶ Solar cell devices prepared using FAPI exhibit strong photoluminescence, long lifetimes, higher PCE, and minimal hysteresis. In a recent study, a mixed halide perovskite film was prepared in a one-step procedure from a mixture of FAI, MABr, Pbl₂, and PbBr₂.^{19a} A solar cell device with mesoporous TiO₂ and spiro-OMeTAD as the hole transport layer showed a record high PCE of 20.8% for a Pbl₂/FAI molar ratio of 1.05 in the precursor solution. The photovoltage obtained (1.18 V) was also the highest value reported for any PSC to date.

Other Metal Ion Halide Perovskites

To avoid the use of toxic lead salts, researchers focused on replacing lead with two members of the same group, Sn and Ge. One problem in the preparation of Sn(II) derivatives is the instability of the resulting devices in the presence of oxygen and moisture. Using encapsulation under inert atmosphere, stable Sn(II) halide perovskite CH₃NH₃SnI₃ has been prepared and tested.²⁷ This Sn(II) perovskite has a bandgap of 1.3 eV, with charge carrier mobility of ≈ 1.6 cm²V⁻¹s⁻¹. It exhibits diffusion length of ca. 30 nm, shorter than the more than 1 μ m observed in the corresponding Pb(II) perovskite. The best performing Sn-based device (FTO/c-TiO₂/meso-TiO₂/MASnI₃/spiro-OMeTAD/Ag) reaches a power efficiency of 6.4% under 1-sun illumination. Quite remarkably for an absorber with a bandgap of 1.23 eV, the open circuit voltage is as high as 0.88 V in the most efficient device.

Kanatidis et al.²⁷ explored bandgap engineering of Sn(II) perovskites using chemical substitution in the form of CH₃NH₃SnI_{3-x}Br_x solid solutions. Among MASnI₃, MASnI₂Br, MASnIBr₂, and MASnBr₃ salts, solar cells with the dibromide derivate MASnIBr₂ (with a bandgap of 1.75 eV) show the highest PCE of 5.73%.

Optimization of the Oxide Anode/ETL

Similar to conventional DSSCs, there have been many optimization studies where different morphological forms—one-dimensional (1D), and three-dimensional (3D) and hierarchical structures—and doping of the semiconducting oxide layer(s) were used in PSCs. The compact layer of TiO_2 serves as an ETL and as a block for the perovskite absorber and the hole transporter that comes into direct contact with the transparent conducting oxide anode. Presence of the c-TiO_2 layer is, thus, essential in all three (passive, active, and planar) PSC devices.

Because the 3D nature of the mesoporous titania layer is widely believed to reduce electron mobility, a number of different forms of TiO_2 have been examined, including 1D nanostructures such as nanosheets, nanowires/fibers, nanorods, and nanotubes.²⁸ One such study reports a PCE of 14.8% for a PSC made of highly transparent TiO_2 anatase nanotube arrays. PSCs made of rutile nanorods show a PCE of 9.4%. One-dimensional nanostructures present a fairly low surface area compared to their mesoporous counterparts. Hierarchical structures grown on 1D nanostructures provide higher surface area and have seen a 25% increase in the photocurrents with constant photovoltages. Mg or Y-doping of TiO_2 gives rise to an increased PCE, presumably due to the widening of the TiO_2 bandgap by 100 mV and related better light harvesting by the perovskite.

SnO_2 has several attractive properties relative to TiO_2 . It exhibits a higher bandgap (3.8 eV), reducing any photocatalytic activity caused by near UV component of solar radiation and rendering higher device stability. It also exhibits charge carrier mobility up to $240 \text{ cm}^2\text{V}^{-1}\text{s}^{-1}$ (two orders of magnitude higher) with low density of trap states, and it possesses a deeper conduction band that facilitates a more efficient transfer of photogenerated electrons. There have been few studies of PSC using SnO_2 anodes.²⁹ A record solar conversion efficiency of 18.4% was obtained^{22b} for a PSC based on SnO_2 as ETL and a mixed halide perovskite MAPBr_3 (15%)- FAPbI_3 (85%).

ZnO has a bandgap similar to that of TiO_2 (3.3 eV) with comparable electron affinity. However the conductivity of ZnO is several orders of magnitude higher than that of TiO_2 , making it an attractive ETL. As in the case of nanorods of TiO_2 , PSCs based on ZnO nanorods achieve comparatively inferior performance (PCE 11%). Liu and Kelly^{21h} obtained a PCE of 15.7% on a PSC based on a compact ZnO as ETL over which a planar layer of $\text{MAPI}_{3-x}\text{Cl}_x$ was used as the light absorber. A PSC based on sputtered compact films of ZnO and MAPI ³⁰ (ITO/ ZnO / MAPI /spiro-OMeTAD/Ag) shows similar PCE values (15.9%). For passive forms of mesoscopic oxides, ZrO_2 was found³¹ to be equally effective as alumina, and PSCs made using this configuration exhibit comparable PCE (10.8% with ZrO_2 vs. 10.9% with mesoporous Al_2O_3).

Back Contact

Generally, a thin film of noble metal (Au or Ag) is deposited on top of the hole transport layer to serve as the back contact in solar cells. In a cost-saving approach, attempts have been made to use various allotropes of carbon as a counter electrode. Mhaisalkar et al.³² managed to successfully transfer carbon nanotubes onto the HTM in order to construct a PSC with mesoporous TiO_2 as an "active" scaffold and spiro-OMeTAD as the HTM. The MAPI /CNTs solar cell showed an efficiency of up to 6.87%, demonstrating the potential of applying carbon nanotubes as a charge collector, eliminating both the metal electrode and hole transporter in perovskite solar cells. The addition of the hole transporter spiro-OMeTAD over the perovskite improved the efficiency to 9.90%.

Graphite-carbon black paste has also been used to prepare a mesoporous carbon counter electrode and use it to construct an HTM-free PSC device.³³ A PSC based on mesoporous layers of ZrO_2 and Carbon (FTO/ c-TiO_2 /meso- TiO_2 /MAPI/ ZrO_2 /C) displays a remarkable PCE of 11.63%. Compared with Au or Pt CE, printable carbon counter electrodes are much cheaper and easier to process, especially for large-scale production.

Hole Transport Materials

Prompt and quantitative capture of photogenerated charge carriers is essential to deliver maximum PCE. Hence, there has been a great effort to identify newer, more efficient electron transport materials (ETM) and HTM. For the best performance, hole transport mediators must meet several requirements. Along with the high hole mobility and good solubility in organic solvents, it must have good compatibility between its HOMO energy levels and the valence band level of the perovskite. High hole mobility permits fast extraction of charges and a higher photocurrent. Sluggish movement of holes leads to higher internal resistance and this in turn reduces the fill factor of devices. Based on the chemical composition, HTM can be grouped into three categories: inorganic, small molecule (organic), and polymeric.

The best HTM used in PSCs has been spiro-OMeTAD (Figure 3), which belongs to the small molecule HTM group. A PCE of >18% has been obtained by applying this material. In spite of its excellent performance, this compound has some limitations. The oxidized form of the spiro-OMeTAD exhibits absorption in the visible light region with a maximum at 520 nm, essentially acting as a filter. The conductivity and hole mobility of pristine spiro-OMeTAD are quite low ($8.7 \times 10^{-5} \text{ Scm}^{-1}$ and $4 \times 10^{-5} \text{ cm}^2\text{V}^{-1}\text{s}^{-1}$). These values increase by an order of magnitude upon addition of select p-dopants, although it would be ideal to have a HTM that functions well without any further dopants.

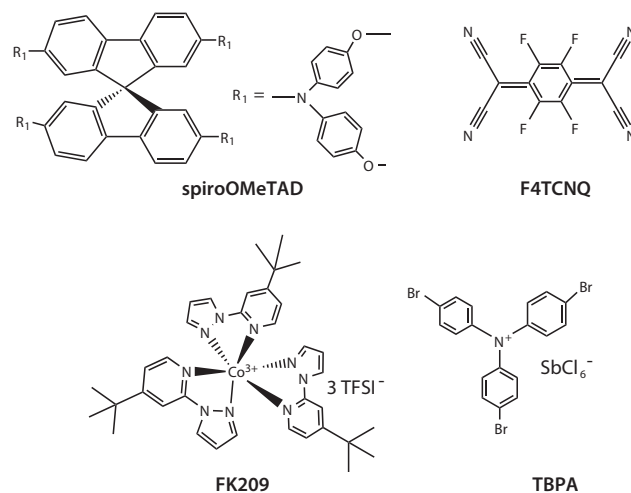


Figure 3. Chemical structure spiro-OMeTAD and some of its p-dopants.

Several additives, mostly metal complexes or salts have been tested as dopants: (p- BrC_6H_4)₃ NSbCl_6 , Co(III) complexes such as tris(2-(1H-pyrazol-1-yl)pyridine)cobalt(III) (FK102), lithium bis(trifluoromethanesulfonyl)imide (LiTFSI), SnCl_4 , SbCl_5 and FeCl_3 , WO_3 , molybdenum tris[1,2-bis(trifluoromethyl)ethane-1, 2-dithiolen], and F4-TCNQ. Most of them are usually applied by vacuum deposition in order to improve electrical conductivity, electron injection, and to reduce recombination. Li ions tend to insert onto the TiO_2 film, altering its electronic properties. The cobalt(III) complex FK209 shows much better solubility in the spiro-OMeTAD-based precursor solution.

Specific examples of HTM that have been found effective with PCE $\geq 7\%$ include CuSCN , CuI , NiO , V_2O_5 , and graphene oxide (GO)—typical inorganic HTMs. Typical examples of small molecule HTMs are spiro-OMeTAD and its extended derivatives; carbazole-based V886, X19, X51, and SGT 405; spiro-acridine-fluorene based CW4; silolothiophene-based triphenylamines; quinolizino acridines; tetra-azulene derivatives, thiophene-based H101 and H111; tetraphenylbenzidine-TPB-based TPBC; and triptycene derivative T103. The donor-acceptor properties of several organic aromatic molecules with a delocalized π -system have been adjusted by the introduction of various functional units to form the

second category of small-molecule HTMs. Examples of this type of HTM include functionalized derivatives of pyrene, thiophene and bithiophenes, perylene, carbazoles, triarylaminines, tetrathiafulvalene, spirofluorene-linked triphenylamines such as spiro-OMeTAD, and TPB. The third group, polymeric HTMs, are efficient in bulk heterojunction polymer organic solar cells. Typical examples of polymeric HTMs are thiophene-based P3HT, triarylamine-based PTAA, phenyl benzidine-based polyTPD, thiophene-based PCPDTBT, PCDTBT, and PCBDTPP and polyfluorenes such as TFO, PFB, and TEB (Figure 4).

Table 3 presents data on some of the best-performing HTMs examined in PSCs having the mesoscopic active scaffold of TiO_2 .³⁴ All of these studies employ either MAPI or its chloride analog $\text{MAPI}_{3-x}\text{Cl}_x$. The bandgap energy of these two materials is very similar (1.55–1.58 eV). With the same choice of electron transport layer (TiO_2), it is meaningful to compare the PCE obtained with different HTMs. With a judiciously tailored design of an HTM, researchers have attained PCE values greater than 18%. A unique, distinguishing feature of PSCs is high photovoltage (≥ 1 V) obtainable with light absorbers of bandgap of 1.5–1.6 eV. Intrinsic losses attributable to the direct bandgap perovskite light absorber are low due to low exciton binding energy (≤ 50 meV), long electron/hole diffusion length (≥ 100 nm), and high mobility of holes and electrons (in the range $1\text{--}10\text{ cm}^2\text{V}^{-1}\text{s}^{-1}$). The ratio of V_{oc}/E_{bg} is ≈ 0.69 , which is higher than that of polymer organic solar cells (≈ 0.55). However, this value is still lower than the 0.80 obtained for thin film amorphous-Si and GaAs thin film solar cells. Proper alignment of the energy levels of the ETL and HTM with respect to the valence and conduction band energy levels of the perovskite is essential to improve the light harvesting efficiency. Examination of the data collected in **Table 3** shows a decreasing PCE value is accompanied by a systematic decrease in the V_{oc} and fill factor of the solar cell device. A higher fill factor is obtainable in devices with a sheet resistance and a high shunt resistance.

Table 3. Solar cell conversion efficiency of perovskite solar cells of mesoscopic TiO_2 active scaffolds with different hole transport materials (FTO/c- TiO_2 /meso- TiO_2 /MAPI/HTM/CE).

HTM	PCE (%)	V_{oc} (V)	Fill Factor	Ref.
spiro-OMeTAD	18.36	1.094	0.78	19d
Carbazole V886	16.91	1.08	0.73	19d
Spiro-acridine-fluorene	16.56	1.05	0.72	19o
Azulene triarylamine	16.5	1.08	0.71	21p
PTAA	16.2	1.04	0.73	34a
PTAA	16.2	1.09	0.76	19i
Ethylendioxythiophene	15.4	1.07	0.72	34b
Carbazole SGT405	14.8	1.02	0.71	34c
Triphenylamine	13.63	0.97	0.67	34d
Spiro-CPDT	13.4	0.97	0.72	34e
Ethylendioxythiophene	13.2	1.05	0.65	34f
Tetraphenylbenzidine	13.10	0.94	0.72	34g
Phenoxazine M1	13.2	1.05	0.65	34h
Carbazole SGT411	13.0	1.00	0.67	34i
Tryptycene T103	12.87	0.985	0.62	34j
Quinolizino acridine	12.8	1.036	0.68	34k
Triazine-Ph-OMeTPA	12.51	0.92	0.66	34l
Pyrene arylamine Py-C	12.4	0.89	0.69	34m
CuSCN	12.4	1.016	0.62	34n
FA-MeoPh	11.86	0.92	0.70	34o
TIPS-pentacene	11.5	0.91	0.60	34p
NiO	11.4	0.89	0.71	34q
Tetrathiofulvene TTF-1	11.03	0.86	0.64	34r
Bithiophene KTM3	11.0	1.08	0.78	34s
Carbazole X51	9.8	0.88	0.66	34t
PDPPDBTE	9.2	0.85	0.75	34u
CuI	8.3	0.62	0.71	34v
Carbazole X19	7.6	0.76	—	34t
Polythiophene PCPDTBT	5.3	0.77	0.67	34w

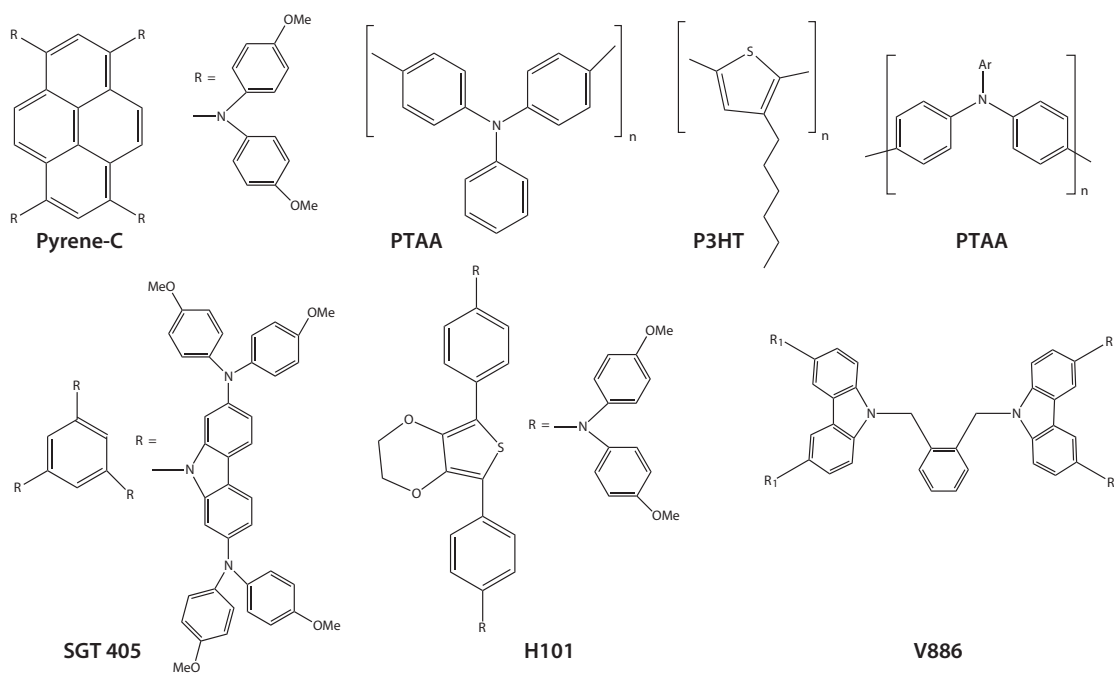


Figure 4. Some examples of polymeric hole transport materials.

Tandem Devices Based on Perovskite Solar Cells

Halide PSCs made with MAPI absorb light efficiently in the blue-green region of the solar spectrum. These PSCs show a clear transparent window at longer wavelengths (>800 nm), opening up the possible design of tandem solar cell packs. A low bandgap solar cell made of Si or CIGS placed as the bottom cell can collect all the light in the red and near-IR region. A tandem device made up of amorphous Si (Ag/AZO/a-Si:H/c-Si/a-Si:H(ITO)) has been successfully connected to a top PSC using a thin layer of transparent SnO₂ deposited on the top of the Si solar cell.^{35a} The tandem device of the (Ag/a-Si:H/c-Si/aSi:H(ITO)/SnO₂/perovskite/spiroOMeTAD/MoO₃/ITO) layout showed an efficiency of 18%, the highest value for this type of cell architecture. Thin MoO₃ serves as a protective layer between this hole conductor and the transparent top electrode of ITO. The back side of the Si cell is fully covered with aluminum-doped zinc oxide (AZO) and silver, both deposited by sputtering. Simulation studies^{35b} of a tandem device made up of MAPI PSC and Si solar cell indicate that with optimized layer thickness the tandem device can deliver efficiency of >30%. A study of a tandem device composed of CIGS as the bottom cell and a perovskite on the top has also been made.^{35c}

Large Area Modules of PSCs

During the past year there have been few successful reports on the fabrication of large area PSC modules. Razza et al.^{36a} optimized the sequential deposition method of halide perovskites to prepare 10 mm² solar cells that achieved a maximum efficiency of 13.3% and an average efficiency of 12.1%. To prove the scalability of the process, series-connected modules were fabricated containing blade-coated PbI₂ films. A module efficiency of 10.4% was then obtained for a 10.1 cm² active area, and an efficiency of 4.3% was measured for a module area of 100 cm².

In a related study, Yang et al.^{36b} used a large excess of organic halide anion during the two-step perovskite preparation and anti-solvent to grow large grain-sized crystals. This achieved a PCE of 16.3% for a planar PSC with 1.2 cm² active area (stabilized PCE output of ≈15.6%). When the device area was reduced to 0.12 cm², a maximum PCE of 18.3% was achieved (stabilized output of ≈17.5%). In 2015, researchers at IMEC, Belgium, reported successful preparation of a perovskite solar cell with 16 cm² active area and a PCE of 11.9%.

An important experimental strategy was recently developed^{36c} to prepare heavily doped inorganic charge extraction layers in planar PSCs to achieve very rapid carrier extraction, avoid pinholes, and eliminate local structural defects over large areas even with 10- to 20-nanometer-thick layers. The robust inorganic nature of the layers enabled fabrication of PSCs with an aperture area >1 cm² and a PCE >15%. Hysteresis in the current-voltage characteristics was eliminated, creating stable PSCs with >90% of the initial PCE remaining after 1,000 hours of light exposure.

Concluding Remarks

Progress in the development of high efficiency solar cells has been so remarkable that within the last three years the solar conversion efficiency has rapidly soared to 21%. However, a number of important conditions must be achieved for hybrid halide perovskite-based solar cells to reach their commercial potential.

- First, improved understanding and control of experimental conditions is required in order to enable easy replication of results across different laboratories. For example, preparative conditions vary significantly, and these conditions strongly influence the crystalline (electronic) and morphological properties of the perovskite layer. This, in turn, drastically affects the overall PCE. Hysteresis observed in the I-V curves requires that photocurrent and voltage must be measured under very slow sweep rate conditions.
- Second, promising solar efficiencies must be replicated in large area modules and panels. Solar cells used in fundamental studies are typically small in size (≤1 cm²), and confidence in the reproducibility of a given method requires measurement in large area samples. Few encouraging reports have appeared recently on the preparation of such large area modules (≥10 cm²) with good efficiency (>10%).
- Third, long-term stability of these new solar devices must be demonstrated under realistic field operating conditions that include elevated temperatures, high moisture/humidity, and constant exposure to light. Few select design layout and material preparation methods have been identified in which the solar cell shows stable performance of at least 1,000 hours under conditions of full solar light exposure or heating to 85 °C. Extensive investigation and development will be required to fully address the moisture sensitivity of PSCs. Either a non-toxic replacement for lead-based perovskite materials and/or a highly robust encapsulation technique will be needed to prevent negative environmental impacts from this technology.
- Last, in order to unleash the enormous potential of PSCs, successful large-scale, low-cost manufacturing methods must be developed.

References

- (1) (a) Green, M. A. *Third Generation Photovoltaics: Advanced Solar Energy Conversion*, Springer Series in Photonics, vol. 12, Springer Verlag, Berlin, **2003**. (b) Conibeer, G. *Mater. Today* **2007**, *10*, 42.
- (2) (a) Kalyanasundaram, K., (ed.) *Dye Sensitized Solar Cells*, EPFL Press, Lausanne, **2010**. (b) Hagfeldt, A.; Boschloo, G.; Sun, L.; Kloo, L.; Pettersson, H. *Chem. Rev.* **2010**, *110*, 6595.
- (3) O'Regan, B.; Grätzel, M. *Nature* **1991**, *353*, 737.
- (4) Kakiage, K.; Aoyama, Y.; Yano, T.; Oya, K.; Fujisawa, J.-I.; Hanaya, M. *Chem. Commun.* **2015**, *51*, 15894-15897.
- (5) (a) Wells, H. L. Z. *Anorg. Chem.* **1893**, *3*, 195. (b) Møller, C. K. *Nature* **1958**, *182*, 1436. (c) Weber, D. Z. *Naturforsch.* **1978**, *33B*, 1443. (d) Mitzi, D.B. *Prog. Inorg. Chem.* **2007**, *48*, 1.
- (6) Kojima, A.; Teshima, K.; Shirai, Y.; Miyasaka, T. *J. Amer. Chem. Soc.* **2009**, *131*, 6050.
- (7) (a) Im, J.-H.; Lee, C.-R.; Lee, J.-W.; Park, S.-W.; Park, N.-G. *Nanoscale* **2011**, *3*, 4088. (b) Park, N.-G. *Material Matters* **2013**, *8*, 126.
- (8) Chang, I.; Lee, B.; Ho, J.; Chang, R. P. H.; Kanatzidis, M. G. *Nature* **2012**, *485*, 486.
- (9) (a) Lee, M. M.; Teuscher, J.; Miyasaka, T.; Murakami, T. N.; Snaith, H. J. *Science* **2012**, *338*, 643. (b) Kim, H.-S.; Lee, C. R.; Im, J.-H.; Lee, K.-B.; et al. *Sci. Rep.* **2012**, *2*, 591.
- (10) Unpublished results (2016), cf. National Renewable Energy Laboratory Best Research-Cell Efficiencies chart: www.nrel.gov/ncpv/images/efficiency_chart.jpg
- (11) (a) Lee, M. M.; Teuscher, J.; Miyasaka, T.; Murakami, T. N.; Snaith, H. J. *Science* **2012**, *338*, 643. (b) Kim, H.-S.; Lee, C. R.; Im, J.-H.; Lee, K.-B.; et al. *Sci. Rep.* **2012**, *2*, 591.
- (12) (a) Burschka, J.; Pellet, N.; Moon, S.-J.; Humphry-Baker, R.; Gao, P.; Nazeeruddin, Md. K.; Grätzel, M. *Nature* **2013**, *499*, 316. (b) Im, J.-H.; Jang, I.-H.; Pellet, N.; Grätzel, M.; Park, N.-G. *Nat. Nanotechnol.* **2014**, *9*, 927.
- (13) Liu, M.; Johnston, M. B.; Snaith, H. J. *Nature* **2013**, *501*, 395.
- (14) Etgar, L.; Gao, P.; Xue, Z.; Peng, Q.; Chandiran, A. K.; Liu, B.; Nazeeruddin, M. K.; Grätzel, M. J. *Amer. Chem. Soc.* **2012**, *134*, 17396.
- (15) (a) Ball, J. M.; Lee, M. M.; Hey, A.; Snaith, H. J. *Energy Environ. Sci.* **2013**, *6*, 1739; (b) Guarnera, S.; Abate, A.; Zhang, W.; Foster, J. M.; Richardson, G.; Petrozza, A.; Snaith, H. J. *J. Phys. Chem. Lett.* **2015**, *6*, 432.
- (16) (a) Liu, D.; Kelly, T. L. *Nature Photon.* **2014**, *8*, 133. (b) Liu, D.; Kelly, T. L.; J. *Amer. Chem. Soc.* **2014**, *136*, 17116. (c) Yang, J.; Siempelkamp, B. D.; Masconi, E.; De Angelis, F.; Kelly, T. *Chem. Mater.* **2015**, *27*, 4229.

- (17) (a) Xing, G. C.; Mathews, N.; Sun, S. Y.; Lim, S. S.; Lam, Y. M.; Grätzel, M.; Mhaisalkar, S.; Sum, T. C. *Science* **2013**, *342*, 344. (b) Stranks, S. D.; Eperon, G. E.; Grancini, G.; Melnlou, C.; et al. *Science* **2013**, *342*, 341. (c) Dong, Q.; Fang, Y.; Shao, Y.; Mulligan, P.; Qiu, J.; Cao, L.; Huang, J. *Science* **2015**, *347*, 967. (d) Wehrenfenning, C.; Eperon, G. E.; Johnston, M. B.; Snaith, H. J.; Herz, L. M. *Adv. Mater.* **2014**, *26*, 1584.
- (18) Docampo, P.; Ball, J. M.; Darwich, M.; Eperon, G. E.; Snaith, H. J. *Nat. Commun.* **2013**, *4*, 1.
- (19) (a) Bi, D.; Tress, W.; Dar, I.; Gao, P.; et al. *Sci. Adv.* **2016**, *2*, e150110. (b) Yang, W. S.; Noh, J. H.; Jeon, N. J.; Kim, Y. C.; Ryu, S.; Seo, J.; Seok, S. I. *Science* **2015**, *348*, 1234. (c) Ahn, N.; Son, D.-Y.; Jan, J.-H.; Kang, S. M.; Choi, M.; Park, N.-G. *J. Am. Chem. Soc.* **2015**, *137*, 8696. (d) Gratia, P.; Magomedo, A.; Malinauskas, T.; Daskeviciene, M.; et al. *Angew. Chem., Int. Ed.* **2015**, *54*, 11409. (e) Li, W.; Fan, J.; Mai, Y.; Wang, L. *J. Am. Chem. Soc.* **2015**, *137*, 10399. (f) Im, J.-H.; Jan, I.-H.; Pellet, N.; Grätzel, M.; Park, N.-G. *Nat. Nanotechnol.* **2014**, *9*, 927. (g) Jeon, N. J.; Lee, H. G.; Kim, Y. C.; Seo, J.; Noh, J. H.; Lee, J.; Seok, S. I. *J. Am. Chem. Soc.* **2014**, *136*, 7837. (h) Yang, D.; Yang, R.; Zhang, J.; Yang, Z.; Liu, S.; Li, C. *Energy Environ. Sci.* **2015**, *8*, 3208. (i) Jeon, N. J.; Noh, J. H.; Kim, Y.-C.; Yang, W. S.; Ryu, S.; Seok, S. I. *Nat. Mater.* **2014**, *13*, 897. (j) Shen, Q.; Ogomi, Y.; Chang, J.; Toyoda, T.; et al. *J. Mater. Chem. A* **2015**, *3*, 9308. (k) Jeon, N. J.; Lee, H. G.; Kim, Y. C.; Seo, J.; Noh, J. H.; Lee, J.; Seok, S. I. *J. Am. Chem. Soc.* **2014**, *136*, 7837. (l) Burschka, J.; Pellet, N.; Moon, S.-J.; Humphry-Baker, R.; Gao, P.; Nazeeruddin, M. K.; Grätzel, M. *Nature* **2013**, *499*, 316. (m) Pellet, N.; Gao, P.; Gregori, G.; Yang, T.-Y.; Nazeeruddin, M. K.; Maier, J.; Grätzel, M. *Angew. Chem., Int. Ed.* **2014**, *53*, 3151. (n) Qin, P.; Tanaka, S.; Ito, S.; Tetreault, N.; Manabe, K.; Nishino, H.; Nazeeruddin, M. D.; Grätzel, M. *Nat. Commun.* **2014**, *5*, 3834. (o) Nishimura, H.; Ishida, N.; Shimazaki, A.; Wakamiya, A.; Saeki, A.; Scott, L. T.; Murata, Y. *J. Am. Chem. Soc.* **2015**, *137*, 15656. (q) Lee, J.-W.; Seol, D.-J.; Cho, A.-N.; Park, N.-G. *Adv. Mater.* **2014**, *26*, 4991. (r) Li, M.-H.; Hsu, C.-W.; Shen, P.-S.; Cheng, H.-M.; Chi, Y.; Chen, P.; Guo T.-F. *Chem. Commun.* **2015**, *51*, 15518.
- (20) (a) Wojciechowski, K.; Saliba, M.; Leijtens, T.; Abate, A.; Snaith, H. J. *Energy Environ. Sci.* **2014**, *7*, 1142. (b) Guarnera, S.; Abate, A.; Zhang, W.; Foster, J. M.; Richardson, G.; Petrozza, A.; Snaith, H. J. *J. Phys. Chem. Lett.* **2015**, *6*, 432. (c) Ball, J. M.; Lee, M. M.; Hey, A.; Snaith, H. J. *Energy Environ. Sci.* **2013**, *6*, 1739. (d) Bi, D.; Moon, S. J.; Häggman, L.; Boschloo, G.; et al. *RSC Adv.* **2013**, *3*, 18762.
- (21) (a) Zhou, H.; Chen, Q.; Li, G.; Luo, S.; et al. *Science* **2014**, *345*, 542. (b) Correa Baena, J. P.; Steier, L.; Tress, W.; Saliba, M.; et al. *Energy Environ. Sci.* **2015**, *8*, 2928. (c) Song, D.; Cui, P.; Wang, T.; Wei, D.; et al. *J. Phys. Chem. C* **2015**, *119*, 2281. (d) Tao, C.; Neutzner, S.; Colella, J.; Marras, S.; et al. *Energy Environ. Sci.* **2015**, *8*, 2365. (e) Yang, B.; Dyck, O.; Poplawsky, J.; Keum, J.; et al. *J. Am. Chem. Soc.* **2015**, *137*, 9210. (f) Li, Y.; Zhao, Y.; Chen, Q.; Yang, Y.; Liu, Y.; Hong, Z.; Liu, Z.; Hsieh, Y.-T.; Meng, L.; Li, Y.; Yang, Y. *J. Am. Chem. Soc.* **2015**, *137*, 15540. (g) Li, Y.; Zhao, Y.; Chen, Q.; Yang, Y.; et al. *J. Am. Chem. Soc.* **2015**, *137*, 1554. (h) Ke, W.; Fang, G.; Liu, Q.; Xiong, L.; et al. *J. Am. Chem. Soc.* **2015**, *137*, 6730. (i) Liu, D.; Kelly, T. L. *Nature Photon.* **2014**, *8*, 133. (j) Liu, M.; Johnston, M. B.; Snaith, H. J. *Nature* **2013**, *501*, 395. (k) Yang, L.; Wang, J.; Leung, W. W. *ACS Appl. Mater. Interfaces* **2015**, *7* (27), 14614–14619. (l) Zhang, J.; Pauporté, J. *Phys. Chem. C* **2015**, *119*, 14919. (m) Wojciechowski, K.; Stranks, S. D.; Abate, A.; Sadoughi, G.; et al. *ACS Nano* **2014**, *8*, 12701. (n) Son, D.-Y.; Bae, K.-H.; Kim, H.-S.; Park, N.-G. *J. Phys. Chem. C* **2015**, *119*, 10321. (o) Zuo, L.; Gu, Z.; Ye, T.; Fu, W.; Wu, G.; Li, H.; Chen, H. *J. Am. Chem. Soc.* **2015**, *137*, 2674. (p) Ryu, S.; Seo, J.; Shin, S. S.; Kim, Y. C.; Jeon, N. J.; Seok, S. I. *J. Mater. Chem. A* **2015**, *3*, 3271. (q) Liu, Y.; Hong, Z.; Chen, Q.; Chen, H.; Chang, W.-H.; Yang, Y.; Song, T.-B.; Yang, Y. *Adv. Mater.* **2016**, *28*(3), 440.
- (22) (a) Wu, C.-G.; Chiang, C.-H.; Tseng, Z.-L.; Nazeeruddin, M. K.; Hagfeldt, A.; Grätzel, M. *Energy Environ. Sci.* **2015**, *8*, 2725. (b) You, J.; Yang, Y.; Hong, Z.; Song, T.-B.; et al. *Appl. Phys. Lett.* **2014**, *105*, 183902. (c) Chang, C.-Y.; Chang, Y.-C.; Huang, W.-K.; Lee, K.-T.; Cho, A.-C.; Hsu, C.-C. *Chem. Mater.* **2015**, *27*, 7119. (d) Chang, C.-Y.; Lee, K.-T.; Huang, W.-K.; Siao, H.-Y.; Chang, Y.-C. *Chem. Mater.* **2015**, *27*, 5122. (e) Tsai, H.; Nie, W.; Cheruku, P.; Mack, N. H.; Xu, P.; Gupta, G.; Mohite, A. D.; Wang, H.-L. *Chem. Mater.* **2015**, *27*, 2750. (f) Kim, J. H.; Liang, P.-W.; Williams, S. T.; Cho, N.; Chueh, C.-C.; Glaz, M. S.; Ginger, D. S.; Jen, A. K.-Y. *Adv. Mater.* **2015**, *27*, 695. (g) Zhao, D.; Sexton, M.; Park, H.-Y.; Baure, G.; Nino, J. C.; So, F. *Adv. Energy Mater.* **2015**, *5*, 1401855. (h) Chiang, T.-Y.; Fan, G.-L.; Jeng, J.-Y.; Chen, K. C.; Chen, P.; Wen, T.-C.; Guo, T.-F.; Wong, K.-T. *ACS Appl. Mater. Interfaces* **2015**, *7*, 24973. (i) Wang, Z.-K.; Li, M.; Yuan, D.-X.; Shi, X.-B.; Ma, H.; Liao, L.-S. *ACS Appl. Mater. Interfaces* **2015**, *7*, 9645. (j) Liu, X.; Jiao, W.; Lei, M.; Zhou, Y.; Song, B.; Li, Y. *J. Mater. Chem. A* **2015**, *3*, 9278. (k) Qing, J.; Chandran, H.-T.; Cheng, Y.-H.; Liu, X.-K.; Li, H.-W.; Tsang, S.-W.; Lo, M.-F.; Lee, C.-S. *ACS Appl. Mater. Interfaces* **2015**, *7*, 23110.
- (23) O'Mahony, F. T. F.; Lee, Y. H.; Jelllett, C.; Dmitrov, S.; et al. *J. Mater. Chem. A* **2015**, *3*, 7219.
- (24) (a) Tress, W.; Marinova, N.; Moehl, T.; Zakeeruddin, S. M.; Nazeeruddin, M. K.; Grätzel, M. *Energy Environ. Sci.* **2015**, *8*, 995. (b) Snaith, H. J.; Abate, A.; Ball, J. M.; Eperon, G. E.; et al. *J. Phys. Chem. Lett.* **2014**, *5*, 1511. (c) Unger, E. L.; Hoke, E. T.; Bailie, C. D.; Nguyen, W. H.; Bowring, A. B.; Heumüller, T.; Christoforo, M. G.; McGhee, M. D. *Energy Environ. Sci.* **2014**, *7*, 3690. (d) Van Reenan, S.; Kemerink, M.; Snaith, H. J. *J. Phys. Chem. Lett.* **2015**, *6*, 3808. (e) Kim, H.-S.; Jang, I.-H.; Ahn, N. M.; Choi, M.; Guerrero, A.; Bisquet, J.; Park, N.-G. *J. Phys. Chem. Lett.* **2015**, *6*, 4633. (f) Heo, J. H.; Han, H. J.; Kim, D.; Ahn, T. K.; Im, S.-H. *Energy Environ. Sci.* **2015**, *8*, 1602. (g) Forcacs, D.; Sessolo, M.; Bolink, J. J. *Mater. Chem.* **2015**, *3*, 14121.
- (25) Qiu, J.; Qiu, Y.; Zhong, M.; Mu, C.; Yang, S. *Nanoscale* **2013**, *5*, 3245.
- (26) Eperon, G. E.; Stranks, S. D.; Menelaou, C.; Johnston, M. B.; Herz, L. M.; Snaith, H. J. *Energy Environ. Sci.* **2014**, *7*, 982.
- (27) (a) Noel, N. K.; Stranks, S. D.; Abate, A.; Wehrenfenning, C.; et al. *Energy Environ. Sci.* **2014**, *7*, 3061. (b) Hao, F.; Stoumpos, C. C.; Chang, R. P. H.; Kanatzidis, M. G. *J. Am. Chem. Soc.* **2014**, *136*, 8093. (c) Hao, F.; Stoumpos, C. C.; Cao, D. H.; Chang, R. P. H.; Kanatzidis, M. G. *Nature Photon.* **2014**, *8*, 489.
- (28) (a) Kim, H.-S.; Lee, J.-W.; Yantara, N.; Boix, P. P.; Kulkarni, S. A.; Mhaisalkar, S.; Grätzel, M.; Park, N.-G. *Nano Lett.* **2013**, *13*, 2412. (b) Qin, P.; Paulose, M.; Dar, M. I.; Moehl, T.; Arora, N.; Gao, P.; Varghese, O. K.; Grätzel, M.; Nazeeruddin, M. K. *Small* **2015**, *11*, 5533. (c) Passoni, L.; Giordano, F.; Zakeeruddin, S. M.; Grätzel, M.; Di Fonzo, F. *RSC Adv.* **2015**, *5*, 93180.
- (29) (a) Zhu, Z.; Zheng, X.; Bai, Y.; Zhang, T.; Wang, Z.; Xiao, S.; Yang, S. *Phys. Chem. Chem. Phys.* **2015**, *17*, 18265–18268. (b) Li, Y.; Zhu, J.; Huang, Y.; Liu, F.; et al. *RSC Adv.* **2015**, *5*, 28424–28429.
- (30) Tseng, Z.-L.; Chiang, C.-H.; Wu, C.-G. *Sci. Rep.* **2015**, *5*, 13211.
- (31) Bi, D.; Moon, S.-J.; Häggman, L.; Boschloo, G.; Yang, L.; Johansson, E. M.; Nazeeruddin, M. K.; Grätzel, M.; Hagfeldt, A. *RSC Adv.* **2013**, *3*, 18762.
- (32) Li, Z.; Kulkarni, S. A.; Boix, P. P.; Shi, E.; et al. *ACS Nano* **2014**, *8*, 6797.
- (33) Zhang, L.; Liu, T.; Liu, L.; Hu, M.; Yang, Y.; Mei, A.; Han, H. *J. Mater. Chem. A* **2015**, *3*, 9165.
- (34) (a) Ryu, S.; Noh, J. H.; Jeon, N. J.; Kim, Y. C.; Yang, W. S.; Seo, J.; Seok, S. I. *Energy Environ. Sci.* **2014**, *7*, 2614. (b) Li, H.; Fu, K.; Boix, P. P.; Wong, L. H.; Hagfeldt, A.; Grätzel, M.; Mhaisalkar, S. G.; Grimsdale, A. C. *ChemSusChem* **2014**, *7*, 3420. (c) Sung, S. D.; Kang, M. S.; Choi, I. T.; Kim, H. M.; Hong, M.; Kim, H. K.; Lee, W. I. *Chem. Comm.* **2014**, *50*, 14161. (d) Choi, H.; Paek, S.; Lim, N.; Lee, Y.-H.; Nazeeruddin, M. K.; Ko, J. *Chem. Euro J.* **2014**, *20*, 10894. (e) Franckevicius, M.; Mishra, A.; Kreuzer, F.; Luo, J.; Zakeeruddin, S. M.; Grätzel, M. *Mater. Horiz.* **2015**, *2*, 613. (f) Li, H.; Fu, K.; Hagfeldt, A.; Grätzel, M.; Mhaisalkar, S. G.; Grimsdale, A. C. *Angew. Chem., Int. Ed.* **2014**, *53*, 4085. (g) Song, Y.; Lv, S.; Liu, X.; Li, X.; Wang, S.; Wei, H.; Li, D.; Xiao, Y.; Meng, Q. *Chem. Comm.* **2014**, *50*, 15329. (h) Cheng, M.; Xu, B.; Chen, C.; Yang, X.; Zhang, F.; Tan, Q.; Hua, Y.; Kloo, L.; Sun, L. *Adv. Energy Mater.* **2015**, *5*, 1401720. (i) Kang, M. S.; Sung, S. D.; Choi, I.-T.; Kim, H.; Hung, M.; Kim, J.; Lee, W. I.; Kim, H. K. *ACS Appl. Mater. Interfaces* **2015**, *7*, 22213. (j) Krishna, A.; Sabha, D.; Li, H.; Yin, J.; Boix, P. P.; Soci, C.; Mhaisalkar, S. G.; Grimsdale, A. C. *Chem. Sci.* **2014**, *5*, 2702. (k) Qin, P.; Paek, S.; Dar, M. I.; Pellet, N.; Ko, J.; Grätzel, M.; Nazeeruddin, M. K. *J. Am. Chem. Soc.* **2014**, *136*, 8516. (l) Do, K.; Choi, H.; Lim, K.; Jo, H.; Cho, J. W.; Nazeeruddin, M. K.; Ko, J.; *Chem. Commun.* **2014**, *53*, 10971. (m) Jeon, N. J.; Lee, J.; Noh, J.-H.; Nazeeruddin, M. K.; Grätzel, M.; Seok, S. I. *J. Am. Chem. Soc.* **2013**, *135*, 19087. (n) Qin, P.; Tanaka, S.; Ito, S.; Tetreault, N.; Manabe, K.; Nishino, H.; Nazeeruddin, M. K.; Grätzel, M. *Nat. Commun.* **2014**, *5*, 3834. (o) Choi, H.; Park, S.; Paek, S.; Ekanayake, P.; Nazeeruddin, M. K.; Ko, J. *J. Mater. Chem. A* **2014**, *2*, 19136. (p) Kazim, S.; Javier Ramos, F.; Gao, P.; Nazeeruddin, M. K.; Grätzel, M.; Ahmad, S. *Energy Environ. Sci.* **2015**, *8*, 1816. (q) Liu, Z.; Zhang, M.; Xu, X.; Bu, L. *Dalton Trans.* **2014**, *44*, 3967. (r) Liu, J.; Wu, Y.; Qin, C.; Yang, X.; et al. *Energy Environ. Sci.* **2014**, *7*, 2963. (s) Krishnamoorthy, T.; Kunwu, F.; Boix, P. P.; Li, H.; et al. *J. Mater. Chem. A* **2014**, *2*, 6305. (t) Xu, B.; Sheibanian, E.; Liu, P.; et al. *Adv. Mater.* **2014**, *26*, 6629. (u) Kwon, Y. S.; Lim, J.; Yun, H.-J.; Kim, Y.-K.; Park, T. *Energy Environ. Sci.* **2014**, *7*, 1454. (v) Christians, J. A.; Fung, R. C. M.; Kamat, P. V. *J. Am. Chem. Soc.* **2014**, *136*, 758. (w) Heo, J. H.; Im, S. H.; Noh, J. H.; Mandal, T. K.; et al. *Nature Photon.* **2013**, *7*, 486.
- (35) (a) Albrecht, S.; Saliba, M.; Correa Baena, J.-P.; Lang, F.; et al. *Energy Environ. Sci.* **2016**, *9*, 81. (b) Filipic, M.; Loper, P.; Niesen, B.; De Wolf, S.; Krc, J.; Ballif, C.; Topic, M. *Opt. Express* **2015**, *23*, A263. (c) Bailie, C. D.; Christoforo, G.; Mailo, J. P.; Bowring, A. R.; et al. *Energy Environ. Sci.* **2015**, *8*, 956.
- (36) (a) Razza, S.; Di Giacomo, F.; Matteocci, F.; Cina, L.; et al. *J. Power Sources* **2015**, *277*, 286. (b) Yang, M.; Zhou, Y.; Zang, Y.; Jian, C.-S.; Padture, N. P.; Zhu, K. *Adv. Mater.* **2015**, *27*, 6363. (c) Chen, W.; Wu, Y.; Yue, Y.; Liu, J.; et al. *Science* **2015**, *350*(6263), 944–948.

HAVE YOU MISSED OUR RECENT ISSUES?

- Vol. 10 No. 4: Biomaterials for Tissue Engineering (RVR)
- Vol. 10 No. 3: Alternative Energy Generation and Storage (RRB)
- Vol. 10 No. 2: Graphene and Carbon Materials (ROM)
- Vol. 10 No. 1: 10th Anniversary Issue—Materials that Matter (RJC)
- Vol. 9 No. 4: Materials for Energy Harvesting and Storage (REO)
- Vol. 9 No. 3: Polymers in Therapeutics and Nanomedicine (QZP)



To view a complete library of issues or to subscribe to our newsletter, visit

aldrich.com/materialmatters

Core-type Quantum Dots

For a complete list of available materials, visit aldrich.com/quantumdots.

PbS

Name	Description	Fluorescence Emission (λ_{em} in nm)	Prod. No.
PbS core-type quantum dots	10 mg/mL in toluene; oleic acid coated	1000	747017-10ML
	10 mg/mL in toluene; oleic acid coated	1200	747025-10ML
	10 mg/mL in toluene; oleic acid coated	1400	747076-10ML
	10 mg/mL in toluene; oleic acid coated	1600	747084-10ML

CdTe

Name	Description	Fluorescence Emission (λ_{em} in nm)	Prod. No.
CdTe core-type quantum dots	COOH functionalized	510	777986-10MG 777986-25MG
	COOH functionalized	520	777935-10MG 777935-25MG
	COOH functionalized	570	777943-10MG 777943-25MG
	COOH functionalized	610	777951-10MG 777951-25MG
	COOH functionalized	710	777978-10MG 777978-25MG
	COOH functionalized	770	777994-10MG 777994-25MG

Core-shell Type Quantum Dots

For a complete list of available materials, visit aldrich.com/quantumdots.

CdSe/ZnS

Name	Description	Fluorescence Emission (λ_{em} in nm)	Prod. No.
CdSe/ZnS core-shell type quantum dots	stabilized with octadecylamine ligands	520	748021-10MG 748021-25MG
	stabilized with octadecylamine ligands	540	748056-10MG 748056-25MG
	stabilized with octadecylamine ligands	560	748080-10MG 748080-25MG
	stabilized with octadecylamine ligands	580	748129-10MG 748129-25MG
	stabilized with octadecylamine ligands	600	748099-10MG 748099-25MG
	stabilized with octadecylamine ligands	620	790192-10MG 790192-25MG
	stabilized with octadecylamine ligands	630	790206-10MG 790206-25MG

InP/ZnS

Name	Description	Fluorescence Emission (λ_{em} in nm)	Prod. No.
InP/ZnS quantum dots	5 mg/mL in toluene stabilized with oleylamine ligands	530	776750-5ML
	5 mg/mL in toluene stabilized with oleylamine ligands	560	776793-5ML
	5 mg/mL in toluene stabilized with oleylamine ligands	590	776769-5ML
	5 mg/mL in toluene stabilized with oleylamine ligands	620	776777-5ML
	5 mg/mL in toluene stabilized with oleylamine ligands	650	776785-5ML

Alloyed Quantum Dots

For a complete list of available materials, visit aldrich.com/quantumdots.

Name	Description	Fluorescence Emission (λ_{em} in nm)	Prod. No.
CdSeS/ZnS alloyed quantum dots	1 mg/mL in toluene, diameter 6 nm	450	753742-5ML 753742-25ML
	1 mg/mL in toluene, diameter 6 nm	490	753750-5ML 753750-25ML
	1 mg/mL in toluene, diameter 6 nm	525	753769-5ML 753769-25ML
	1 mg/mL in toluene, diameter 6 nm	540	753777-5ML 753777-25ML
	1 mg/mL in toluene, diameter 6 nm	575	753785-5ML 753785-25ML
	1 mg/mL in toluene, diameter 6 nm	630	753793-5ML 753793-25ML
	1 mg/mL in toluene, diameter 6 nm	665	753807-5ML 753807-25ML
	1 mg/mL in H ₂ O, diameter 6 nm, COOH functionalized	490	754226-1ML 754226-5ML
	1 mg/mL in H ₂ O, diameter 6 nm, COOH functionalized	525	753831-1ML 753831-5ML
	1 mg/mL in H ₂ O, diameter 6 nm, COOH functionalized	540	753866-1ML 753866-5ML
	1 mg/mL in H ₂ O, diameter 6 nm, COOH functionalized	575	753874-1ML 753874-5ML
	1 mg/mL in H ₂ O, diameter 6 nm, COOH functionalized	630	753882-1ML 753882-5ML
	1 mg/mL in H ₂ O, diameter 6 nm, COOH functionalized	665	753890-1ML 753890-5ML
CdSeS/ZnS alloyed quantum dots kit	5 X 1 mg/mL in H ₂ O, diameter 6 nm, COOH functionalized	490-665	753904-1KT
	5 X 1 mg/mL in toluene, diameter 6 nm	490-665	753823-1KT

Precursors for Organometallic Perovskites

For a complete list of available materials, visit aldrich.com/perovskites.

Organoiodide Materials

Name	Composition	Description	Purity	Prod. No.
Acetamidinium iodide	C ₂ H ₇ IN ₂	powder	98%	805971-25G
Benzylammonium iodide	C ₇ H ₁₀ IN	powder	98%	806196-25G
<i>n</i> -Butylammonium iodide	C ₄ H ₁₂ IN	powder	98%	805874-25G 805874-5G
<i>t</i> -Butylammonium iodide	C ₄ H ₁₂ IN	powder	98%	806102-25G
<i>i</i> -Butylammonium iodide	C ₄ H ₁₂ IN	powder	98%	805866-25G 805866-5G
Diethylammonium iodide	C ₄ H ₁₂ IN	powder	98%	806188-25G
Dimethylammonium iodide	C ₂ H ₈ IN	powder	98%	805831-25G 805831-5G
Formamidinium iodide	CH ₃ IN ₂	powder	≥98%	806048-25G
Guanidinium iodide	CH ₅ IN ₃	powder	-	806056-25G 806056-5G
Imidazolium iodide	C ₃ H ₅ IN ₂	powder	98%	805963-25G
Methylammonium bromide	CH ₅ BrN	powder	98%	806498-25G
	CH ₅ BrN	powder	98%	793507-5G
Methylammonium bromide solution	CH ₅ BrN	0.18 M in 2-propanol	-	808407-50ML
Methylammonium chlorodiodoplumbate(II) precursor solution	CH ₅ NCI ₂ Pb	8.6 wt. % (Pb in DMF)	-	809039-25G
Methylammonium iodide	CH ₅ IN	powder	98%	793493-5G
	CH ₅ IN	powder	-	806390-25G
Methylammonium triiodoplumbate(II) precursor solution	CH ₅ I ₃ NPb	40 wt. % in DMF	-	793833-5ML
Phenethylammonium iodide	C ₈ H ₁₂ IN	powder	≥98%	805904-25G
Phenylammonium iodide	C ₆ H ₈ IN	powder	≥98%	805912-25G
<i>n</i> -Propylammonium iodide	C ₃ H ₁₀ IN	powder	-	805858-25G 805858-5G
<i>i</i> -Propylammonium iodide	C ₃ H ₁₀ IN	powder	98%	805882-25G 805882-5G

Lead Halides

Name	Composition	Description	Prod. No.
Lead(II) bromide	PbBr ₂	powder; 99.999% trace metals basis	398853-5G
	PbBr ₂	powder; ≥98%	211141-100G 211141-500G
Lead(II) chloride	PbCl ₂	beads; 99.999%	449865-5G
	PbCl ₂	powder and chunks; 99.999% trace metals basis	203572-10G 203572-50G
	PbCl ₂	powder; 98%	268690-5G 268690-250G 268690-1KG
Lead(II) iodide	PbI ₂	beads; 99.999% trace metals basis	554359-5G
	PbI ₂	solid; 99.999% trace metals basis	203602-50G
	PbI ₂	powder; 99%	211168-50G
Lead(II) iodide solution	PbI ₂	solution; 0.55 M in DMF	795550-10ML

Titania Nanomaterials for Support

For a complete list of available materials, visit aldrich.com/nanopowders.

Name	Description	Purity	Form	Prod. No.
Titanium	particle size <100 nm	98.5% trace metals basis	dispersion nanoparticles	513415-5G
Titanium dioxide	particle size 22 - 25 nm (BET) spec. surface area 65-75 m ² /g (BET)	>95% (anatase (XRD))	paste (nanocrystalline colloid)	798495-25G
	particle size 18 - 20 nm (BET) spec. surface area 75-85 m ² /g (BET)	-	paste (nanocrystalline colloid)	798509-25G
	spec. surface area 50-60 m ² /g (BET)	-	paste (nanocrystalline colloid)	798517-25G
	particle size 18 - 20 nm (BET) spec. surface area 60-70 m ² /g (BET)	>95% (anatase(XRD))	paste (nanocrystalline colloid)	798525-25G
	average diameter 25 nm	-	nanotubes powder	799289-500MG
Titanium(IV) oxide	primary particle size 21 nm (TEM), surface area 35-65 m ² /g (BET)	≥99.5% trace metals basis	nanopowder	718467-100G
Titanium(IV) oxide, anatase	particle size <25 nm, spec. surface area 45-55 m ² /g	99.7% trace metals basis	nanopowder	637254-50G 637254-100G 637254-500G
Titanium(IV) oxide, mixture of rutile and anatase	particle size <100 nm (BET) particle size <50 nm (XRD)	99.5% trace metals basis	nanopowder	634662-25G 634662-100G
	particle size ~21 nm (primary particle size of starting nanopowder) particle size <250 nm (DLS), BET surf. area 50 m ² /g (BET surface area of starting nanopowder)	99.9% trace metals basis	nanoparticle paste	700355-25G
	particle size <150 nm (volume distribution, DLS) particle size ~21 nm (primary particle size of starting nanopowder)	99.5% trace metals basis	dispersion nanoparticles	700347-25G 700347-100G
	particle size <100 nm particle size ~30 nm (primary particle size of starting nanopowder)	99.9% trace metals basis	dispersion nanoparticles	700339-100G
	Titanium(IV) oxide, rutile	particle size <100 nm, spec. surface area 50 m ² /g	99.5% trace metals basis	nanopowder

Inorganic 2D Materials

For a complete list of available materials, visit aldrich.com/periodic.

Name	Composition	Description	Purity	Prod. No.
Molybdenum diselenide	MoSe ₂	crystals	99.995%	808660-1EA
Molybdenum disulfide	MoS ₂	crystals	99.995%	808652-1EA
Molybdenum telluride	MoTe ₂	crystals	99.995%	808814-1EA
Niobium diselenide	NbSe ₂	crystals	99.995%	808679-1EA
Rhenium disulfide	ReS ₂	crystals	99.995%	808695-1EA
Tantalum diselenide	TaSe ₂	crystals	99.995%	808733-1EA
Titanium disulfide	TiS ₂	crystals	99.995%	808717-1EA
Tungsten diselenide	WSe ₂	crystals	99.995%	808822-1EA
Tungsten disulfide	WS ₂	crystals	99.995%	808806-1EA

Organic Hole Transport Materials

For a complete list of available materials, visit aldrich.com/dssc.

Name	Description	Prod. No.
Spiro-MeOTAD	99%, HPLC, λ_{abs} 385 nm in dichloromethane λ_{abs} 306 nm in dichloromethane	792071-1G 792071-5G
2,2',7,7'-Tetrakis(N,N-diphenylamino)-9,9-spirobifluorene	99%, HPLC, absorption 378 nm in THF	765007-1G
Poly(3-hexylthiophene-2,5-diyl)	regioregular	445703-1G
	99.995% trace metals basis, electronic grade, average M_n 54,000-75,000, regioregular	698997-250MG 698997-1G 698997-5G
	99.995% trace metals basis, electronic grade, average M_n 15,000-45,000, regioregular	698989-250MG 698989-1G 698989-5G
	regiorandom	510823-1G
Polyaniline (emeraldine salt)	30 wt.% polyaniline on nylon	577073-10G
	20 wt.% polyaniline on carbon black	530565-5G 530565-25G
Polypyrrole	coated on titanium dioxide doped, proprietary organic sulfonic acid as dopant	578177-10G
	proprietary organic sulfonic acid as dopant	577030-5G 577030-25G
	composite with carbon black doped, proprietary organic sulfonic acid as dopant	530573-25G
	5 wt % dispersion in H ₂ O, doped, proprietary organic acids as dopant	482552-100ML
Polypyrrole- <i>block</i> -poly(caprolactone)	0.3-0.7 wt. % (dispersion in nitromethane), <i>p</i> -toluenesulfonate as dopant	735817-25G

Hole Conductor Cobalt Dopants

For a complete list of available materials, visit aldrich.com/perovskite.

Name	Purity	Prod. No.
FK 102 Co(II) PF ₆ salt	98%	805238-5G
FK 102 Co(II) TFSI salt	98%	805246-5G
FK 102 Co(III) PF ₆ salt	>98%	805254-5G
FK 102 Co(III) TFSI salt	98%	805203-5G
FK 209 Co(II) PF ₆ salt	98%	805378-5G
FK 209 Co(II) TFSI salt	98%	805386-5G
FK 209 Co(III) PF ₆ salt	98%	805408-5G
FK 209 Co(III) TFSI salt	98%	805394-5G
FK 269 Co(II) PF ₆ salt	98%	805548-5G
FK 269 Co(II) TFSI salt	98%	805815-5G
FK 269 Co(III) PF ₆ salt	98%	805521-5G
FK 269 Co(III) TFSI salt	98%	805807-5G

Fluorine-doped Tin Oxide Coated Glass Slides

For a complete list of available materials, visit aldrich.com/fto.

L × W × D (mm)	Surface Resistivity (Ω/sq)	Haze (%)	Transmittance (% visible)	Prod. No.
50 × 50 × 2.2	~7	5	80-82	735140-5EA
100 × 100 × 2.3	~7	5	80-82	735159-5EA
300 × 300 × 2	~7	5	80-82	735167-1EA
50 × 50 × 3	~8	12	80-81.5	735175-5EA
100 × 100 × 3	~8	12	80-81.5	735183-5EA
300 × 300 × 3.2	~8	12	80-81.5	735191-1EA
50 × 50 × 3	~10	1	83	735205-5EA
100 × 100 × 3	~10	1	83	735213-5EA
300 × 300 × 3	~10	1	83	735221-1EA
50 × 50 × 2.2	~13	≤0.74	82-84.5	735248-5EA
100 × 100 × 2	~13	≤0.74	82-84.5	735256-5EA
300 × 300 × 2.3	~13	≤0.74	82-84.5	735264-1EA

GRAPHENE AND OTHER 2D CRYSTALS

FOR RECHARGEABLE BATTERIES



Francesco Bonaccorso,* Vittorio Pellegrini
Istituto Italiano di Tecnologia, Graphene Labs, 16163, Genova, Italy
*Email: francesco.bonaccorso@iit.it

Introduction

Advanced technologies for energy conversion and storage are widely sought after for their potential to improve consumer and electronic device performance as well as for the prospect of reducing the societal and environmental impact of energy generation. Rechargeable batteries already power a wide range of applications from portable electronics to automotive systems.¹ But these applications are still hindered by battery performance limitations that include inadequate power and energy density, limited lifetime, slow recharging, high cost, and limitations in battery shape and physical flexibility. In order to address these challenges, novel materials for anodes and cathodes will be required. Lithium-ion batteries (LIBs) currently dominate the market,² with most commercial LIBs comprised of a LiCoO_2 cathode on aluminum substrate and a graphite anode on copper. This configuration yields a theoretical specific energy density of 387 Wh kg^{-1} and a measured energy density of $120\text{--}150 \text{ Wh kg}^{-1}$,³ much higher than what can be achieved by other battery types such as lead acid ($\sim 30 \text{ Wh kg}^{-1}$)⁴ and nickel metal hydrides ($45\text{--}68 \text{ Wh kg}^{-1}$).¹ Other promising oxide host structures identified but not yet commercialized in batteries include layered $\text{Li}_{1-x}\text{MO}_2$ ($M = \text{Ni, Mn, Co}$),⁵ spinel LiMn_2O_4 ,⁶ and ordered olivine $\text{Li}_{1-x}\text{MPO}_4$ ($M = \text{Fe, Mn, Ni}$).⁷

Graphene and several related two-dimensional (2D) crystals can boost the performance of LIBs and improve cyclability either as stand-alone materials^{8,9} or when integrated with other materials to form functional composites.^{10,11} Besides graphene, a number of 2D crystals have recently been investigated, including transition metal dichalcogenides (TMDs),¹² transition metal oxides (TMOs),¹³ layered double hydroxides (LDHs),^{14,15} and MXenes.¹⁶ Among these new materials, graphene-silicon nanoparticle (NP) composites show significant promise and have attracted substantial attention.¹⁷ The theoretical reversible specific capacity of silicon, measured as the total ampere-hours per gram (mAh g^{-1}) available during controlled discharge, approaches $4,000 \text{ mAh g}^{-1}$,¹⁸ one of the highest values among potential anode materials. However, silicon and nanostructured silicon-based anodes also suffer from material degradation and significant capacity fading due to volume contraction and expansion during the charge/discharge cycling.¹⁹ This issue can be limited by using graphene to fabricate hybrid anodes where graphene secures well-dispersed particles and forms a conductive matrix between them.

The potential of graphene and other 2D crystals²⁰ is not limited to conventional lithium-ion batteries. Sulfur-, tin-, sodium-, and zinc-based batteries can also benefit by the incorporation of 2D crystals from a cost perspective, potentially allowing them to compete with lithium-ion technology.²¹ Graphene and other 2D crystals also can be used to improve the electrochemical performance of Li-air batteries.^{22,23} For example, the incorporation of porous reduced graphene oxide (RGO) results in the highest stability achieved in such an electrode, and is a very promising early utilization of RGO technology.¹⁹ However, further studies are needed to assess reproducibility and scalability.^{19,21}

The role of graphene and other 2D crystals is not limited to improving reversible specific capacity or specific energy density in batteries.¹⁰ In fact, graphene can be used to form conductive films to replace metal supports both in cathodes and anodes, reducing overall battery weight. Thus, the exploitation of graphene and other 2D crystals can allow for the development of conformable and transparent batteries with enormous potential for wearable electronics,²⁴ smart tissues,²⁵ and biomedical applications like implantable prosthetic devices in the long-term.¹¹

Much of the current research is focused on developing a clear understanding of the charge storage mechanism of graphene, other 2D crystals, and their composites in order to limit irreversible processes.^{16,21} Subsequently, the ability to go into commercial application of these 2D materials will be linked to exceptional and consistent morphology, electrical properties, purity, and cost.²⁶ In the next few years it will be crucial to determine the best lab-scale solution that can effectively be scaled up to develop viable commercial products.

We present a comprehensive review of the current state of the art of graphene and other 2D crystals used in the development of next-generation batteries, outlining the key issues to be explored in an effort to identify future directions. We also discuss how the versatility of 2D crystal-based technology can boost the development of new power management solutions for portable and flexible devices.

Production of 2D Crystals for the Fabrication of Functional Electrodes

One of the most important material requirements for developing energy storage devices, and batteries in particular, is the combination of high specific surface area (SSA)²⁷ and high electrical conductivity (σ)²⁸ associated with the prospect of large scale manufacturing.²⁶ Two-dimensional crystals that meet such requirements can be produced by bottom-up^{29,30} and top-down^{11,13,26} techniques, offering complementary opportunities for renewable energy technologies. Here, we briefly focus on liquid phase exfoliation (LPE), a production strategy that is both affordable and highly scalable, making it appropriate for batteries and other energy devices.

Liquid Phase Exfoliation

Direct exfoliation of layered crystals (Figure 1A) in solution²⁰ is considered a preferred production route for energy applications because of its low cost, scalability, and potential for functionalization. The exfoliation of layered crystals is usually carried out via ultrasonication (Figure 1B)^{8,13,20,26,31–33} in water with the aid of surfactants/polymers,^{31,32} or in organic solvents.^{8,9,34,35} Other exfoliation approaches such as shear mixing,³⁷ ball milling,³⁸ as well as electrochemical processes^{39,40} have been proposed as alternative scale-up methods.

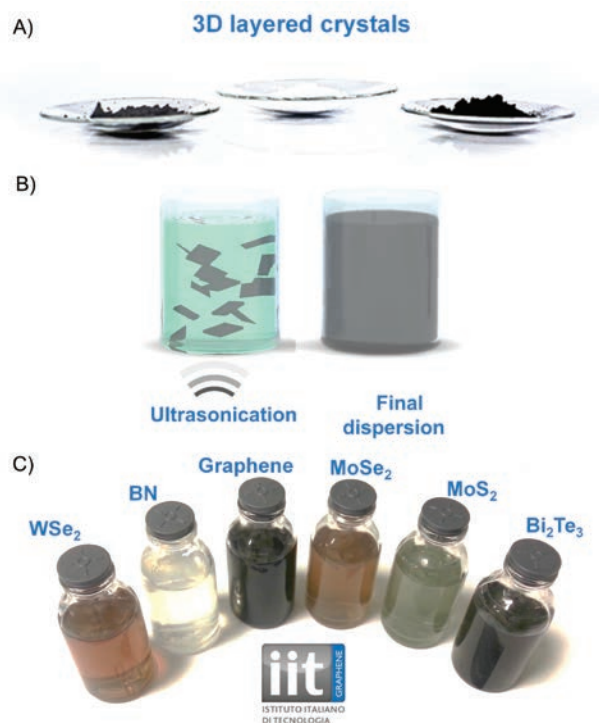


Figure 1. Process chain from the exfoliation of bulk-layered crystals to functional inks. **A)** Layered bulk crystals. **B)** Exfoliation of layered crystals by ultrasonication. **C)** Photograph of different 2D crystal inks.

After exfoliation, the obtained dispersions are “purified” via ultracentrifugation⁴¹ in order to separate exfoliated and unexfoliated flakes. This ultracentrifugation is also a powerful tool for the separation of large, thick³⁴ flakes from small, thin^{8,31,32,35} flakes.

A high concentration of 2D crystals in solution is desirable for the large-scale production of composites⁴² and inks³¹ used in the fabrication of functional electrodes for battery applications (Figure 1C). Following ultracentrifugation, a concentration of ~15 mg/mL for graphitic sheets³² and ~40 mg/mL for MoS₂⁴³ flakes can be achieved. A dispersion highly enriched by single-layer graphene (SLG) is achieved by sonication and ultracentrifugation in water-surfactant dispersion in a uniform (SLG ~60%)³¹ and a density gradient (SLG ~80%)³² medium. Surfactants³⁹ and polymers^{44,45} allow for improved control of the morphological properties (lateral size³¹ and thickness³²) of the dispersed flakes and also help to avoid aggregation—the main factor limiting the SSA of the as-produced materials. However, a high SSA also brings disadvantages when the material is used in batteries. For example, high SSA favors the formation of solid electrolyte interphase and leads to very high initial irreversible capacity.^{14,46} Moreover, the presence of surfactants/polymers is not

optimal for device integration, especially when preservation of the pristine electronic properties of the flakes is important, e.g., in LIB electrodes. The presence of surfactants and/or polymers decreases the inter-flake connectivity, strongly affecting the σ of the electrodes.²³ One significant disadvantage of the LPE of 2D crystals is a reliance on solvents with high boiling points, high toxicity, and/or incompatibility with deposition onto current collectors such as copper and aluminum. To overcome such limitation, LPE of 2D crystals has recently been carried out in a mixture of low boiling point solvents⁴⁷ such as water/ethanol^{45,47,48} or water/isopropyl alcohol.⁴⁷ By adjusting the relative concentration of the co-solvents, it is possible to tune the rheological properties such as density, viscosity, and surface tension of the 2D crystal dispersions/inks. LPE is also utilized to create dispersions of graphite intercalated compounds⁴⁹ formed by periodic insertion of atomic or molecular species (intercalants) between graphite layers⁵⁰ and is largely used in LIBs.⁴⁶ Graphite intercalated compounds can be processed with donor or acceptor intercalants to yield highly conductive materials ($\sigma = 6.3 \times 10^5 \text{ S cm}^{-1}$).⁵¹ Moreover, tunability of the interlayer spacing (e.g., from 0.53–0.59 nm with potassium, rubidium, or cesium up to ~0.9 nm with dimethylsulfoxide⁵²) permits the accommodation of large amounts of lithium ions.

LPE can also be exploited to produce graphene oxide (GO).⁵³ Graphene oxide contains extended aromatic frameworks and multiple functional groups such as hydroxyl or epoxide groups with carboxylic or carbonyl groups attached to the edges.⁵⁴ These functional groups render GO readily dispersible in water and other common solvents, and provide reaction sites for chemical modification,⁵³ i.e., covalent attachment of organic and inorganic nanoparticles. Several processes have been developed to chemically reduce or decrease the oxidation state of the oxygen-containing groups in the GO flakes.⁵⁵ Even though RGO does not achieve the same σ as pristine graphene,⁵⁵ it is still widely being explored by researchers for the fabrication of electrodes for lithium-ion and other technologies.¹⁰ Unfortunately, the reduction state strongly influences the final electrochemical performance of RGO as an anode material. Indeed, the further removal of functional groups during battery operation results in a re-stacking of the graphene layers, reducing the storage capacity and, thus, reversible capacity during cycling.⁵⁶

Storage Mechanisms and Current State-of-the-Art Electrochemical Performances

LIBs are based on the capture and release of lithium ions.^{1–3} Current LIBs are typically composed of an intercalated lithium compound cathode (e.g., LiCoO₂ or LiFePO₄), a graphitic anode, and an electrolyte.^{1–3} During the charging mode, lithium ions travel from cathode to anode through the electrolyte upon application of an external electrical potential.^{1–3} In the reverse process, lithium ions are extracted from the graphitic electrode and migrate toward the cathode.^{1–3} Electrons traveling in the external circuit can be used to power devices and perform external work.^{1–3} The gravimetric capacity to store lithium ions (i.e., the weight percentage of stored lithium per gram of battery weight) is crucial to the performance of these rechargeable batteries. Compared with graphite, graphene and other 2D crystals have a larger theoretical gravimetric capacity.¹⁸ Additionally, the use of graphene provides additional flexibility that enables further development of bendable and stretchable battery devices.⁵⁷ Other relevant properties of 2D crystals are their high σ , and the electrochemical and thermal stability within the operational temperature range (–50/100 °C). LIBs are ideal for applications in which high energy density (~200 Wh kg⁻¹, typically more than one order of magnitude larger than that of supercapacitors, see Figure 2) is needed.

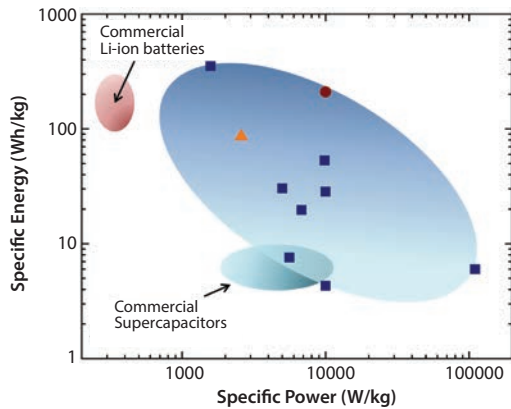


Figure 2. Ragone-like plot⁵⁸ showing energy (Wh/kg) vs. power (W/kg) densities for batteries and supercapacitors. The blue ellipse encloses the region of energy/power density values of available 2D crystal-based storage devices. Inside the ellipse, the circular dot refers to a lithium-ion battery,⁵⁹ the orange triangle to a hybrid supercapacitor-battery,⁶⁰ and the blue squares to supercapacitors.⁶¹ The smaller white and cyan elliptical areas refer to values for commercial LIBs⁶² and supercapacitors,⁶¹ respectively. It is important to stress that it is problematic to compare packaged commercial cells (the mass includes the electrodes/package/electrolyte with performance measured using industry standards) with 2D crystal-based devices considered for the plot that include only the electrode material. When packaging and measurement methods are accounted for, these devices could have lower energy and power densities than shown on the diagram.

2D Crystals as Cathode and Anode Materials in LIBs

Graphene and other 2D crystals are emerging as promising materials for both anodes^{8–10,63} and cathodes⁶⁴ in LIBs (Figure 3A). For example, graphene and other 2D crystals can be used as an electrically conductive support for cathode nanomaterials such as olivine-type phosphates (consisting of a hexagonal closed-packing of oxygen atoms with Li⁺ and M²⁺ cations located in 1/2 of the octahedral sites and P⁵⁺ cations in 1/8 of the tetrahedral sites),^{65,66} with low σ ($\sim 10^{-8}$ S cm⁻¹).⁶⁷ This is because electrically conductive 2D crystals such as graphene and RGO (Figure 3B) facilitate electron transport between conductive 2D crystals and cathode nanomaterials, allowing the fabrication of electrodes with higher electrochemical performance.⁶³

Although a conductive 2D crystal matrix can enhance the σ of a composite material and improve the rate capability compared to bare cathode materials,⁶⁵ the method of composite fabrication is fundamental to the final electrochemical performance of the resulting cathode. In fact, it has been shown that mixing RGO according to the standard procedure used for carbon black can actually reduce Li⁺ mobility, affecting the electrochemical performance of the hybrid cathode.⁶⁸ Several attempts to engineer the hybrid cathode material with RGO as an electrically conductive support have been carried out.⁶⁹ LiMn_{1-x}Fe_xPO₄ nanorods grown on RGO flakes show a reversible specific capacity of ~ 100 mAh g⁻¹ at the rate of 50 C, with stable operation, i.e., 1.9% degradation for 100 cycles.⁶⁵ A similar approach to create hybrid electrodes was applied to different materials, such as spinels like LiMn₂O₄.⁶⁹ The hybrid RGO/LiMn₂O₄ cathode shows a high specific capacity of 137 mAh g⁻¹ at 1 C rate (a measure of the speed at which a battery is discharged relative to its maximum capacity), with remarkable performances also at faster charge/discharge rates of 50 C and 100 C, delivering discharge capacities of 117 mAh g⁻¹ and 101 mAh g⁻¹, respectively.⁶⁹

RGO is currently one of the most commonly used 2D crystal materials deployed in LIB anodes (Figure 3C).⁷⁰ During the first cycle, the RGO anode can display capacities well above the theoretical limit of SLG. However, this large initial capacity is linked to the irreversible reduction of the electrolyte and the formation of a surface passivation layer likely

favoured by the presence of large amounts of structural defects and functional groups.^{26,53–55} A reversible specific capacity of RGO-based electrodes of 540 mAh g⁻¹,⁷⁰ far below the theoretical value of graphene,¹⁰ has been demonstrated.

More recently, graphene flakes produced by LPE of pristine graphite have been used for the preparation of anodes.^{9,10} Edges and defects can potentially act as reversible storage sites of Li, contributing to the reversible specific capacity of the graphene-based electrodes. Graphene electrodes show faster C rates⁶¹ with respect to graphite, mainly due to decreased energy barriers for lithium diffusion at the graphene flake edges.^{8,71} Hassoun et al. have demonstrated a reversible specific capacity of ~ 750 mAh g⁻¹ with a current density of 700 mA g⁻¹ using an anode made of exfoliated graphene flakes with a lateral size finely tuned to less than 100 nm.⁹ This configuration resulted in the uptake of lithium ions both on the basal planes and on the edges of the flakes.⁸ The graphene flake-based anode shows optimal performance in a full cell configuration, achieving a reversible specific capacity of 165 mAh g⁻¹ and an estimated energy density of ~ 190 Wh kg⁻¹, with stable operation for over 80 charge/discharge cycles.⁸ Graphene flakes produced by LPE have also proven to be effective anode materials in a binder-free configuration, achieving a reversible specific capacity of ~ 500 mAh g⁻¹ after 100 cycles at a current density of 100 mA g⁻¹, with a coulombic efficiency of $>99.5\%$.⁹

Graphene and other 2D crystals have also been used for hybrid anode fabrication to increase the charge/discharge capacity of LIBs by mixing electrochemically active particles such as alloy-type anodes,⁷² silicon,^{73,74} sulfur,⁷⁵ Co₃O₄,⁷⁶ Li₃VO₄,⁷⁷ Fe₃O₄,⁷⁸ with graphene and other 2D crystals.

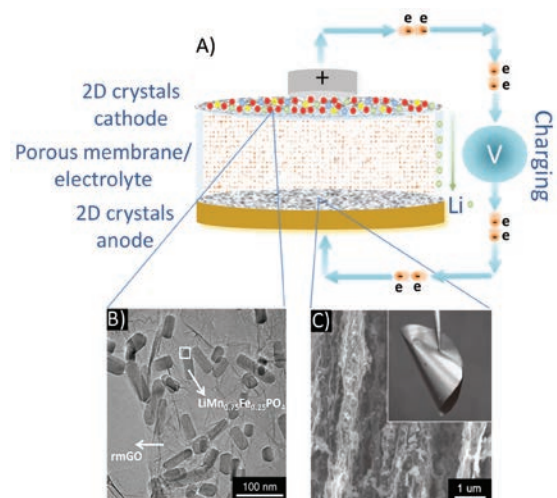


Figure 3. Representative strategies for graphene and 2D crystal-based battery electrodes. A) Schematic of a battery consisting of graphene and 2D crystal electrodes (anodes and cathodes) in a charging state. B) Graphene as substrate for the growth of electrochemically active materials for lithium-ion batteries.⁶⁵ C) Hybrid GO/silicon composite electrode.⁷⁹

Both graphene flakes and RGO can suppress NP aggregation by accommodating their volume expansion/contraction upon lithiation/de-lithiation while supplying high conductivity to the hybrid anodes. As a consequence, the reversible specific capacity and cycling performance of hybrid anodes, such as graphene/Co₃O₄,⁷³ RGO/sulfur,⁸⁰ RGO/Li₃VO₄,⁷⁴ and RGO/Fe₃O₄,⁷⁵ can be greatly improved compared to electrodes made of these NPs alone.

Other 2D crystals, such as TMDs,⁸¹ TMOs,⁸² and transition metal hydroxides (TMHs)⁸³ are also promising lithium-ion battery materials due to their fast ion conductivity and ability to intercalate lithium ions.¹⁶ For example, a reversible specific capacity of ~ 800 mAh g⁻¹ and ~ 470 mAh g⁻¹ has been demonstrated for MoS₂⁷⁸ and WS₂⁸⁴ anodes, respectively. ZrS₂ colloidal nanodisks with a diameter of ~ 20 nm delivered a reversible specific capacity of ~ 600 mAh g⁻¹.⁸⁵ A hybrid WS₂/RGO composite was used as

an electrode and achieved a reversible specific capacity of $\sim 240 \text{ mAh g}^{-1}$ at a high current density up to 4 A g^{-1} .⁸⁶ Among TMOs, lithiated MoO_3 nanobelts show a specific capacity of $\sim 220 \text{ mAh g}^{-1}$ at a current density of 30 mA g^{-1} after 15 cycles, with a capacity retention of 92%.⁸⁷ However, the lithiation process is not yet fully understood, with the interaction of lithium ions with the oxygen atoms controlling the reversible and irreversible intercalation/uptake processes.

Other Technologies (Air, Sodium, Flexible)

Lithium Air

Lithium-air batteries, commonly composed of metallic lithium and oxygen (or air) as anode and cathode, respectively offer a theoretical energy density of $5,200 \text{ Wh kg}^{-1}$,⁸⁸ much higher than what is achievable using metal-ion batteries.² This high theoretical energy density results from the pairing of lithium and oxygen from air⁸⁹ and makes lithium-air batteries one of the most promising technologies for the development of next-generation batteries.

However, despite a promising theoretical energy density, lithium-air batteries have a number of performance issues that must be addressed before successful commercialization. These limitations include short lifetime, limited rate capability (e.g., only about 100 cycles), and low energy efficiency. The morphology of the cathode (air electrode) is currently believed to be a critical limiting factor to the improved performance of lithium-air batteries. In fact, both the porosity and SSA of the cathode determine the morphology and amount of the reduction products resulting from the discharge process.

Incorporation of graphene and other 2D crystals has shown promise in addressing the limitations of lithium-air batteries and improving their performance. For example, RGO used as a cathode material can deliver higher capacities than other carbon substrates.⁹⁰ In particular, the use of RGO in combination with other catalysts such as $\text{RuO}_2 \cdot 0.64\text{H}_2\text{O}$ -RGO hybrids⁹¹ in lithium-air battery cathodes is very promising. This intriguing combination results in a reversible specific capacity of $5,000 \text{ mAh g}^{-1}$ at a charge potential of $\sim 3.7 \text{ V}$ and high current density of 500 mA g^{-1} .⁸⁹ A very recent work has shown that RGO electrodes can help reversibly form and remove crystalline LiOH during discharge and charge, leading to high specific capacity and improved rechargeability.⁹²

Sodium Ion

Since sodium is a more abundant element than lithium, sodium-ion batteries have the potential to become a cheaper alternative to lithium-ion batteries. Graphite, the most common anode material in lithium-ion technology, however, is not a suitable active anode material for use in sodium-ion batteries. Because of its large ionic radius, Na^+ ions do not intercalate into graphite.⁹³ This drawback is stimulating research aimed at exploring the use of graphene-based materials in which the interlayer distance can be tuned and optimized for Na^+ intercalation and up-take.⁹³ Promising results have been obtained with RGO, yielding a specific capacity of $\sim 100 \text{ mAh g}^{-1}$ at a current density of 200 mA g^{-1} after 250 cycles.⁹⁴ Moreover, anodes made by highly ordered graphitic structures with a large graphene interlayer spacing have reached a specific capacity of $\sim 300 \text{ mAh g}^{-1}$ at a current density of 50 mA g^{-1} after 10 cycles, reinforcing the crucial role of interlayer spacing in graphene-based anodes for sodium ion batteries.⁹⁵ However, the use of graphene and 2D crystals in sodium-ion batteries, both as active anode materials and as an electrical support at the cathode, is at an early stage. More extensive research is needed to define the effectiveness of this approach.

Flexible Batteries

The development of flexible and/or stretchable battery devices⁹⁶ is strongly dependent upon the development of flexible electrodes with robust mechanical properties. Such devices must be able to accommodate significant strain²² while retaining their function. These next-generation batteries must also have high reversible specific capacity and energy efficiency coupled with a long cycle life and low cost. These requirements make the development of flexible batteries particularly challenging using current technologies. In fact, the process used to prepare a conventional electrode, including the steps of mixing those compositions (i.e., active material, carbon black and binder), coating the mixture onto the current collector, post-drying, and pressing, is time-consuming and expensive. In addition, the post-drying (annealing) process poses a strong limitation due to the small temperature range the substrate itself can sustain to fabricate flexible electrodes or flexible supports. Moreover, a flexible electrode must contain the precise amount of binder and carbon black⁹⁰ in order to obtain good flexibility, σ , as well as adhesion between the electrode and the current collector. In this context, it is necessary to envisage novel materials and production processes for the fabrication of electrochemically performant flexible electrodes.

Graphene and other 2D crystals may be a viable strategy for the realization of a flexible and stretchable battery. For example, layer-by-layer assembly of a 3D flexible conducting scaffold loaded with silicon nanoparticles showed a reversible specific capacity of $1,100 \text{ mAh g}^{-1}$ at a discharge current of 8 A g^{-1} .⁹¹ The device was also tolerant to structural deformation.⁹⁷

Cheng and co-workers⁵⁷ demonstrated a thin, lightweight, flexible lithium-ion battery based on a flexible, conductive, interconnected 3D graphene foam network produced by chemical vapor deposition. The foam network served as both a highly conductive pathway for electrons/lithium ions and as a lightweight current collector. After filling the 3D graphene foam with active materials leading to $\text{LiFePO}_4/\text{graphene}$ and $\text{Li}_4\text{Ti}_5\text{O}_{12}/\text{graphene}$ electrodes as cathode and anode, respectively, a flexible battery was demonstrated.⁵⁷ The assembled battery operated at a voltage of 1.9 V , with an initial discharge capacity of $\sim 143 \text{ mAh g}^{-1}$ and a coulombic efficiency of 98% at a 0.2 C rate.⁵⁷ The 3D graphene foams replaced various inactive components of the battery such as the metal current collectors, conducting additives, and binders.⁵⁷

The development of such flexible batteries is still at an early stage, and the inclusion of graphene and other 2D crystals into different components of the battery⁵⁷ is even more recent. There is still a long way to go before a reliable solution for the fabrication of transparent and flexible batteries based on graphene and other 2D crystals is identified. Without doubt, a transparent and flexible battery has the potential to deeply impact many areas of technology and consumer products. For example, a flexible and transparent battery could be coupled with computer/smart phone/PDA displays to make more compact and user-friendly electronics, integrating hidden energy harvesting and storage capability. Another example, conceptual products such as flexible and transparent communication devices, biosensors, and other concepts are now highly limited by rigid and opaque batteries, likely the most difficult component to make flexible and transparent at the same time. Batteries with conformable configurations will be very important to fit into the next generation of electronics with different form factors, and here graphene and 2D crystals could play a key role.

Perspective

Graphene and other 2D crystals have the potential to impact practical energy storage systems such as LIBs by increasing their energy and power densities, cyclability, and cost, as well as enabling the development of next-generation batteries such as lithium-air and flexible batteries. However, there are many issues that still need to be addressed, and there is ample room for significant breakthroughs in the field. While promising results at the laboratory level are creating high expectations, the gap between laboratory-scale research and commercial applications based on 2D crystals has yet to be closed. The challenges ahead are linked to the refinement of the production methods to better understand and control fundamental issues such as lithium adsorption and solid electrolyte interface formation, the role of lateral sizes and number of layers of the flakes, optimization of graphene-based composites, and fine tuning inter-layer distances of the 2D crystals flakes through appropriate functionalization of the flakes themselves, with the aim to push storage densities and cyclability to the highest possible values. Another challenge is the scale-up and manufacture of these emerging technologies. These listed here are some of the goals to reach before 2023, as set by the European Graphene Flagship.¹¹

Acknowledgments

The authors acknowledge Bruno Scrosati, Reza Fathi, Simone Monaco and Haiyan Sun for discussions and funding from the European Union Seventh Framework Programme under grant agreement n°604391 Graphene Flagship.

References

- Burke, A. F. *Proc. IEEE* **2007**, *95*, 806–820.
- Scrosati, B.; Garche, J. *J. Power Sources* **2010**, *195*, 2419–2430.
- Bruce, P. G.; Freunberger, S. A.; Hardwick, L. J.; Tarascon, J. M. *Nat. Mater.* **2012**, *11*, 19–29.
- Divya, K. C.; Oostergaard, J. *Electr. Pow. Syst. Res.* **2009**, *79*, 511–520.
- Ohzuku, T.; Makimura, Y. *Chem. Lett.* **2001**, *30*, 642–643.
- Thackeray, M. M.; David, W.; Bruce, P. G.; Goodenough, J. B. *Mater. Res. Bull.* **1983**, *18*, 461–472.
- Padhi, A. K.; Nanjundaswamy, K. S.; Goodenough, J. B. *J. Electrochem. Soc.* **1997**, *144*, 1188–1194.
- Hassoun, J.; Bonaccorso, F.; Agostini, M.; Angelucci, M.; et al. *Nano Lett.* **2014**, *14*, 4901–4906.
- Sun, H.; Del Rio Castillo, A. E.; Monaco, S.; Capasso, A.; et al. *J. Mater. Chem. A* **2016**, DOI: 10.1039/C5TA08553E.
- Bonaccorso, F.; Colombo, L.; Yu, G.; Stoller, M.; Tozzini, V.; Ferrari, A. C.; Ruoff, R. S.; Pellegrini, V. *Science* **2015**, *347*, 1246501.
- Ferrari, A. C.; Bonaccorso, F.; Fal'ko, V.; Novoselov, K. S.; et al. *Nanoscale* **2015**, *7*, 4598–4810.
- Jariwala, D.; Sangwan, V. K.; Lauhon, L. J.; Marks, T. J.; Hersam, M. C. *ACS Nano* **2014**, *8*, 1102–1120.
- Nicolosi, V.; Chhowalla, M.; Kanatzidis, M. G.; Strano, M. S.; Coleman, J. N. *Science* **2013**, *340*, 1420.
- Abellán, G.; Martí-Gastaldo, C.; Ribera, A.; Coronado, E. *Acc. Chem. Res.* **2015**, *48*, 1601–1611.
- Liu, J.; Li, Y.; Huang, X.; Li, G.; Li, Z. *Adv. Funct. Mater.* **2008**, *18*, 1448–1458.
- Naguib, M.; Mochalin, V. N.; Barsoum, M. W.; Gogotsi, Y. *Adv. Mater.* **2014**, *26*, 992–1005.
- Son, I. H.; Park, J. H.; Kwon, S.; Park, S.; Rummeli, M. H.; et al. *Nat. Commun.* **2015**, *6*, 7393.
- Larcher, D.; Beattie, S.; Morcrette, M.; Edström, K.; Jumas, J.-C.; Tarascon, J.-M. *J. Mater. Chem.* **2007**, *17*, 3759–3772.
- Winter, M.; Besenhard, J. O.; Spahr, M. E.; Novak, P. *Adv. Mater.* **1998**, *10*, 725–763.
- Coleman, J. N.; Lotya, M.; O'Neill, A.; Bergin, S. D. et al., *Science* **2011**, *331*, 568–571.
- Raccichini, R.; Varzi, A.; Passerini, S.; Scrosati, B. *Nat. Mater.* **2015**, *14*, 271–279.
- Xiao, J.; Mei, D.; Li, X.; Xu, W.; et al. *Nano Lett.* **2011**, *11*, 5071–5078.
- Sun, B.; Wang, B.; Su, D.; Xiao, L.; Ahn, H.; Wang, G. *Carbon* **2012**, *50*, 727–733.
- Nathan, A.; Ahnood, A.; Cole, M. T.; Lee, S.; et al. *Proc. IEEE* **2012**, *100*, 1486–1517.
- Cataldi, P.; Bayer, I. S.; Bonaccorso, F.; Pellegrini, V.; Athanassiou, A.; Cingolani, R. *Adv. Electr. Mater.* **2015**, *1*, 1500224. doi: 10.1002/aeml.201500224
- Bonaccorso, F.; Lombardo, A.; Hasan, T.; Sun, Z.; Colombo, L.; Ferrari, A. C. *Mater. Today* **2012**, *15*, 564–589.
- Stoller, M. D.; Park, S.; Zhu, Y.; An, J.; Ruoff, R. S. *Nano Lett.* **2008**, *8*, 3498–3502.
- Geim, A. K.; Novoselov, K. S. *Nat. Mater.* **2007**, *6*, 183–191.
- Zhan, Y.; Liu, Z.; Najmaei, S.; Ajayan, P. M.; Lou, J. *Small* **2012**, *8*, 966–971.
- Wu, J.; Pisula, W.; Muellen, K. *Chem. Rev.* **2007**, *107*, 718–747.
- Maragó, O. M.; Bonaccorso, F.; Saija, R.; Privitera, G.; et al. *ACS Nano* **2010**, *4*, 7515–7523.
- Green, A. A.; Hersam, M. C. *Nano Lett.* **2009**, *9*, 4031–4036.
- Smith, R. J.; et al. *Adv. Mater.* **2011**, *23*, 3944–3948.
- Torrisi, F.; et al. *ACS Nano* **2012**, *6*, 2992–3006.
- Hernandez, Y.; Nicolosi, V.; Lotya, M.; Blighe, F. M. et al. *Nat. Nanotechnol.* **2008**, *3*, 563–568.
- Bonaccorso, F.; Balis, N.; Stylianakis, M. M.; Savarese, M.; et al. *Adv. Funct. Mater.* **2015**, *25*, 3870–3880.
- Paton, K. R.; Varrla, E.; Backes, C.; Smith, R. J.; et al. *Nat. Mater.* **2014**, *13*, 624–630.
- Fabbro, A.; Scaini, D.; Leon, V.; Vázquez, E.; et al. *ACS Nano* **2016**, *10*, 615–623.
- Lu, J.; Yang, J.-X.; Wang, J.; Lim, A.; Wang, S.; Loh, K. P. *ACS Nano* **2009**, *3*, 2367–2375.
- Parvez, K.; Wu, Z.-S.; Li, R.; Liu, X.; Graf, R.; Feng, X.; Müllen, K. *J. Am. Chem. Soc.* **2014**, *136*, 6083–6091.
- Bonaccorso, F.; Hasan, T.; Tan, P. H.; Sciascia, C.; Privitera, G.; Di Marco, G.; Gucciardi, P. G.; Ferrari, A. C. *J. Phys. Chem. C* **2010**, *114*, 17267–17285.
- Hasan, T.; Sun, Z.; Wang, F.; Bonaccorso, F.; Tan, P. H.; Rozhin, A. G.; Ferrari, A. C. *Adv. Mater.* **2009**, *21*, 3874–3899.
- O'Neill, A.; Khan, U.; Coleman, J. N. *Chem. Mater.* **2012**, *24*, 2414–2421.
- Guan, G.; Zhang, S.; Liu, S.; Cai, Y.; Low, M.; et al. *J. Am. Chem. Soc.* **2015**, *137*, 6152–6155.
- Vega-Mayoral, V.; Backes, C.; Hanlon, D.; Khan, U.; et al. *Adv. Funct. Mater.* **2015**, DOI: 10.1002/adfm.201503863
- Wu, Z.S.; Zhou, G.; Yin, L.-C.; ren, W.; Li, F.; Cheng, H.-M. *Nano Energy* **2012**, *1*, 107–131.
- Halim, U.; Zheng, C. R.; Chen, Y.; Lin, Z.; Jiang, S.; Cheng, R.; Huang, Y.; Duan, X. *Nat. Commun.* **2013**, *4*, 2213.
- Capasso, A.; Del Rio Castillo, A. E.; Sun, H.; Ansaldo, A.; Pellegrini, V.; Bonaccorso, F. *Solid State Commun.* **2015**, *224*, 53–63.
- Valles, C.; Drummond, C.; Saadaoui, H.; Furtado, C. A.; et al. *J. Am. Chem. Soc.* **2008**, *130*, 15802–15804.
- Dresselhaus, M. S.; Dresselhaus, G. *Adv. Phys.* **2002**, *51*, 1–186.
- Vogel, F. L. *J. Mater. Sci.* **1977**, *12*, 982–986.
- Lerf, A.; He, H.; Forster, M.; Klinowski, J. *J. Phys. Chem. B* **1998**, *102*, 4477–4482.
- Stankovich, S.; Piner, R. D.; Nguyen, S. T.; Ruoff, R. S. *Carbon* **2006**, *44*, 3342–3347.
- Dreyer, D. R.; Park, S.; Bielawski, C. W.; Ruoff, R. S. *Chem. Soc. Rev.* **2010**, *39*, 228–240.
- Mattevi, C.; Eda, G.; Agnoli, S.; Miller, S.; et al. *Adv. Funct. Mater.* **2009**, *29*, 2577–2583.
- Vargas, C. O. A.; Caballero, A.; Morales, J. *Nanoscale* **2012**, *4*, 2083–2092.
- Li, N.; Chen, Z.; Ren, W.; Li, F.; Cheng, H.-M. *Proc. Nat. Acad. Sci. USA* **2012**, *109*, 17360–17365.
- Ragone, D. V. Review of battery systems for electrically powered vehicles, SAE paper 680453, (1968).
- Lim, C. H.; Kannan, A. G.; Lee, H.-W.; Kim, D. K. *J. Mater. Chem. A* **2013**, *1*, 6183–6190.
- Zhang, F.; Zhang, T.; Yang, X.; Zhang, L.; Leng, K.; Huang, Y.; Chen, Y. *Energy Environ. Sci.* **2013**, *6*, 1623–1632.
- Wu, Z.-S.; Wang, D. W.; Ren, W.; Zhao, J.; Zhou, G.; Li, F.; Cheng, H.-M. *Adv. Funct. Mater.* **2010**, *20*, 3595–3602.
- <http://www.panasonic.com/industrial/batteries-oem/oem/lithium-ion.aspx>
- Vargas, O.; Caballero, A.; Morales, J.; Elia, G. A.; Scrosati, B.; Hassoun, J. *Phys. Chem. Chem. Phys.* **2013**, *15*, 20444–20446.
- Hu, L.-H.; Wu, F.-Y.; Lin, C.-T.; Klobystov, A. N.; Li, L.-J. *Nat. Commun.* **2013**, *4*, 1687.
- Wang, H.; Yang, Y.; Liang, Y.; Cui, L.-F.; Casalogue, H. S.; Li, Y.; Hong, G.; Cui, Y.; Dai, H. *Angew. Chem. Int. Ed.* **2011**, *123*, 7502.
- Ammundsen, B.; Paulsen, J. *Adv. Mater.* **2001**, *13*, 943–956.
- Rissouli, K.; Benkhoulja, K.; Ramos-Barrado, J. R.; Julien, C. *Mater. Sci. Eng. B* **2003**, *98*, 185–189.
- Kucinskis, G.; Bajars, G.; Kleperis, J. *J. Power Sources* **2013**, *240*, 66–79.
- Bak, S.-M.; Nam, K.-W.; Lee, C.-W.; Kim, K.-H.; Jung, H.-C.; Yang, X.-Q.; Kim, K.-B. *J. Mater. Chem.* **2011**, *21*, 17309–17315.
- Yoo, E.; Kim, J.; Hosono, E.; Zhou, H.-S.; Kudo, T.; Honma, I. *Nano Lett.* **2008**, *8*, 2277–2282.
- Uthaisar, C.; Barone, V. *Nano Lett.* **2010**, *10*, 2838–2842.
- Evanoff, K.; Magasinski, A.; Yang, J.; Yushin, G. *Adv. Energy Mater.* **2011**, *1*, 495–498.
- Chou, S.-L.; Wang, J.-Z.; Choucair, M.; Liu, H.-K.; Stride, J. A.; Dou, S.-X. *Electrochem. Commun.* **2010**, *12*, 303–306.
- Hu, R.; Sun, W.; Chen, Y.; Zeng, M.; Zhu, M. *J. Mater. Chem. A* **2014**, *2*, 9118–9125.
- Ji, L.; Rao, M.; Zheng, H.; Zhang, L.; Li, Y.; Duan, W.; Guo, J.; Cairns, E. J.; Zhang, Y. *J. Am. Chem. Soc.* **2011**, *133*, 18522–18525.
- Wu, Z. S.; Ren, W.; Wen, L.; Gao, L.; Zhao, J.; Chen, Z.; Zhou, G.; Li, F.; Cheng, H.-M. *ACS Nano* **2010**, *4*, 3187–3194.
- Shi, Y.; Wang, J.-Z.; Chou, S.-L.; Wexler, D.; Li, H.-J.; Ozawa, K.; Liu, H.-K.; Wu, Y.-P. *Nano Lett.* **2013**, *13*, 4715–4720.
- Zhou, G.; Wang, D.-W.; Li, F.; Zhang, L.; Li, N.; Wu, Z.-S.; Wen, L.; Qing, G.; Cheng, H.-M. *Chem. Mater.* **2010**, *22*, 5306–5313.
- Zhao, X.; Hayner, C. M.; Kung, H. H. *Adv. Energy Mater.* **2011**, *1*, 1079–1084.
- Wang, H.; Yang, Y.; Liang, Y.; Robinson, J. T.; et al. *Nano Lett.* **2011**, *11*, 2644–2647.
- Du, G.; Guo, Z.; Wang, S.; Zeng, R.; Chen, Z.; Liu, H. *Chem. Commun.* **2010**, *46*, 1106–1108.
- Wang, H.; Cui, L.-F.; Yang, Y.; Casalogue, H. S.; Robinson, J. T.; Liang, Y.; Cui, Y.; Dai, H. *J. Am. Chem. Soc.* **2010**, *132*, 13978–13980.
- Li, Y.; Gong, M.; Liang, Y.; Feng, J.; Kim, J.-E.; Wang, H.; Hong, G.; Zhang, B.; Dai, H. *Nat. Commun.* **2013**, *4*, 1805.
- Bhandavat, R.; David, L.; Singh, G. *J. Phys. Chem. Lett.* **2012**, *3*, 1523–1530.
- Jang, J.-T.; Jeong, S.; Seo, J.-W.; Kim, M.-C.; et al. *J. Am. Chem. Soc.* **2011**, *133*, 7636–7639.
- Shiva, K.; Matte, H. S. S. R.; Reajendra, H. B.; Bhattacharyya, A. J.; Rao, C. N. R. *Nano Energy* **2013**, *2*, 787.
- Mai, L.; Hu, B.; Chen, W.; Qi, Y.; Lao, C.; Yang, R.; Dai, Y.; Wang, Z. L. *Adv. Mater.* **2007**, *19*, 3712–3716.

- (88) Lee, J.-S.; Kim, S. T.; Cao, R.; Choi, N.-S.; Liu, M.; Lee, K. T.; Cho, J. *Adv. Energy Mater.* **2011**, *1*, 34–50.
 (89) Zhu, J.; Yang, D.; Yin, Z.; Yan, Q.; Zhang, H. *Small* **2014**, *10*, 3480–3498.
 (90) Xiao, J.; Mei, D.; Li, X.; Xu, W.; et al. *Nano Lett.* **2011**, *11*, 5071–5078.
 (91) Jung, H.-G.; Jeong, Y. S.; Park, J.-B.; Sun, Y.-K.; Scrosati, B.; Lee, Y. J. *ACS Nano* **2013**, *7*, 3532–3539.
 (92) Wang, G.; Shen, X.; Yao, J.; Park, J. *Carbon* **2009**, *47*, 2049–2053.

- (93) Liu, T.; Leskes, M.; Yu, W.; Moore, A. J.; Zhou, L.; Bayley, P. M.; Kim, G.; Grey, C. P. *Science* **2015**, *350*, 530–533.
 (94) Wang, Y.-X.; Chou, S.-L.; Liu, H.-K.; Dou, S.-X. *Carbon* **2013**, *57*, 202–208.
 (95) Ding, J.; Wang, H.; Li, Z.; Kohandehghan, A.; et al. *ACS Nano* **2013**, *7*, 11004–11015.
 (96) Kwon, Y. H.; Woo, S. W.; Jung, H. R.; Yu, H. K.; et al. *Adv. Mater.* **2012**, *24*, 5192–5197.
 (97) Zhao, X. C.; Hayner, M.; Kung, M. C.; Kung, H. H. *Adv. Energy Mater.* **2011**, *1*, 1079–1084.

Graphene

For a complete list of available materials, visit aldrich.com/graphene.

Graphene and Graphene Nanoplatelets

Name	Form	Composition	Description	Prod. No.
Graphene nanoplatelets	powder	Graphene nanoplates as produced	Anionic Surfactant	799084-500MG
	powder	Carbon > 95 wt. % Oxygen < 2 wt. %	hydrophobic	806668-25G
	powder	Carbon > 85 wt. % Oxygen > 3 wt. %	Dispersibility: dichloromethane, <i>N</i> -methyl-2-pyrrolidone, and other non-polar solvents hydrocarbon functionalized, hydrophobic	806633-25G
	powder	Carbon > 95 wt. % Oxygen > 1 wt. %	Dispersibility: Water, THF, DMF oxidized	806641-25G
	powder	Carbon > 70 wt. % Oxygen > 10 wt. %	Dispersibility: water (high stability in aqueous medium) polycarboxylate functionalized, hydrophilic	806625-25G
	dispersion in H ₂ O, 1 mg/mL	Graphene 0.1% Water 99.9%	Anionic Surfactant	799092-50ML
Graphene dispersion	dispersion in NMP, 10 mg/mL	Graphene 1% NMP 99%	-	803839-5ML

Graphene Nanoribbons

Name	Purity	Dimension (μm × nm)	Surface Area (m ² /g by BET)	Prod. No.
Graphene nanoribbons, alkyl functionalized	≥85% carbon basis, TGA	L × W 2-15 × 40-250	BET surf. area 38 m ² /g	797766-500MG
Graphene nanoribbons	≥90.0% carbon basis, TGA	L × W 2-15 × 40-250	BET surf. area 48-58 m ² /g	797774-500MG

Graphene Inks

Name	Particle Size	Electrical Properties	Viscosity	Prod. No.
Graphene dispersion, with ethyl cellulose in cyclohexanone and terpineol, inkjet printable	≤3 μm	resistivity 0.003-0.008 Ω-cm (thermally annealed 250 °C for 30 minutes, film thickness >100 nm)	8-15 mPa.s at 30 °C	793663-5ML
Graphene dispersion, with ethyl cellulose in terpineol, gravure printable	≤3 μm	resistivity 0.003-0.008 Ω-cm (thermally annealed 250 °C for 30 minutes, film thickness >100 nm)	0.75-3 Pa.s at 25 °C (shear viscosity at 100 s ⁻¹ , 25 °C)	796115-10ML
Graphene dispersion, with ethyl cellulose in terpineol, screen printable	≤3 μm	resistivity 0.003-0.008 Ω-cm (thermally annealed 300 °C for 30 minutes, film thickness >100 nm, 25 °C)	5-50 Pa.s at 25 °C (shear viscosity at 10 s ⁻¹)	798983-10ML
Graphene ink in water, inkjet printable	80 - 500 nm (exfoliated graphene flakes)	sheet resistance 4k Ω/sq (80 nm thickness)	1 cP (100s ⁻¹)	808288-5ML
Graphene ink in water, flexo/gravure/screen printable	500 - 1500 nm (exfoliated graphene flakes)	sheet resistance 10 Ω/sq (25μm thickness)	140 cP (1000s ⁻¹) 570 cP (100s ⁻¹)	805556-10ML
Graphene ink in water, screen printable	500 - 1500 nm (exfoliated graphene flakes)	sheet resistance 10 Ω/sq (at 25 μm thickness)	1800 cP (1000s ⁻¹) 350 cP (100s ⁻¹)	808261-10ML

Graphene Films

Name	Size (L × W × thickness)	Resistance (Ω/sq)	Prod. No.
Monolayer graphene film, on copper foil	1.5 cm × 1.5 cm × 25 μm (copper foil substrate) 1 cm × 1 cm × (theoretical) 0.345 nm (Monolayer graphene film)	600	773697-4EA
	1 in. × 1 in. × 18 μm (copper foil substrate) 1 in. × 1 in. × (theoretical) 0.245 nm (monolayer graphene film)	350	799009-1EA
Monolayer graphene film, on quartz	1.25 cm × 1.25 cm × 525 μm (quartz substrate) 1 cm × 1 cm × (theoretical) 0.345 nm (monolayer graphene film)	600	773719-4EA
Monolayer graphene film, on SiO ₂ /Si substrate	1 cm × 1 cm × (theoretical) 0.345 nm (monolayer graphene film) 1 cm × 1 cm × 525 μm (SiO ₂ /Si substrate)	600	773700-4EA

Name	Size (L x W x thickness)	Resistance (Ω /sq)	Prod. No.
Monolayer graphene film, on PET film	1 in. x 1 in. x 0.188 mm (PET film substrate)	700	745863-1EA 745863-5EA
	1 in. x 1 in. x (theoretical) 0.345 nm (monolayer graphene film)		
	2 in. x 2 in. x (theoretical) 0.345 nm (monolayer graphene film)	700	745871-1EA
	2 in. x 2 in. x 0.188 mm (PET film substrate)		
Suspended monolayer graphene on TEM grid substrate (Quantifoil gold)	diam. x thickness 2 mm x (theoretical) 0.345 nm (monolayer graphene film) size x distance between discs x diam. 2 μ m x 4 μ m x 3 mm (gold coated TEM grid)	170	798177-1PK

Graphene Field Effect Transistor Chips

Name	Description	Prod. No.
Graphene field effect transistor chip	FET mobility on Al_2O_3 : ~3000 cm^2/V sec FET mobility on Si/SiO_2 : ~1500 cm^2/V sec Material uniformity: >95% Single layer graphene Sheet resistance on Si/SiO_2 : 900 \pm 50 ohms/sq Transparency: >97.4%	803995-1EA

Reduced Graphene Oxide

For a complete list of available materials, visit aldrich.com/graphene.

Description	Composition	Conductivity	Prod. No.
chemically reduced	Carbon > 95 wt. % Nitrogen > 5 wt. %	> 600 S/m	777684-250MG 777684-500MG
chemically reduced by hydrazine	Carbon > 75% Nitrogen < 5%	7111 S/m (pressed pallet)	805424-1G
amine functionalized	Carbon > 65 wt. % Nitrogen > 5 wt. %	-	805432-500MG
Form: Black powder octadecylamine functionalized	Carbon > 78 wt. % Nitrogen > 3 wt. %	6.36 S/m (pressed pellets)	805084-500MG
tetraethylene pentamine functionalized	Carbon > 65 wt. % Nitrogen > 8 wt. %	-	806579-500MG
piperazine functionalized	Carbon > 65 wt. % Nitrogen > 5 wt. %	70.75 S/m (pressed pellets)	805440-500MG

Graphene Oxide

For a complete list of available materials, visit aldrich.com/graphene.

Name	Form	Description	Prod. No.
Graphene oxide	dispersion in H_2O	2 mg/mL	763705-25ML 763705-100ML
	dispersion in H_2O	4 mg/mL, dispersibility: Polar solvents monolayer content (measured in 0.5mg/mL): >95%	777676-50ML 777676-200ML
	dispersion in H_2O	1 mg/mL, 15-20 sheets, 4-10% edge-oxidized	794341-50ML 794341-200ML
	powder or flakes	sheets	763713-250MG 763713-1G
	powder	15-20 sheets 4-10% edge-oxidized	796034-1G
	film	4 cm (diameter) x 12-15mm (thickness), non-conductive	798991-1EA
Graphene oxide, ammonia functionalized	dispersion in H_2O	1 mg/mL	791520-25ML 791520-100ML
Graphene oxide, alkylamine functionalized	dispersion (in toluene)	2.0 mg/mL	809055-50ML
Graphene oxide nanocolloids	dispersion in H_2O	2 mg/mL	795534-50ML 795534-200ML

Graphene Nanocomposites

For a complete list of available materials, visit aldrich.com/graphene.

Graphene-based Nanocomposites

Name	Particle Size (nm)	Composition	Prod. No.
Fe ₃ O ₄ /graphene nanocomposite	5 - 25 (Fe ₃ O ₄ nanocrystal)	graphene 3-8% Fe ₃ O ₄ nanocrystal 4-9% acetone ~80 wt.%	803715-5ML
Mn ₃ O ₄ /graphene nanocomposite	5 - 25 (Mn ₃ O ₄ nanocrystal)	graphene 3-8% Mn ₃ O ₄ nanocrystal 4-9% acetone ~80 wt.%	803723-5ML
Pd/graphene nanocomposite	5 - 50 (Pd nanocrystal)	graphene 6-10% Pd nanoparticle 2-6% acetone ~80 wt.%	803707-5ML
Pt/graphene nanocomposite	2 - 5 (Pt nanocrystal)	graphene 6-10% Pt nanoparticle 1-4% acetone ~80 wt.%	803693-5ML
PtCo/graphene nanocomposite	2 - 5 (PtCo nanocrystal)	graphene 10-15% PtCo nanocrystal 5-10% acetone ~80%	803766-5ML
PtPd/graphene nanocomposite	5 - 50 (PtPd nanocrystal)	graphene 10-15% PtPd nanocrystal 5-10% acetone ~80%	803758-5ML

Reduced Graphene Oxide-based Nanocomposites

Name	Particle Size (nm)	Composition	Prod. No.
Fe ₃ O ₄ /reduced graphene oxide nanocomposite	5 - 25 (Fe ₃ O ₄ nanocrystal)	reduced graphene oxide 10-17% Fe ₃ O ₄ nanocrystal 3-8% acetone ~80%	803804-5ML
Mn ₃ O ₄ /reduced graphene oxide nanocomposite	5 - 25 (Mn ₃ O ₄ nanocrystal)	reduced graphene oxide 10-17% Mn ₃ O ₄ nanocrystal <3-8% acetone ~80%	803812-5ML
Pd/reduced graphene oxide nanocomposite	5 - 50 (Pd nanocrystal)	reduced graphene oxide 5-20% Pd nanocrystal <5% acetone ~80%	803790-5ML
Pt/reduced graphene oxide nanocomposite	2 - 5 (Pt nanocrystal)	reduced graphene oxide 5-20% Pt nanocrystal <5% acetone ~80%	803782-5ML
PtCo/reduced graphene oxide nanocomposite	2 - 5 (PtCo nanocrystal)	reduced graphene oxide 10-18% PtCo nanocrystal 2-10% acetone ~80%	803901-5ML
PtPd/reduced graphene oxide nanocomposite	5 - 50 (PtPd nanocrystal)	reduced graphene oxide 10-18% PtPd nanocrystal 2-10% acetone ~80%	803820-5ML

NANOSTRUCTURED OLIVINE-BASED CATHODE MATERIALS FOR LITHIUM-ION BATTERIES



Vishwanathan Ramar and Palani Balaya*
Department of Mechanical Engineering
National University of Singapore, Singapore-117576
*Email: mpepb@nus.edu.sg

Introduction

Due to the adverse impact of the continued use of fossil fuels on the earth's environment and climate, researchers have been asked to develop new approaches for producing power using renewable sources like wind and solar energy.¹ Although renewable energy sources are abundant, they are highly intermittent in nature, which makes advancement in renewable energy difficult without further development of electrical energy storage systems. Lithium-ion batteries (LIBs) have favorable energy and power densities that arise from high electromotive force generated by the high electrochemical reactivity of Li^+ .¹ The physicochemical properties of ionic transport, electron transport, and electrochemical kinetics must be precisely balanced in order to efficiently convert the chemical energy to be stored in batteries.²⁻⁴ We have developed new approaches to more effectively achieve this balance by shifting from micro-sized particles to nano-sized particles and adding conductive wiring to the surface of the nano-sized particles.³

The overall storage properties of LIB depend upon the materials used for cathodes, anodes, and electrolytes.⁵ In this regard, various classes of inorganic cathode materials have been investigated.⁴ We focus on polyanion-based cathode materials for Li storage (i.e., phosphates), emphasizing the role of nanoscale design on electrochemical kinetics and lithium storage performance.

During the electrochemical redox reaction, guest species such as Li^+ are reversibly intercalated and deintercalated into the host lattice of the electrode materials. The specific storage capacities of electrodes are estimated based on the reversible insertion/extraction of Li^+ ions during electrochemical processes. For example, orthorhombic phospho-olivine LiMPO_4 ($M = \text{Fe}, \text{Mn}, \text{Co}, \text{or Ni}$)⁶ cathode materials enable the reversible intercalation/deintercalation of 1 mole of Li per formula unit with a theoretical capacity of 170 mAh g^{-1} . Unlike other oxide-based cathode materials, the phospho-olivine framework is very stable because of its strong P–O covalent bonding which prevents oxygen release.⁷ Intrinsic structural stability makes these materials safe candidates for electric vehicle applications. One of the most widely studied cathode materials, lithium iron(II) phosphate (LFP, **Prod. No. 759546**), exhibits a specific energy of 586 Wh kg^{-1} ($170 \text{ mAh g}^{-1} \times 3.45 \text{ V}$).^{6,8-9} Besides LFP, lithium manganese phosphate (LMP), also offers a high specific energy of

701 Wh kg^{-1} ($171 \text{ mAh g}^{-1} \times 4.1 \text{ V}$) arising from its high $\text{Mn}^{2+}/\text{Mn}^{3+}$ redox voltage ($\sim 4.1 \text{ V}$ vs. Li/Li^+).¹⁰⁻¹⁵ However, the energy density of LMP is limited by its low electronic conductivity, ionic diffusivity,^{7,16} interfacial strain between the $\text{LiMnPO}_4/\text{MnPO}_4$ phases,¹⁷ and Jahn-Teller distortion.¹⁸

Our scalable synthetic approach for the production of nanostructured LiMPO_4 ($M = \text{Fe}$ and/or Mn) as well as the electrochemical properties of the nanostructured LMP cathode material is presented here. Phosphate-based cathode materials synthesized by the soft template-method assisted high energy ball milling method with carbon black attain reduced particle size and enhanced carbon wiring formation as described in our earlier reports.¹³⁻¹⁴ A nanostructure with divalent cation substitution can further enhance the lithium storage properties, making it a prospective candidate for practical applications.

Synthesis of Nanostructured Phosphate-based Cathode Materials

We dissolved 0.01 M of the cationic surfactant hexadecyltrimethylammonium bromide (**Prod. No. H5882**) in a mixture of absolute ethanol and milli-Q/DI water in a V/V ratio of 5:1 to form micelles. Following this, manganese(II) acetate tetrahydrate (**Prod. No. 221007**) and/or iron(III) acetate (**Prod. No. 517933**) and lithium dihydrogen phosphate (**Prod. No. 442682**) were added in stoichiometric ratio and stirred for 24 h. The solvents were evaporated using a Heidolph Hei-VAP rotary evaporator. The final product was calcined in a furnace at $650 \text{ }^\circ\text{C}$ for 6 h in an Ar-H_2 (95:5) gas environment. Pure LiMPO_4 ($M = \text{Fe}$ and/or Mn) materials were milled together with carbon black using a FRITSCHE premium line high energy ball mill at 500 rpm for 4 h.¹³⁻¹⁴ Further mild heat treatment was carried out at $500 \text{ }^\circ\text{C}$ for 3 h in an Ar-H_2 atmosphere to relieve any stress developed during the ball mill process.

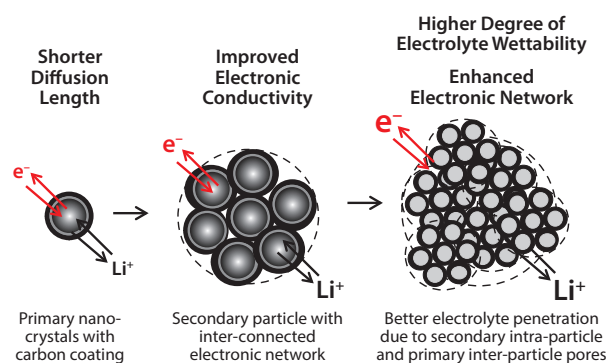


Figure 1. Schematic of nanostructuring strategies to improve the electrochemical properties of inorganic electrode materials.

Figure 1 represents nanostructuring strategies used to enhance the lithium storage performance of LiMPO_4 ($M = \text{Fe}$ and/or Mn). The particles are comprised of interconnected nano-crystals and mesopores with

a conductive carbon coating. These particles were prepared using the soft template assisted high energy ball mill method. This material architecture offers the advantages of short transport length, improved electronic conductivity, and improved electronic network due to interconnectivity of primary (particle–particle) and secondary particles. The material also includes pores that provide penetration of the organic electrolyte, facilitating rapid insertion/extraction of lithium ions in the electrode materials.

Electrochemical Properties of Nanostructured LiMnPO_4 Cathode Materials

Figure 2A presents the X-ray diffraction (XRD) patterns of micron-sized and nano-sized LMP samples. All the Bragg peaks were indexed to the *Pmnb* space group (JCPDS Card No. 33-0803) with an olivine structure. The expanded XRD 2θ region (**Figure 2B**) shows that peak broadening increases as particle size decreases. No significant changes were observed in the lattice parameters. Transmission electron microscope (TEM) images of micron-sized (M-LMP) and nano-sized LMP/C (N-LMP/C) samples are displayed in **Figures 2C** and **2D**, respectively. The M-LMP particle size is ~ 400 nm, while N-LMP/C has a particle size of 40–50 nm. Notably, the surface area of N-LMP/C sample is higher (~ 46 $\text{m}^2 \text{g}^{-1}$) than the M-LMP sample (~ 9.9 $\text{m}^2 \text{g}^{-1}$).

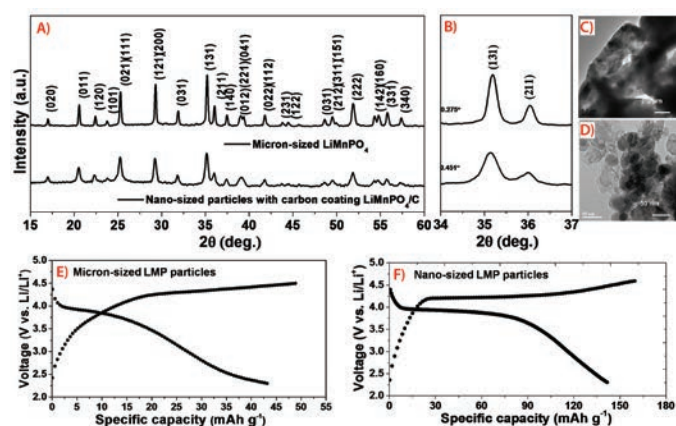


Figure 2. A) XRD patterns (JCPDS Card No. 33-0803) for micron-sized LiMnPO_4 and nano-sized LiMnPO_4/C samples. B) Expanded 2θ region illustrating the peak broadening. C) TEM image of micron-sized LMP. D) TEM image of nano-sized LMP; charge-discharge profile of E) micron- and F) nano-LMP/C at 0.05 C.

The storage performance was then evaluated using the galvanostatic cycling process. The corresponding voltage–specific capacity profile for micron- and nano-LMP samples are presented in **Figures 2E** and **2F**. The charge-discharge plateaus of the M-LMP sample corresponding to $\text{Mn}^{2+}/\text{Mn}^{3+}$ redox potentials are seen at ~ 4.31 V and 3.95 V vs. Li/Li^+ (**Figure 2E**) while the redox potentials of the nano-sized LMP/C sample occurs at ~ 4.27 V and 3.97 V vs. Li/Li^+ (**Figure 2F**). A better extraction/insertion plateau of lithium ions is observed for the N-LMP/C sample with a higher discharge capacity of 140 mAh g^{-1} compared to the M-LMP sample which exhibits only 43 mAh g^{-1} at 0.05 C over the voltage window of 4.6–2.3 V at room temperature. This improved electrochemical property of N-LMP/C is ascribed to nanoparticles with a higher surface area and carbon coating.

Electrochemical Properties of Nanostructured $\text{LiFe}_x\text{Mn}_{1-x}\text{PO}_4/\text{C}$ ($x = 0.2, 0.5, \text{ and } 0.8$) Cathode Materials

Nanostructuring of the LMP particle along with carbon coating improved the electrochemical performance. However, we observed that complete extraction and insertion of lithium is not possible in N-LMP. Therefore, to further improve the electrochemical performance of N-LMP/C, the Fe^{2+} cation was substituted for Mn^{2+} . The Fe^{2+} -substituted $\text{LiFe}_x\text{Mn}_{1-x}\text{PO}_4/\text{C}$ ($x = 0.2, 0.5, \text{ and } 0.8$) samples were prepared using the high energy ball mill-assisted soft template method as described earlier. **Figure 3A** shows the XRD of the $\text{LiFe}_x\text{Mn}_{1-x}\text{PO}_4/\text{C}$ ($x = 0.2, 0.5, \text{ and } 0.8$) samples. All the Bragg peaks belong to the *Pmnb* space group (JCPDS Card No. 33-0803). The expanded 2θ region as presented in **Figure 3B** indicates a continuous shift in the peak positions, revealing formation of Mn-Fe mixed compositions. Field Emission Scanning Electron Microscope (FESEM) images of $\text{LiFe}_x\text{Mn}_{1-x}\text{PO}_4/\text{C}$ ($x = 0.2, 0.5, \text{ and } 0.8$) samples show the presence of particles with a pseudo-spherical morphology (**Figure 4**) with nanocrystals of 40–50 nm. Notably, all the samples exhibit similar surface area and pore sizes.

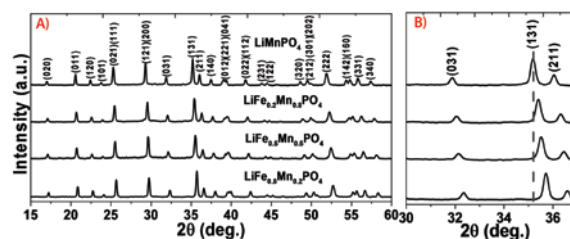


Figure 3. A) XRD patterns of the $\text{LiFe}_x\text{Mn}_{1-x}\text{PO}_4/\text{C}$ ($x = 0.2, 0.5, \text{ and } 0.8$) samples and XRD pattern of LiMnPO_4 sample for comparison. B) Expanded 2θ region showing the continuous shift in the peak positions to the higher angles with the substitution of the Fe^{2+} for Mn^{2+} .

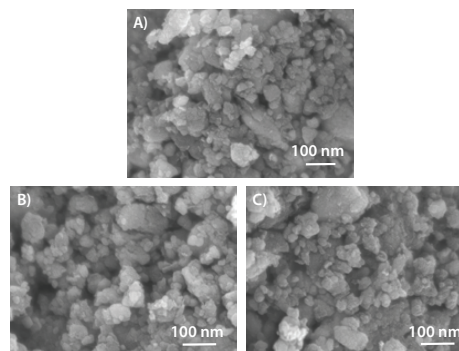


Figure 4. FESEM images of A) $\text{LiFe}_{0.2}\text{Mn}_{0.8}\text{PO}_4/\text{C}$, B) $\text{LiFe}_{0.5}\text{Mn}_{0.5}\text{PO}_4/\text{C}$, and C) $\text{LiFe}_{0.8}\text{Mn}_{0.2}\text{PO}_4/\text{C}$.

Figures 5A, 5C, and 5E illustrate the galvanostatic profiles of $\text{LiMn}_{1-x}\text{Fe}_x\text{PO}_4$ ($x = 0.2, 0.5, \text{ and } 0.8$) in which two distinct charge-discharge plateaus corresponding to $\text{Mn}^{2+}/\text{Mn}^{3+}$ and $\text{Fe}^{2+}/\text{Fe}^{3+}$ redox couples can be seen. All of the Mn-Fe mixed compositions exhibit a similar discharge capacity of 159 mAh g^{-1} at 0.1 C (close to the theoretical capacity of 170 mAh g^{-1}) compared to nanostructured LiMnPO_4 which delivers a capacity of 140 mAh g^{-1} at 0.05 C. Unlike LiMnPO_4 , the resultant capacity is an

oxidation/reduction contribution of both $\text{Fe}^{2+}/\text{Fe}^{3+}$ (~3.45 V) and $\text{Mn}^{2+}/\text{Mn}^{3+}$ (~4.1 V). Although the capacity is similar for all of the compositions, $\text{LiFe}_{0.2}\text{Mn}_{0.8}\text{PO}_4/\text{C}$ exhibits high energy density since 80% of the lithium storage capacity occurs at the higher potential Mn regime. The voltage polarization of mixed transition compositions is much lower than the parent LiMnPO_4 .¹³ The huge reduction in polarization at the Mn redox region and improved storage performance can be ascribed to nanostructuring, carbon coating, Fe-O-Mn superexchange interaction, lower activation energy, and the electronic configuration of Mn^{2+} ($3d^5$) and Fe^{2+} ($3d^6$) of Mn-Fe mixed olivines.

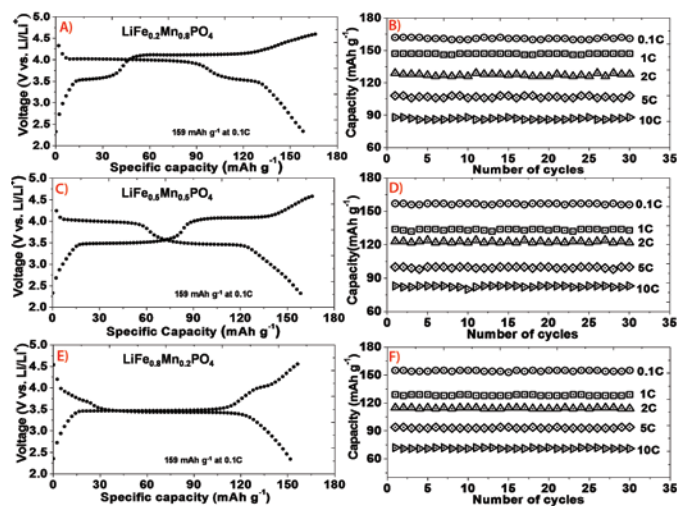


Figure 5. Galvanostatic charge/discharge profiles of $\text{LiFe}_x\text{Mn}_{1-x}\text{PO}_4/\text{C}$ ($x = 0.2, 0.5, \text{ and } 0.8$) at 0.1 C and corresponding cycling stability up to 30 cycles at various C-rates: A,B) $\text{LiFe}_{0.2}\text{Mn}_{0.8}\text{PO}_4/\text{C}$; C,D) $\text{LiFe}_{0.5}\text{Mn}_{0.5}\text{PO}_4/\text{C}$; and E,F) $\text{LiFe}_{0.8}\text{Mn}_{0.2}\text{PO}_4/\text{C}$, in a voltage window of 4.6–2.3 V at room temperature.

The stabilized discharge capacity of $\text{LiFe}_x\text{Mn}_{1-x}\text{PO}_4/\text{C}$ ($x = 0.2, 0.5, \text{ and } 0.8$) at various C-rates (0.1, 1, 2, 5, and 10 C) are shown in **Figures 5B, 5D, and 5F**. The $\text{LiFe}_{0.2}\text{Mn}_{0.8}\text{PO}_4/\text{C}$ electrode delivers discharge capacities of 159, 141, 125, 106, and 88 mAh g^{-1} at 0.1, 1, 2, 5, and 10 C, respectively (**Figure 5B**). Similarly, the $\text{LiFe}_{0.5}\text{Mn}_{0.5}\text{PO}_4/\text{C}$ electrode exhibits discharge capacities of 159, 134, 122, 100, and 82 mAh g^{-1} at 0.1, 1, 2, 5, and 10 C, respectively (**Figure 5D**). $\text{LiFe}_{0.8}\text{Mn}_{0.2}\text{PO}_4/\text{C}$ electrode shows discharge capacities of 159, 126, 115, 93, and 70 mAh g^{-1} at 0.1, 1, 2, 5, and 10 C, respectively (**Figure 5F**). Nanostructured Mn-Fe mixed olivine samples showed good cyclic stability compared to nanostructured LMP/C of up to 30 cycles.¹³

Electrode Sheets

For a complete list of available materials, visit aldrich.com/lib.

Sheet size 5 × 10 in./80% active material on aluminum electrode substrate.

Name	Composition	Purity	Nominal Voltage (V)	Capacity (minimum)	Capacity (nominal)	Prod. No.
Lithium manganese nickel oxide, LMNO	$\text{Li}_x\text{Mn}_y\text{NiO}_z$	≥98%	4.7 (Li/Li ⁺)	115 mAh/g	125 mAh/g	765198-1EA
Lithium manganese oxide, LMO	LiMn_2O_4	≥98%	4.7 (Li/Li ⁺)	110 mAh/g	120 mAh/g	765201-1EA
Lithium nickel cobalt aluminium oxide, NCA	$\text{LiNi}_{0.8}\text{Co}_{0.15}\text{Al}_{0.05}\text{O}_2$	≥98%	3.7 (Li/Li ⁺)	150 mAh/g	180 mAh/g	765171-1EA
Lithium nickel manganese cobalt oxide, NMC	$\text{LiNi}_{0.33}\text{Mn}_{0.33}\text{Co}_{0.33}\text{O}_2$	-	3.5 (Li/Li ⁺)	210 mAh/g	-	765163-1EA
Lithium titanate, LTO	$\text{Li}_4\text{Ti}_5\text{O}_{12}$	≥98%	1.5 (Li/Li ⁺)	160 mAh/g	150 mAh/g	765155-1EA

Summary

Favorable physicochemical balancing can be achieved by nano-sizing and introducing conductive carbon wiring on the surface of nanomaterials. Nano-sized LMP/C exhibits superior storage performance of 140 mAh g^{-1} compared to a micron-sized LMP sample capable of only 43 mAh g^{-1} at 0.05 C. Use of the nanostructuring strategy with Fe^{2+} cation substitution at the Mn site enhances the electrochemical properties of the electrodes, resulting in improved energy storage capacity compared to nano-LMP/C. This makes them attractive as electrode materials for LIBs. Accordingly, nanostructured $\text{LiFe}_x\text{Mn}_{1-x}\text{PO}_4/\text{C}$ ($x = 0.2, 0.5, \text{ and } 0.8$) compounds deliver a discharge capacity of ~159 mAh g^{-1} at 0.1 C.

Acknowledgments

Authors thank DSO, Singapore for their funding support (WBS: R-265-000-393-592).

References

- (1) Tarascon, J. M.; Armand, M. *Nature*. **2001**, *414*, 359–367.
- (2) Maier, J. *Nat. Mater.* **2005**, *4*, 805–815.
- (3) Balaya, P. *Energy Environ. Sci.* **2008**, *1*, 645–654.
- (4) Arico, A. S.; Bruce, P.; Scrosati, B.; Tarascon, J.-M.; van Schalkwijk, W. *Nat. Mater.* **2005**, *4*, 366–377.
- (5) Goodenough, J. B.; Kim, Y. *Chem. Mater.* **2009**, *22*, 587–603.
- (6) Padhi, A. K.; Nanjundaswamy, K. S.; Goodenough, J. B. *J. Electrochem. Soc.* **1997**, *144*, 1188–1194.
- (7) Yonemura, M.; Yamada, A.; Takei, Y.; Sonoyama, N.; Kanno, R. *J. Electrochem. Soc.* **2004**, *151*, A1352–A1356.
- (8) Saravanan, K.; Reddy, M. V.; Balaya, P.; Gong, H.; Chowdari, B. V. R.; Vittal, J. J. *Mater. Chem.* **2009**, *19*, 605–610.
- (9) Padhi, A. K.; Nanjundaswamy, K. S.; Masquelier, C.; Okada, S.; Goodenough, J. B. *J. Electrochem. Soc.* **1997**, *144*, 1609–1613.
- (10) Yamada, A.; Kudo, Y.; Liu, K.-Y. *J. Electrochem. Soc.* **2001**, *148*, A747–A754.
- (11) Wang, D.; Deghenghi, G.; Exnar, I. *J. Electrochem. Soc.* **2009**, *156*, A541–A552.
- (12) Drezen, T.; Kwon, N.-H.; Bowen, P.; Teerlinck, I.; Isono, M.; Exnar, I. *J. of Power Sources*. **2007**, *174*, 949–953.
- (13) Marthas, S. K.; Markovsky, B.; Grinblat, J.; Gofer, Y.; Haik, O.; Zinigrad, E.; Aurbach, D.; Drezen, T.; Wang, D.; Deghenghi, G.; Exnar, I. *J. Electrochem. Soc.* **2009**, *156*, A541–A552.
- (14) Ramar, V.; Saravanan, K.; Gajjala, S. R.; Hariharan, S.; Balaya, P. *Electrochim. Acta*. **2013**, *105*, 496–505.
- (15) Ramar, V.; Balaya, P. *Phys. Chem. Chem. Phys.* **2013**, *15*, 17240–17249.
- (16) Saravanan, K.; Ramar, V.; Balaya, P.; Vittal, J. J. *Mater. Chem.* **2011**, *21*, 14925–14935.
- (17) Rissouli, K.; Benkhouja, K.; Ramos-Barrado, J. R.; Julien, C. *Mater. Sci. Eng. B*. **2003**, *98*, 185–189.
- (18) Meethong, N.; Huang, H. Y. S.; Speakman, S. A.; Carter, W. C.; Chiang, Y. M. *Adv. Funct. Mater.* **2007**, *17*, 1115–1123.
- (19) Yamada, A.; Yonemura, M.; Takei, Y.; Sonoyama, N.; Kanno, R. *Electrochem. Solid State Lett.* **2005**, *8*, A55–A58.

Cathode Materials

For a complete list of available materials, visit aldrich.com/lib.

Name	Composition	Purity	Particle Size	Prod. No.
Cobalt monoantimonide	CoSb	99.9% trace metals basis	-80 mesh	746320-5G
Lithium cobalt(III) oxide	LiCoO ₂	powder, 99.8% trace metals basis	-	442704-100G-A
Lithium cobalt phosphate, LCP	LiCoPO ₄	powder, 99%	-	725145-25G
Lithium cobalt phosphate, LCP	LiCoPO ₄	powder, 99.9% trace metals basis	-	777110-25G
Lithium iron(III) oxide	LiFeO ₂	powder, 95%	<1 μm	442712-100G-A
Lithium iron(II) phosphate, LFP	LiFePO ₄	powder, >97% (XRF)	<5 μm (BET)	759546-5G
Lithium manganese dioxide	LiMnO ₂	powder, >99% trace metals basis	<1 μm	725137-25G
Lithium manganese nickel oxide, LMNO	Li ₂ Mn ₃ NiO ₈	powder, >99%	<0.5 μm (BET)	725110-25G
Lithium manganese oxide, LMO	LiMn ₂ O ₄	powder, >99%	<0.5 μm (BET)	725129-25G
Lithium manganese(III,IV) oxide, LMO	LiMn ₂ O ₄	-	<5 μm	482277-25G
Lithium molybdate	Li ₂ MoO ₄	powder or crystals, 99.9% trace metals basis	-	400904-250G
Lithium nickel cobalt aluminium oxide, NCA	LiNi _{0.8} Co _{0.15} Al _{0.05} O ₂	powder, >98%	<0.5 μm	760994-10G
Lithium nickel cobalt oxide, LNCO	LiNi _{0.8} Co _{0.2} O ₂	powder, >98%	<0.5 μm	760986-10G
Lithium nickel dioxide, LNO	LiNiO ₂	powder, ≥98% trace metals basis	<3 μm (BET)	757365-10G
Lithium nickel manganese cobalt oxide, NMC	LiNi _{0.33} Mn _{0.33} Co _{0.33} O ₂	powder, >98%	<0.5 μm	761001-10G
Manganese nickel carbonate	Mn _{0.75} Ni _{0.25} CO ₃	powder, 99.99% trace metals basis (excluding Mg)	-	763608-25G

Anode Materials

For a complete list of available materials, visit aldrich.com/lib.

Name	Purity	Description	Form	Prod. No.
Lithium	99%, metals basis	particle size 4-10 mesh	granular	444456-10G 444456-50G
	99.9% trace metals basis	thickness × W 1.5 × 100 mm	ribbon	266000-25G 266000-100G
	99.9% trace metals basis	thickness × W 0.75 × 45 mm	ribbon	265993-25G 265993-100G
	99.9% trace metals basis	thickness × W 0.75 × 19 mm	ribbon	320080-25G 320080-100G
	99.9% trace metals basis	thickness × W 0.38 × 23 mm	ribbon	265985-25G 265985-100G
	≥98%	diam. 3.2 mm	wire	278327-25G 278327-100G
Lithium-aluminum alloy	-	-	powder	426490-25G
Lithium titanate, LTO	-	-325 mesh	powder	400939-100G
Lithium titanate, spinel, LTO nanopowder	>99%	particle size <200 nm (BET)	nanopowder	702277-25G
Tin(IV) oxide	-	particle size <100 nm (BET)	nanopowder	549657-5G 549657-25G

Electrolyte Solutions

For a complete list of available materials, visit aldrich.com/lib.

Lithium Hexafluorophosphate Solutions, Battery Grade: H₂O <15 ppm; HF <50 ppm; APHA <50

Name	Specifications	Prod. No.
2.0 M LiPF ₆ in EC/DMC= 50/50(v/v)	in ethylene carbonate and dimethyl carbonate	809357-100ML
2.0 M LiPF ₆ EC/EMC=50/50(v/v)	in ethylene carbonate and ethylmethyl carbonate	809365-100ML
2.0 M LiPF ₆ EC/DEC= 50/50(v/v)	in ethylene carbonate and diethyl carbonate	809349-100ML
2.0 M LiPF ₆ DMC	in dimethyl carbonate	809411-100ML
2.0 M LiPF ₆ EMC	in ethylmethyl carbonate	809403-100ML
2.0M LiPF ₆ DEC	in diethyl carbonate	809543-100ML
2.0 M LiPF ₆ PC	in propylene carbonate	809470-100ML
1.0 M LiPF ₆ in EC/DMC=50/50 (v/v)	in ethylene carbonate and dimethyl carbonate	746711-100ML
1.0 M LiPF ₆ in EC/EMC=50/50 (v/v)	in ethylene carbonate and ethyl methyl carbonate	746738-100ML
1.0 M LiPF ₆ in EC/DEC=50/50 (v/v)	in ethylene carbonate and diethyl carbonate	746746-100ML

Name	Specifications	Prod. No.
1.0 M LiPF ₆ in DMC	in dimethyl carbonate	746754-100ML
1.0 M LiPF ₆ in EMC	in ethyl methyl carbonate	746762-100ML
1.0 M LiPF ₆ in DEC	in diethyl carbonate	746770-100ML
1.0 M LiPF ₆ in PC	in propylene carbonate	746789-100ML

Electrolyte Materials

For a complete list of available materials, visit aldrich.com/lib.

Name	Composition	Purity	Prod. No.
Lithium bis(oxalato)borate	LiB(C ₂ O ₄) ₂	-	757136-25G
Lithium difluoro(oxalato)borate	LiBF ₂ (C ₂ O ₄)	-	774138-25G
Lithium hexafluoroarsenate(V)	LiAsF ₆	98%	308315-10G
Lithium hexafluorophosphate	LiPF ₆	≥99.99% trace metals basis	450227-5G 450227-25G 450227-250G
Lithium perchlorate	LiClO ₄	99.99% trace metals basis	634565-10G 634565-100G
Lithium phosphate monobasic	LiH ₂ PO ₄	99%	442682-500G-A
Lithium tetrachloroaluminate	LiAlCl ₄	99.99% trace metals basis	451142-5G
Lithium tetrachlorogallate	LiGaCl ₄	99.99% trace metals basis	736317-5G
Lithium tetrafluoroborate	LiBF ₄	99.99% trace metals basis	451622-5G 451622-25G
Lithium trifluoromethanesulfonate	CF ₃ SO ₃ Li	99.995% trace metals basis	481548-5G 481548-25G

Solvents and Additives

For a complete list of available materials, visit aldrich.com/lib.

Name	Structure	Purity	Prod. No.
Acetonitrile, electronic grade	CH ₃ CN	99.999% trace metals basis	733466-1L 733466-4L
Adiponitrile, H ₂ O <100 ppm, acid <200 ppm		>99%	900020-25G
Allyl methyl sulfone		96%	718203-5G
Bis(trifluoromethane)sulfonimide		-	449504-10G 449504-50G
1-Butyl-3-methylimidazolium thiocyanate		≥95%	724408-5G
Diethyl carbonate, anhydrous		≥99%	517135-100ML 517135-1L
Diethyl carbonate, H ₂ O <10 ppm, acid <10ppm		>99%	900018-25G
Diethyl sulfite		98%	774278-25G
Dimethyl carbonate, anhydrous		≥99%	517127-100ML 517127-1L 517127-2L 517127-20L
Dimethyl carbonate, Acid content <10 ppm, H ₂ O <10 ppm		99.99%, GC	809942-25G
1,2-Dimethyl-3-propylimidazolium bis(trifluoromethylsulfonyl)imide		99.9% trace metals basis	724416-1G
Ethylene carbonate, H ₂ O <10 ppm, acid <10 ppm		>99%	809950-25G

Solvents and Additives (cont'd)

Name	Structure	Purity	Prod. No.
Ethylene sulfite		≥99.0%	774251-25G
Ethyl methyl carbonate		99%	754935-50ML
Ethyl methyl carbonate, H ₂ O <10 ppm, acid <10 ppm		99.99%, GC	809934-25G
1-Ethyl-3-methylimidazolium tetrachloroaluminate		99.9% trace metals basis	724424-5G
Ethyl methyl sulfone		97%	709980-5G
Fluoroethylene carbonate		99%	757349-25G
3-(Methylsulfonyl)-1-propyne		95%	718319-5G
Methyl-trioctylammonium bis(trifluoromethylsulfonyl)imide		99.9% trace metals basis	724432-1G
Phenylcyclohexane, H ₂ O <100 ppm, acid <200 ppm		99%	810002-25G
1,3-Propanesultone, H ₂ O <100 ppm, acid		99%	809985-25G
Propylene carbonate, anhydrous		99.7%	310328-100ML 310328-500ML 310328-1L 310328-2L
Propylene carbonate, H ₂ O <10 ppm, acid <10 ppm		>99%	809969-25G
1,2-Propyleneglycol sulfite		≥98%	774456-10G
Propylene sulfate		≥99%	774294-10G
1,3-Propylene sulfite		99%	774243-25G
2-Propynyl methanesulfonate, H ₂ O <100 ppm, acid <200 ppm		>99%	809993-25G
Vinylene carbonate		99%	757144-25G
Vinylene carbonate, H ₂ O <100 ppm, acid <200 ppm		99%	809977-25G

AGGREGATION-INDUCED EMISSION LUMINOGENS FOR NON-DOPED ORGANIC LIGHT-EMITTING DIODES



Han Nie,¹ Zujin Zhao^{1a} and Ben Zhong Tang^{1,2,3b}

¹State Key Laboratory of Luminescent Materials and Devices, South China University of Technology, Guangzhou 510640, China

²Department of Chemistry, The Hong Kong University of Science and Technology, Clear Water Bay, Kowloon, Hong Kong, China

³Hong Kong Branch of Chinese National Engineering Research Center for Tissue Restoration and Reconstruction, Hong Kong, China

^aEmail: mszjzhao@scut.edu.cn

^bEmail: tangbenz@ust.hk

Introduction

Organic Light-emitting Diodes (OLEDs) are solid-state devices that transform electrical energy into light. OLEDs are considered the next generation technology for high-resolution flexible displays and solid state lighting, attracting intense scientific and industrial interest.¹ As the fluorescent OLEDs, which are the first generation of OLEDs and employ conventional fluorophores as emitters, have been significantly studied due to the excellent stability and relatively long operating lifetime of the resulting devices.²

The external quantum efficiency of an OLED (η_{ext}) can be determined by calculating the product of the internal quantum efficiency (η_{int}) and the light out-coupling factor (η_{out}):

$$\eta_{\text{ext}} = \eta_{\text{int}} \times \eta_{\text{out}}$$

Typically, η_{out} is approximately 20–30% for most OLED devices without an optical out-coupling layer. The η_{int} value can be obtained from the equation, $\eta_{\text{int}} = \gamma \times \beta \times \Phi_{\text{PL}}$, where γ is the carrier balance ratio of holes and electrons, β is the fraction of excitons that are capable of radiative decay, and Φ_{PL} is the intrinsic photoluminescence (PL) quantum yield of the emitting layer.³ According to spin statistics, 25% of the excitons generated by electronic excitation are singlet excitons that decay to ground state via fluorescence. Therefore, the β for fluorescent OLEDs is limited to 25% and the theoretical maximum η_{ext} of the device is about 5–7.5% even if the γ and Φ_{PL} of a fluorophore (Φ_{p}) are 100%.³ Thus development of efficient and stable fluorescent materials with high Φ_{p} values is of great importance. Many conventional fluorophores emit strongly as isolated molecules in solutions; however, these emissions experience partial or complete quenching in the aggregated state. This effect is known as aggregation-caused quenching (ACQ).⁴ The ACQ effect is believed to be controlled by the formation of delocalized excitons via strong intermolecular π - π stacking interactions, resulting in red-shifted emissions and low Φ_{PL} values.⁴ Because of the negative impact on Φ_{PL} , the ACQ effect has obstructed the application of conventional fluorophores in OLEDs for some time.

Aggregation-induced emission (AIE) is a unique chromophore aggregation-associated phenomenon that is essentially the opposite of ACQ.⁵ Luminogens with AIE characteristics (AIEgens) are weakly fluorescent or nonfluorescent when molecularly dispersed in dilute solutions, but they fluoresce strongly upon the formation of aggregates.

Figure 1 presents the AIE phenomenon based on a typical AIEgen, 1,1,2,3,4,5-hexaphenylsilole (HPS, **Prod. No. 797294**),⁶ in which the emission of HPS activates upon aggregation.

During the past decade, the AIE phenomenon has been thoroughly characterized through systematic experimental measurements and theoretical calculations. These studies have established that the restriction of intramolecular motion, RIM (comprised of both restriction of intramolecular rotations, RIR, and restriction of intramolecular vibrations, RIV) is largely responsible for the AIE effect.⁶ In the solution state, active molecular motions act as a nonradiative channel for energetic decay from the excited state to the ground state. In the aggregated state, however, these motions are restricted greatly by the spatial constraints and interactions of the surrounding molecules, blocking the nonradiative decay channels and resulting in emission.

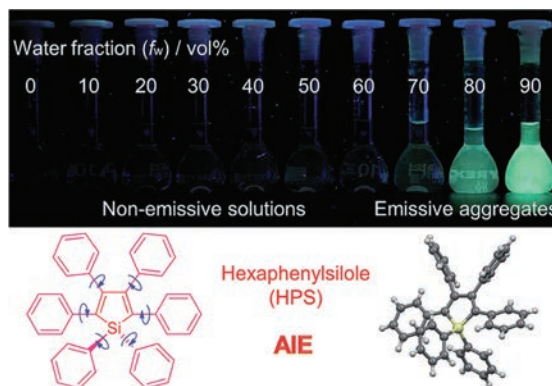


Figure 1. Fluorescence photographs of solutions and suspensions of hexaphenylsilole (HPS; 20 mM) in THF/water mixtures with different fractions of water. Reproduced with permission from Reference 6. Copyright (2014) Wiley-VCH.

Attracted by the potential applications of the AIE phenomenon, many research groups have focused on the development of new AIEgens and how best to harness their potential. A thorough understanding of the AIE mechanism has enabled the development of a wide range of new AIEgens, providing researchers with an alternative strategy for addressing problems caused by fluorescence quenching and enabling the development of new highly efficient solid-state emitters.⁷ Fluorescent AIEgens with high Φ_{E} values in solid films, in particular silole⁸ and tetraphenylethene (TPE)⁹ derivatives, have been widely used to fabricate stable and simplified non-doped fluorescent OLEDs. Some of these OLEDs show excellent electroluminescence (EL) performance with high efficiencies approaching or reaching the theoretical limit. These achievements are summarized in this review.

Silole-based AIEgens

The first reported AIEgens,⁵ propeller-shaped siloles (**Prod. Nos. 797294** and **797286**) have generated the most attention from researchers in the field of organic electronics research. Due to their AIE characteristics, most siloles present high solid-state Φ_f values. Their unique $\sigma^*-\pi^*$ conjugation results in low-lying LUMO (lowest unoccupied molecular orbital) levels, which arise from the interaction between the σ^* orbital of two exocyclic single C–Si bonds and the π^* orbital of the butadiene moiety. As a result, siloles exhibit good electron affinity and fast electron mobility, allowing them to be used to transport electrons in OLEDs.⁸ In addition, siloles display high thermal and morphological stability and good solubility in common solvents, facilitating film fabrication by vapor deposition or using solution processing techniques.⁸ The excellent integrated performance of siloles is a good indicator of their potential for use in the fabrication of non-doped OLEDs, and many efficient solid-state luminescent materials for OLEDs have been developed recently through efforts to engineer new types of siloles.

Fluorene-based substituents have been widely used in the construction of efficient light emitters for OLEDs because of their intense emissivity and good thermal stability. Siloles incorporating dimethylfluorene as substituents at the 2,5-positions of the silole ring show excellent PL and EL properties.¹⁰ For example, the MFMPs film (ITO/NPB (60 nm)/emitter (20 nm)/TPBi (40 nm)/LiF (1 nm)/Al (100 nm)) shown in **Figure 2** exhibits a strong fluorescence peak at 534 nm with a much higher Φ_f value (88%) than that in THF solution (2.6%), indicating AIE characteristics. When MFMPs is adopted as a light-emitting layer to fabricate non-doped OLEDs, e.g., MFMPs [ITO/NPB (60 nm)/MFMPs (20 nm)/TPBi (40 nm)/LiF (1 nm)/Al (100 nm)], the resulting device can be turned on at a low voltage (3.2 V) and radiates yellow light at 544 nm with CIE coordinates ($x = 0.37$, $y = 0.57$), a maximum luminance (L_{\max}) of 31,900 cd m⁻². The device gives good EL efficiencies with a maximum current efficiency ($\eta_{c,\max}$) of 16.0 cd A⁻¹, a maximum power efficiency ($\eta_{p,\max}$) of 13.5 lm W⁻¹, and a maximum external quantum efficiency ($\eta_{\text{ext},\max}$) of 4.8%. This approaches the theoretical limit of OLEDs based on traditional fluorescent materials. The EL performance of MFMPs is further demonstrated in a device configuration that includes ITO/MoO₃ (5 nm)/NPB (60 nm)/MFMPs (20 nm)/TPBi (60 nm)/LiF (1 nm)/Al (100 nm). In this configuration, the device shows a turn-on voltage (V_{on}) of 3.3 V, a yellow EL peak at 540 nm (CIE 0.36, 0.57), and outstanding maximum luminance, current, and power efficiencies of 37,800 cd m⁻², 18.3 cd A⁻¹ and 15.7 lm W⁻¹, respectively. Notably, a $\eta_{\text{ext},\max}$ of 5.5% is obtained in this optimized device, exceptional for fluorescent OLEDs.

As previously discussed, both the outstanding AIE attributes and the unique electronic structures of siloles make them ideal materials for utilization as light-emitting materials and electron transporters in efficient non-doped OLEDs. By combining the two merits of siloles, efficient bifunctional n-type light emitters can also be produced, an approach that is favored for fabricating simplified OLEDs. (MesB)₂MPPS and (MesB)₂HPS are both good examples of this approach. Both contain the silole ring and dimesitylboryl, a functional group that contains inherently electron-deficient groups.¹¹ The tetraphenylsilole moiety endows the luminogens with AIE characteristics and efficient solid-state emissions, while the dimesitylboryl group effectively lowers the LUMO energy level and improves the electron-transporting ability of the molecule by virtue of the vacant low-lying pπ orbital on the boron center. (MesB)₂MPPS and (MesB)₂HPS possess low-lying LUMO energy levels of 3.06 and 3.10 eV, respectively, indicating significant potential as an electron transporter for OLEDs. Solid films of (MesB)₂MPPS and (MesB)₂HPS are highly emissive with peaks at 524 and 526 nm, and exhibit high Φ_f values of 58% and 62%, respectively. Based on these properties, double-layer OLEDs [ITO/NPB (60 nm)/silole (60 nm)/LiF (1 nm)/Al (100 nm)] were fabricated by adopting (MesB)₂MPPS or (MesB)₂HPS simultaneously as both light-emitting (emissive layer, EML) and electron-transporting layers (ETL). These two simplified OLEDs display excellent performance with high $\eta_{c,\max}$ (up to 4.35%), $\eta_{p,\max}$ (up to 13.9 cd A⁻¹), and $\eta_{\text{ext},\max}$ (up to 11.6 lm W⁻¹). All of these results are much higher than those attained using triple-layer devices with an additional TPBi (**Prod. No. 806781**) electron-transporting layer. The excellent performance of these OLEDs is attributed to the efficient electron transport and the LUMO level of siloles matching the cathode work function, resulting in a good carrier balance of holes and electrons (γ). This shows that dimesitylboryl functionalized siloles are efficient n-type solid-state light emitters and are promising bifunctional materials for constructing high-performance and simplified OLEDs. A similar silole derivative, (MesBF)₂MPPS, developed by integrating dimesitylboryl substituents into MFMPs,¹² also exhibits excellent solid-state emission ($\Phi_f = 88\%$) and great electron-transporting potential, consequently presenting a good EL property as well (**Table 1**).

TPE-based AIEgens

The TPE functionality is one of the most popular AIEgen moieties because of its simple molecular structure and remarkable AIE effect. A TPE unit can easily be introduced into ACQ fluorophores to create new fluorescent AIEgens with high emission efficiencies in the aggregated state that can be effectively used to fabricate efficient non-doped OLEDs. Some examples of TPE-based AIEgen structures are shown in **Figure 3**. With subtle structural alteration the emission colors of TPE-based fluorescent AIEgens can be tuned to cover the whole range of visible light. This has been used to construct a number of high performance and highly efficient blue, cyan, green, yellow, red, and even white OLEDs.^{7,9}

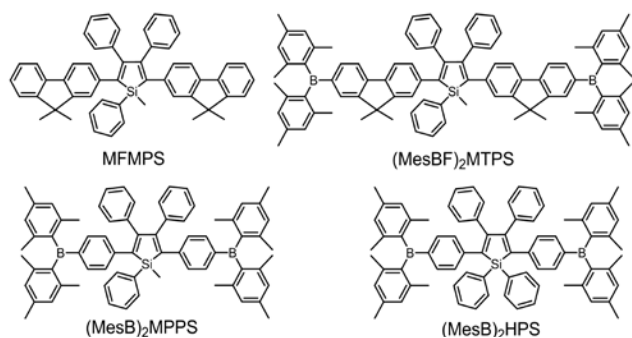


Figure 2. Chemical structures of silole-based AIEgens.

Table 1. Electroluminescent performances of representative devices.

Emitter	Active Layer in Device	λ_{EL} (nm)	CIE	V_{on} (V)	L_{max} (cd m ⁻²)	$\eta_{C,max}$ (cd A ⁻¹)	$\eta_{P,max}$ (lm W ⁻¹)	$\eta_{ext,max}$ (%)	Ref.
MFMPs	NPB (60 nm)/MFMPs (20 nm)/TPBi (40 nm)	544	0.37, 0.57	3.2	31,900	16.0	13.5	4.8	10
MFMPs	MoO ₃ (5 nm)/NPB (60 nm)/MFMPs (20 nm)/TPBi (60 nm)	544	0.36, 0.57	3.3	37,800	18.3	15.7	5.5	10
(MesB) ₂ MPPS	NPB (60 nm)/(MesB) ₂ MPPS (60 nm)	520	0.30, 0.56	3.9	13,900	13.0	10.5	4.12	11
(MesB) ₂ HPS	NPB (60 nm)/(MesB) ₂ HPS (60 nm)	524	0.33, 0.56	4.3	12,200	13.9	11.6	4.35	11
(MesBF) ₂ MTPS	NPB (60 nm)/(MesBF) ₂ MTPS (20 nm)/TPBi (40 nm)	554	0.41, 0.56	3.8	48,348	12.3	8.8	4.1	12
MethylTPA-3pTPE	MoO ₃ (10 nm)/NPB (60 nm)/MethylTPA-3pTPE (15 nm)/TPBi (35 nm)	480	0.17, 0.28	3.1	13,639	8.03	7.04	3.99	13
MethylTPA-3pTPE	MoO ₃ (10 nm)/MethylTPA-3pTPE (75 nm)/TPBi (35 nm)	469	0.18, 0.25	2.9	15,089	6.51	6.88	3.39	13
BTPE-PI	NPB (60 nm)/BTPE-PI (20 nm)/TPBi (40 nm)	463	0.15, 0.15	3.2	20,300	5.9	5.3	4.4	14
BTPE-PI	NPB (40 nm)/BTPE-PI (20 nm)/TPBi (40 nm)	450	0.15, 0.12	3.2	16,400	4.9	4.4	4.0	14
TTPEPy	NPB (60 nm)/TTPEPy (40 nm)/TPBi (20 nm)	492	–	4.7	18,000	10.6	5.0	4.04	15
TTPEPy	NPB (60 nm)/TTPEPy (26 nm)/TPBi (20 nm)/	488	–	3.6	36,300	12.3	7.0	4.95	15
2TPATPE	NPB (40 nm)/2TPATPE (20 nm)/TPBi (10 nm)/Alq ₃ (30 nm)	514	–	3.4	32,230	12.3	10.1	4.0	16
2TPATPE	2TPATPE (60 nm)/TPBi (10 nm)/Alq ₃ (30 nm)	512	–	3.2	33,770	13.0	11.0	4.4	16
PDA-TPE	PDA-TPE (65 nm)/Bphen (35 nm)	523	–	2.4	54,200	14.4	14.1	4.5	17
TPA-TPE	TPA-TPE (65 nm)/Bphen (35 nm)	510	–	2.6	48,300	8.3	8.7	3.6	17
PDA-TPE	NPB (40 nm)/PDA-TPE (25 nm)/Bphen (35 nm)	523	–	2.4	53,600	15.9	16.2	5.9	17
TPA-TPE	NPB (40 nm)/TPA-TPE (25 nm)/Bphen (35 nm)	515	–	2.6	58,300	14.3	15.0	4.5	17
TPE-PNPB	NPB (60 nm)/TPE-PNPB (20 nm)/TPBi (40 nm)	516	0.27, 0.51	3.2	49,993	15.7	12.9	5.12	18
TPE-PNPB	TPE-PNPB (80 nm)/TPBi (40 nm)	516	0.25, 0.50	3.2	13,678	16.8	14.4	5.35	18
BTPETTD	NPB (60 nm)/BTPETTD (20 nm)/TPBi (10 nm)/Alq ₃ (30 nm)	592	–	5.4	8,330	6.4	2.9	3.1	20
TPE-TPA-BTD	NPB (80 nm)/TPE-TPA-BTD (20 nm)/TPBi (40 nm)	604	–	3.2	15,584	6.4	6.3	3.5	19
TPE-NPA-BTD	NPB (80 nm)/TPE-NPA-BTD (20 nm)/TPBi (40 nm)	604	–	3.2	16,396	7.5	7.3	3.9	19
TTPEBTTD	NPB (60 nm)/TTPEBTTD (20 nm)/TPBi (40 nm)	650	0.67, 0.32	4.2	3,750	2.4	–	3.7	21

Abbreviations: λ_{EL} = electroluminescence maximum; V_{on} = turn-on voltage at 1 cd m⁻²; L_{max} = maximum luminance; $\eta_{C,max}$ = maximum current efficiency; $\eta_{P,max}$ = maximum power efficiency; $\eta_{ext,max}$ = maximum external quantum efficiency; CIE = Commission Internationale de l'Éclairage coordinates; NPB = *N,N'*-di(1-naphthyl)-*N,N'*-diphenylbenzidine; TPBi = 1,3,5-tris(*N*-phenylbenzimidazol-2-yl)benzene; Bphen = 4,7-diphenyl-1,10-phenanthroline; Alq₃ = Tris-(8-hydroxyquinoline)aluminum. NPB functions as a hole-transporting layer (HTL); TPBi and Bphen serve as an electron-transporting layer (ETL) and a hole-blocking layer (HBL), respectively; Alq₃ functions as ETL; and MoO₃ serves as a hole-injection layer (HIL).

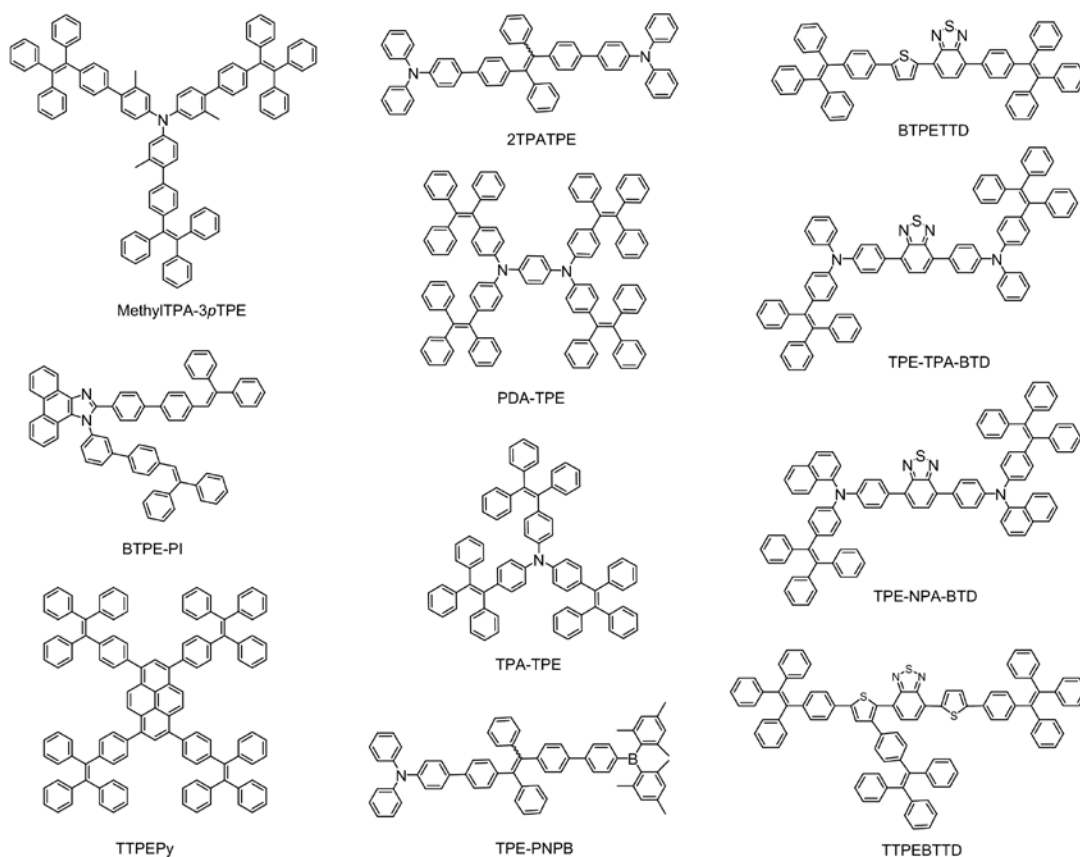


Figure 3. Chemical structures of TPE-based AIEgens.

The development of efficient blue OLEDs, especially deep blue OLEDs, is critical for realizing commercial applications of full-color display and solid-state lighting. However, because of the intrinsic large band gap, robust organic blue light-emitting materials and OLEDs are still rare. Considerable effort has been invested in the development of pure organic blue fluorophores because of the formidable challenges in designing efficient blue phosphors and the difficulty of improving the stability and longevity of the resulting phosphorescent OLEDs. Recently, Li's group has developed a number of blue AIEgens by utilizing different linkage patterns and increasing the intramolecular twisting degrees using steric hindrance to tune the balance between the molecular rotation and conjugation.¹³ Among these AIEgens, MethylTPA-3pTPE, consisting of a methyl-substituted triphenylamine (TPA) core and three TPE units in peripheries, shows a high Φ_f value of 64% in the aggregate state with good EL efficiency. A multilayer OLED with a configuration of ITO/MoO₃ (10 nm)/NPB (60 nm)/MethylTPA-3pTPE (15 nm)/TPBi (35 nm)/LiF (1 nm)/Al radiates blue light at 480 nm (CIE 0.17, 0.28) and presents excellent performance with L_{\max} , $\eta_{C,\max}$, $\eta_{P,\max}$ and $\eta_{\text{ext,max}}$ of 13,639 cd m⁻², 8.03 cd A⁻¹, 7.04 lm W⁻¹, and 3.99%, respectively. While the methyl-substituted TPA group creates good hole-transporting properties for MethylTPA-3pTPE, a simplified device without the HTL, [MoO₃ (10 nm)/MethylTPA-3pTPE (75 nm)/TPBi (35 nm)/LiF (1 nm)/Al], shows comparable EL efficiencies (6.51 cd A⁻¹, 6.88 lm W⁻¹, and 3.39%) and emits bluer light at 469 nm (CIE 0.18, 0.25).

Triphenylethene is another highly useful AIE unit with a very simple molecular structure. Compared to TPE, triphenylethene possesses a shorter conjugation length and exhibits a bluer solid-state emission, making it a promising building block for the fabrication of efficient solid-state blue fluorophores. The melding of triphenylethene with a phenanthro[9,10-d]imidazole (PI) group at the molecular level produces an efficient deep blue AIEgen, BTPE-PI.¹⁴ A non-doped multilayer EL device constructed using BTPE-PI as an emitting layer [ITO/NPB (40 nm)/BTPE-PI (20 nm)/TPBi (40 nm)/LiF (1 nm)/Al (100 nm)] allows for the display of deep blue EL, peaking at 450 nm (CIE 0.15, 0.12) with an outstanding $\eta_{\text{ext,max}}$ of 4.4% and a small efficiency roll-off.

Pyrene (Prod. Nos. 185515 and 571245) is a conventional fluorophore whose film emission is generally weakened as a result of the notorious ACQ effect. Attaching four TPE units to the periphery of pyrene generates a new fluorophore (TTPEPy), which features obvious AIE characteristics and efficient solid-state fluorescence ($\Phi_f = 70\%$).¹⁵ The non-doped OLEDs using TTPEPy as light-emitting layers radiate sky blue emissions with a peak at ~490 nm, while showing excellent performance ($\eta_{C,\max}$ up to 12.3 cd A⁻¹ and $\eta_{\text{ext,max}}$ 4.95%).

In order to use organic semiconductors in an OLED device, emitters should have both efficient solid-state emissions and high carrier-transporting capabilities. Such multifunction materials help simplify device configuration, shorten the fabrication process, and reduce the manufacturing cost because they simultaneously serve as light-emitting layers and hole- and/or electron-transporting layers.⁹ TPA is widely used in semiconductor fabrication due to its good hole-injection/transporting capability, but it suffers from the ACQ effect in the condensed phase. By integrating the TPA groups with the TPE unit, a new and highly versatile semiconductor, 2TPATPE, was prepared.¹⁶ 2TPATPE exhibits not only an extremely high Φ_f value (~100%) but also an excellent hole mobility value of 5.2×10^{-4} cm² V⁻¹ S⁻¹ in solid amorphous film, as determined by time-of-flight technique, a widely used method to measure carrier mobility. A simplified OLED of 2TPATPE without the HTL [ITO/2TPATPE (60 nm)/TPBi (10 nm)/Alq₃ (30 nm)/LiF/Al (200 nm)] was constructed that emits green light with an L_{\max} value of 33,770 cd m⁻² and displays excellent EL efficiencies (4.4%, 13.0 cd A⁻¹, and 11.0 lm W⁻¹), an improvement over devices that include an HTL [ITO/NPB (40 nm)/2TPATPE (20 nm)/TPBi (10 nm)/Alq₃ (30 nm)/LiF/Al (200 nm)] that showed EL efficiencies of 4.0%, 12.3 cd A⁻¹, and 10.1 lm W⁻¹.

Adachi and co-workers developed two novel starburst AIEgens, PDA-TPE and TPA-TPE, by integrating a hole-transporting *N,N,N',N'*-tetraphenyl-*p*-phenylenediamine (PDA) or TPA core with TPE units.¹⁷ The amorphous films of the two AIEgens emit strong fluorescence with high Φ_f values of 56–73% and possess much higher hole mobility than the typical commercialized hole transporter, *N,N'*-di(1-naphthyl)-*N,N'*-diphenylbenzidine (NPB, Prod. No 556696). This is due to the presence of PDA or TPA groups as well as a spontaneous molecular orientation of the star-burst molecules. Hence, the resulting simplified OLEDs in which PDA-TPE or TPA-TPE function both as light-emitting and hole-transporting bifunctional layers perform extremely well (Table 1). Because of the optimal charge balance and the enhanced η_{out} ascribed to the spontaneous molecular orientation, triple-layer devices such as [ITO/NPB (40 nm)/PDA-TPE or TPA-TPE (25 nm)/BPhen (35 nm)/LiF (0.8 nm)/Al (70 nm)] display notably high $\eta_{\text{ext,max}}$ values of up to 5.9% with green EL emissions at 510–530 nm.

Bipolar luminescent materials that contain both electron donors and acceptors (D-A) are preferred materials for balancing the injection and transport of carriers in OLEDs and also help simplify device structure. In an effort to create a more highly efficient solid-state bipolar luminogen, our group designed a new luminogen by connecting an electron donor (diphenylamino) and an electron acceptor (dimesitylboryl) with a TPE unit resulting in a D-A framework with AIE units.¹⁸ This new bipolar AIEgen (TPE-PNPB) exhibits a weak D-A interaction and fluoresces strongly in solid film with a Φ_f value of 94%. The resulting trilayer OLED [ITO/NPB (60 nm)/TPE-PNPB (20 nm)/TPBi (40 nm)/LiF (1 nm)/Al (100 nm)] can be turned on at a low voltage of 3.2 V and radiates a bright EL emission at 516 nm (CIE 0.27, 0.51) with a high L_{\max} of 49,993 cd m⁻². The resulting $\eta_{C,\max}$, $\eta_{P,\max}$ and $\eta_{C,\max}$ values attained from this device were excellent, measuring 15.7 cd A⁻¹, 12.9 lm W⁻¹, and 5.12%, respectively. A remarkably high $\eta_{C,\max}$ of 5.35% is recorded when TPE-PNPB functions both as an EML and HTL in a bilayer OLED, demonstrating that TPE-PNPB is an excellent p-type light emitter. In addition, the $\eta_{C,\max}$ values of 4.75% and 4.45% are maintained at 1,000 cd m⁻² for its trilayer and bilayer OLEDs, respectively, suggesting good stability of OLED based on TPE-PNPB.

For full-color display applications, it will be necessary to develop efficient blue, green, and red fluorescent materials and OLEDs. Like the blue OLEDs, the current performance of existing red fluorescent OLEDs is also unsatisfactory. In general, many traditional red fluorophores are constructed from planar polycyclic aromatic hydrocarbon (PAHs) units with extended π -conjugation. These materials also display a strong ACQ effect, exhibiting weak emission in the solid state.¹⁹ The use of AIE units to develop efficient red fluorophores is emerging as a promising approach to address these shortcomings. For example, a new orange-red fluorophore named BTPETTD, composed of two TPE units tethered to a conjugate of benzo-2,1,3-thiadiazole and thiophene, has been developed.²⁰ BTPETTD shows AIE characteristics and emits efficiently in solid films with a Φ_f value of 55%. OLEDs fabricated using BTPETTD as the light-emitting material exhibited an orange-red EL of 592 nm and high EL efficiencies of 6.1 cd A⁻¹ and 3.1%. Another set of red AIEgens, TPE-TPA-BTD and TPE-NPA-BTD, have also been recently developed.¹⁹ These new materials have high Φ_f values of 48.8% and 63.0%, respectively. The resulting non-doped OLEDs both emit at 604 nm with high $\eta_{\text{ext,max}}$ values up to 3.9%. Moreover, these new red AIEgens possess good hole-transporting characteristics due to the presence of arylamino moieties, and double-layer EL devices using these materials as both EMLs and HTLs also perform well (Table 1). When more TPE units are introduced to the conjugated backbone, the resulting luminogen TTPEBTTD shows a highly twisted conformation, and the intermolecular interactions are greatly suppressed. The solid film of TTPEBTTD emits red PL peaking at 646 nm. High-performance red non-doped OLED is achieved using TTPEBTTD as the light-emitting layer, radiating EL at 650 nm (CIE 0.67, 0.32) and offers an L_{\max} of 3,750 cd m⁻² and a high $\eta_{\text{ext,max}}$ of 3.7%.²¹

Conclusion and Outlook

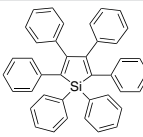
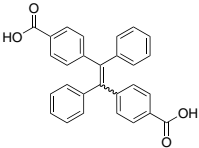
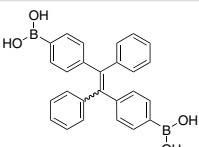
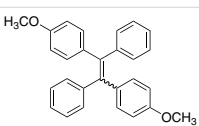
Since the AIE phenomenon was first reported, many fluorescent AIEgens with high Φ_f values in the solid state have been developed for the fabrication of stable and efficient non-doped OLEDs. The emission colors of the devices cover the whole range of visible light. Some of these OLEDs approach or reach the theoretical limit of $\eta_{\text{ext,max}}$ (5–7.5%), several of which have been summarized in this review. A number of high-performance white OLEDs have also been successfully produced using these AIEgens.²² The ability to use the AIE effect to improve common fluorophores (the first-generation luminescent materials) for OLEDs demonstrates the great academic and practical significance of AIE research. However, since 75% of the generated excitons (triplet excitons) have not yet been employed using AIE, there is still much room to improve the efficiencies of fluorescent OLEDs. Much effort has recently been devoted to the creation of third-generation luminescent materials for fabricating efficient OLEDs using pure organic thermally activated delayed fluorescence (TADF) materials. These materials allow the devices to have a large β that can theoretically reach up to 100%, but the efficiency roll-off of these devices is usually severe. Integrating both AIE and TADF effects within a molecule is another promising strategy for constructing increasingly more robust luminescent materials for high-performance OLEDs.

Acknowledgments

We greatly acknowledge financial support from the National Natural Science Foundation of China (51273053), the National Basic Research Program of China (973 Program, 2015CB655004 and 2013CB834702), the Guangdong Natural Science Funds for Distinguished Young Scholars (2014A030306035), the ITC-CNRC14S01, the Guangdong Innovative Research Team Program (201101C0105067115), and the Fundamental Research Funds for the Central Universities (2015PT020 and 2015ZY013).

Aggregation-induced Emission Luminogens

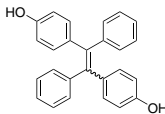
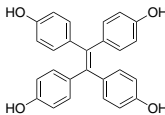
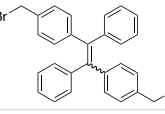
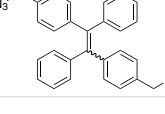
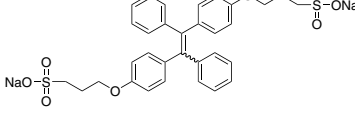
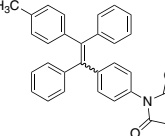
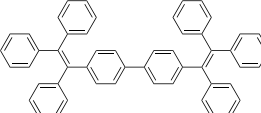
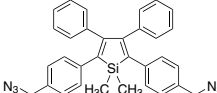
For a complete list of available materials, visit aldrich.com/oled.

Name	Acronym	Structure	Application	Prod. No.
1,1,2,3,4,5-Hexaphenyl-1H-silole	HPS		HPS is an aggregation-induced emission (AIE) material for use in the OLED emitting layer.	797294-25MG
4,4'-(1,2-Diphenylethene-1,2-diyl)dibenzoic acid	TPE-CA		TPE-CA is an aggregation-induced emission (AIE) dye for esterification with hydroxyl and amino groups.	797359-25MG
[(1,2-Diphenylethene-1,2-diyl)bis(4,1-phenylene)]diboronic acid	TPE-BA		TPE-BA is an aggregation-induced emission (AIE) dye for use in Suzuki reaction and D-Glucose detection.	797367-25MG
1,2-Bis(4-methoxyphenyl)-1,2-diphenylethene	TPE-OMe		TPE-OMe is a hydroxy-group protected aggregation-induced emission (AIE) material used in the synthesis of blue mitochondrial dye.	797324-25MG

References

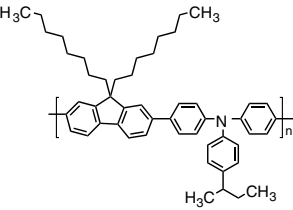
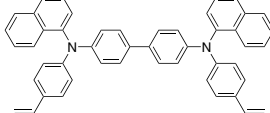
- Zhu, M., Yang, C. *Chem. Soc. Rev.* **2013**, *42*, 4963.
- Liu, M., Li, X.-L., Chen, D.-C., Xie, Z., Cai, X., Xie, G., Liu, K., Tang, J., Su, S.-J., Cao, Y. *Adv. Funct. Mater.* **2015**, *25*, 5190.
- Kaji, H., Suzuki, H., Fukushima, T., Shizu, K., Suzuki, K., Kubo, S., Komino, T., Oiwa, H., Suzuki, F., Wakamiya, A., Murata, Y., Adachi, C. *Nat. Commun.* **2015**, *6*, 8476.
- Hong, Y., Lam, J. W. Y., Tang, B. Z. *Chem. Soc. Rev.* **2011**, *40*, 5361.
- Luo, J., Xie, Z., Lam, J. W. Y., Cheng, L., Chen, H., Qiu, C., Kwok, H. S., Zhan, X., Liu, Y., Zhu, D., Tang, B. Z. *Chem. Commun.* **2001**, 1740.
- Mei, J., Hong, Y., Lam, J. W. Y., Qin, A., Tang, Y., Tang, B. Z. *Adv. Mater.* **2014**, *26*, 5429.
- Mei, J., Leung, N. L. C., Kwok, R. T. K., Lam, J. W. Y., Tang, B. Z. *Chem. Rev.* **2015**, *115*, 11718.
- Zhao, Z., He, B., Tang, B. Z. *Chem. Sci.* **2015**, *6*, 5347.
- Zhao, Z., Lam, J. W. Y., Tang, B. Z. *J. Mater. Chem.* **2012**, *22*, 23726.
- Chen, B., Jiang, Y., Chen, L., Nie, H., He, B., Lu, P., Sung, H. H. Y., Williams, I. D., Kwok, H. S., Qin, A., Zhao, Z., Tang, B. Z. *Chem. Eur. J.* **2014**, *20*, 1931.
- Chen, L., Jiang, Y., Nie, H., Lu, P., Sung, H. H. Y., Williams, I. D., Kwok, H. S., Huang, F., Qin, A., Zhao, Z., Tang, B. Z. *Adv. Funct. Mater.* **2014**, *24*, 3621.
- Quan, C., Nie, H., Hu, R., Qin, A., Zhao, Z., Tang, B. Z. *Chin. J. Chem.* **2015**, *33*, 842. (13)
- Huang, J., Sun, N., Yang, J., Tang, R., Li, Q., Ma, D., Li, Z. *Adv. Funct. Mater.* **2014**, *24*, 7645.
- Qin, W., Yang, Z., Jiang, Y., Lam, J. W. Y., Liang, G., Kwok, H. S., Tang, B. Z. *Chem. Mater.* **2015**, *27*, 3892.
- Zhao, Z., Chen, S., Lam, J. W. Y., Lu, P., Zhong, Y., Wong, K. S., Kwok, H. S., Tang, B. Z. *Chem. Commun.* **2010**, *46*, 2221.
- Liu, Y., Chen, S., Lam, J. W. Y., Lu, P., Kwok, R. T. K., Mahtab, F., Kwok, H. S., Tang, B. Z. *Chem. Mater.* **2011**, *23*, 2536.
- Kim, J. Y., Yasuda, T., Yang, Y. S., Adachi, C. *Adv. Mater.* **2013**, *25*, 2666.
- Chen, L., Jiang, Y., Nie, H., Hu, R., Kwok, H. S., Huang, F., Qin, A., Zhao, Z., Tang, B. Z. *ACS Appl. Mater. Interfaces* **2014**, *6*, 17215.
- Qin, W., Lam, J. W. Y., Yang, Z., Chen, S., Liang, G., Zhao, W., Kwok, H. S., Tang, B. Z. *Chem. Commun.* **2015**, *51*, 7321.
- Zhao, Z., Deng, C., Chen, S., Lam, J. W. Y., Qin, W., Lu, P., Wang, Z., Kwok, H. S., Ma, Y., Qiu, H., Tang, B. Z. *Chem. Commun.* **2011**, *47*, 8847.
- Zhao, Z., Geng, J., Chang, Z., Chen, S., Deng, C., Jiang, T., Qin, W., Lam, J. W. Y., Kwok, H. S., Qiu, H., Liu, B., Tang, B. Z. *J. Mater. Chem.* **2012**, *22*, 11018.
- Liu, B., Nie, H., Zhou, X., Hu, S., Luo, D., Gao, D., Zou, J., Xu, M., Wang, L., Zhao, Z., Qin, A., Peng, J., Ning, H., Cao, Y., Tang, B. Z. *Adv. Funct. Mater.* **2016**, *26*, 776.

Aggregation-induced Emission Luminogens (cont'd)

Name	Acronym	Structure	Application	Prod. No.
4,4'-(1,2-Diphenylethene-1,2-diyl)diphenol	TPE-DOH		TPE-DOH is a synthetic intermediate of aggregation-induced emission (AIE) dye for use in further synthesis of alkyl-halogen to make ether and polymer reaction via esterification.	797219-25MG
4,4''',4''''-(Ethene-1,1,2,2-tetrayl)tetraphenol	TPE-TOH		TPE-TOH is a synthetic intermediate of aggregation-induced emission (AIE) dye for use in further synthesis of alkyl-halogen to make ether via esterification and polymer reaction.	797375-25MG
1,2-Bis[4-(bromomethyl)phenyl]-1,2-diphenylethene	TPE-MB		TPE-MB is an intermediate of aggregation-induced emission (AIE) material used in the synthesis of blue mitochondrial dye for bio-imaging.	797332-25MG
1,2-Bis[4-(azidomethyl)phenyl]-1,2-diphenylethene	TPE-MN3		TPE-MN3 is an aggregation-induced emission (AIE) dye for "Click" reaction.	797340-25MG
Sodium 3,3'-[[[1,2-diphenylethene-1,2-diyl]bis(4,1-phenylene)]bis(oxy)]bis(propane-1-sulfonate)	TPE-Sulfonate		TPE-Sulfonate is an aggregation-induced emission (AIE) dye for bio-imaging and water-based fluorescent probes.	797383-25MG
1-[4-[1,2-Diphenyl-2-(p-tolyl)vinyl]phenyl]-1H-pyrrole-2,5-dione	TPE-Thiol		TPE-Thiol is an aggregation-induced emission (AIE) material for the "Click" chemistry, with alkene and thio group detection.	797316-25MG
4,4'-Bis(1,2,2-triphenylvinyl)-1,1'-biphenyl	BTPE		BTPE is an aggregation-induced emission (AIE) material for use in blue emissive layer for OLED.	797308-25MG
2,5-Bis[4-(azidomethyl)phenyl]-1,1-dimethyl-3,4-diphenyl-1H-silole	Silole-N3		Silole-N3 is a "Clickable" aggregation-induced emission (AIE) material for use in circularly polarised luminescence (CPL).	797286-25MG

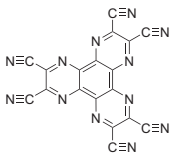
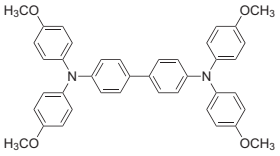
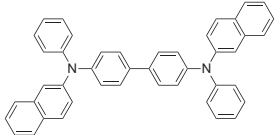
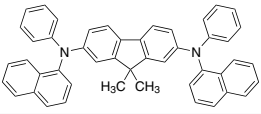
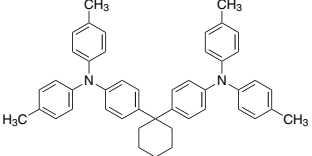
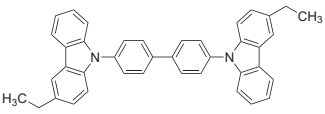
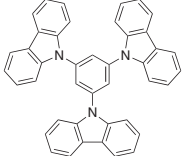
Hole Transport/Injection Layer Materials

For a complete list of available materials, visit aldrich.com/oled.

Name	Acronym	Structure	Purity	Prod. No.
Poly[[9,9-dioctylfluorenyl-2,7-diyl]-co-(4,4'-(N-(4-sec-butylphenyl)diphenyl)amine)]	TFB		-	L512036-250MG
N4,N4'-di(Naphthalen-1-yl)-N4,N4'-bis(4-vinylphenyl)biphenyl-4,4'-diamine	VNPB		-	L512044-250MG

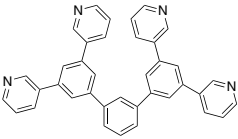
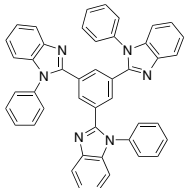
Name	Acronym	Structure	Purity	Prod. No.
N4,N4'-Bis[4-[bis(3-methylphenyl)amino]phenyl]-N4,N4'-diphenyl-[1,1'-biphenyl]-4,4'-diamine	DNTPD		99%	776343-500MG
4,4',4''-Tris[phenyl(m-tolyl)amino]triphenylamine	m-MTDATA		≥99.0%	776327-1G 776327-5G
9,9'-(9,9-Dihexyl-9H-fluorene-2,7-diyl)bis(3,6-di-tert-butylcarbazole)	TBCF		-	771554-500MG
3,6-Bis(3-ethyl-N-carbazolyl)-N-phenylcarbazole	-		99%, HPLC	775878-500MG
9,9'-(9,9-Dimethyl-9H-fluorene-2,7-diyl)bis-9H-carbazole	DMFL-CBP		98%	768766-500MG
4,4',4''-Tris[2-naphthyl(phenyl)amino]triphenylamine	2-TNATA		97%	768669-1G
9,9'-[1,1'-Biphenyl]-4,4'-diylbis[3,6-bis(1,1-dimethyl ethyl)-9H-carbazole]	-		99%	768405-1G
3,6-Bis(N-carbazolyl)-N-ethylcarbazole	-		99%, HPLC	765058-1G
3,6-Bis(N-carbazolyl)-N-phenylcarbazole	BCC-36		99%, HPLC	765031-1G

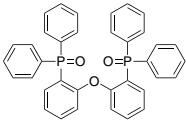
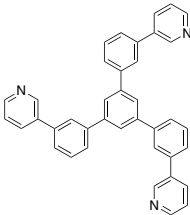
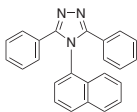
Hole Transport/Injection Layer Materials (cont'd)

Name	Acronym	Structure	Purity	Prod. No.
2,2',7,7'-Tetrakis(<i>N,N</i> -diphenylamino)-9,9-spirofluorene	Spiro-TAD		99%, HPLC	765007-1G
Dipyrazino[2,3- <i>f</i> 2',3'- <i>h</i>]quinoxaline-2,3,6,7,10,11-hexacarbonitrile	HAT-CN6		97%, HPLC	764957-1G
<i>N,N,N',N'</i> -Tetrakis(4-methoxyphenyl)benzidine	MeO-TPD		98%	763497-1G 763497-5G
<i>N,N'</i> -Di(2-naphthyl- <i>N,N'</i> -diphenyl)-1,1'-biphenyl-4,4'-diamine	beta-NPB		99%, HPLC	762903-1G
9,9-Dimethyl- <i>N,N'</i> -di(1-naphthyl)- <i>N,N'</i> -diphenyl-9 <i>H</i> -fluorene-2,7-diamine	DMFL-NPB		98%, HPLC	757314-5G
4,4'-Cyclohexylidenebis[<i>N,N</i> -bis(4-methylphenyl)benzenamine]	TAPC		97%	757284-1G 757284-5G
4,4'-Bis(3-ethyl- <i>N</i> -carbazolyl)-1,1'-biphenyl	Ethyl-CBP		99%, HPLC	757160-1G 757160-5G
1,3,5-Tris(<i>N</i> -carbazolyl)benzene	TCB		97%	752193-1G

Electron Transport/Injection Layer Materials

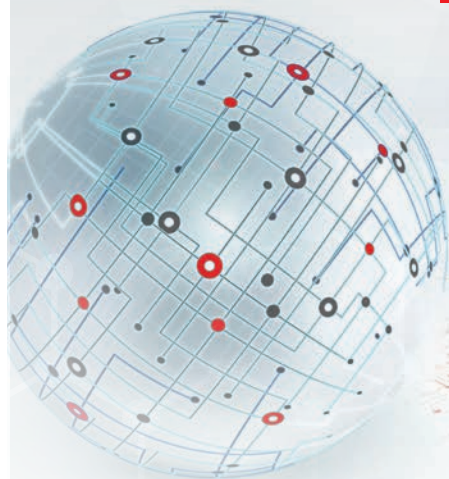
For a complete list of available materials, visit aldrich.com/oled.

Name	Acronym	Structure	Purity	Prod. No.
1,3-Bis(3,5-dipyrid-3-ylphenyl)benzene	B3PyPB		≥99%, HPLC	804886-500MG
2,2',2''-(1,3,5-Benzinetriyl)-tris(1-phenyl-1 <i>H</i> -benzimidazole)	TPBi		≥99.5%, HPLC	806781-500MG

Name	Acronym	Structure	Purity	Prod. No.
Bis[2-(diphenylphosphino)phenyl] ether oxide	DPEPO		98%	805459-5G
1,3,5-Tri(m-pyridin-3-ylphenyl)benzene	TmPyPB		99%, HPLC	790907-1G 790907-5G
3,5-Diphenyl-4-(1-naphthyl)-1H-1,2,4-triazole	TAZ		97%, HPLC	703761-1G

ALDRICH
Materials Science

MATERIALS FOR INNOVATION



ELECTRONICS

Nanowires; printed electronics inks and pastes; materials for OPV, OFET, OLED; nanodispersions; CNTs and graphene; precursors for PVD, CVD, and sputtering

ENERGY

Ready-to-use battery grade electrode and electrolyte materials; nanopowders, nanostructures and dispersions; quantum dots; perovskites; fuel cells and membrane; hydrogen storage materials including MOFs; phosphors; thermoelectrics; high purity salts

BIOMEDICAL

Materials for drug delivery, tissue engineering, and regenerative medicine; PEGs, biodegradable and natural polymers; functionalized nanoparticles; block copolymers, dendrimers and nanoclays

Find more information on our capabilities at

aldrich.com/matsci

BORON NITRIDE NANOTUBES

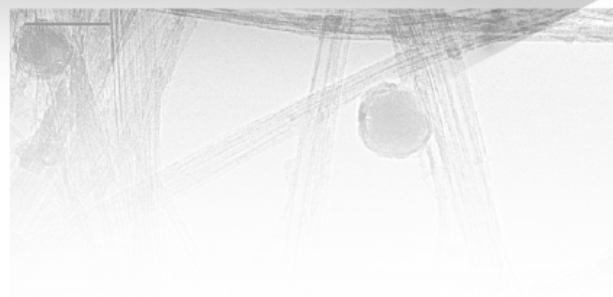
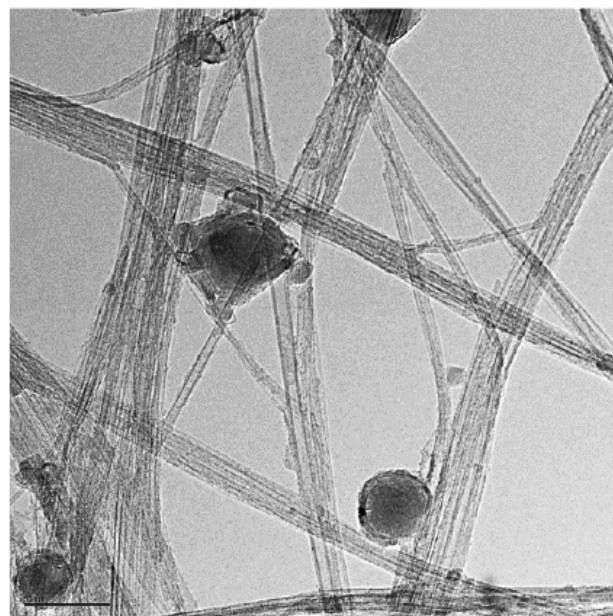
Boron nitride nanotubes (BNNTs) are structural analogs of carbon nanotubes and offer advantages such as:

- High stiffness
- Improved chemical stability
- Enhanced thermal conductivity
- High thermal stability
- Electric field tunable band gap

Applications of BNNTs extend from transparent materials, bulk composites and assemblies, to spintronics, gas adsorption, drug delivery, and diagnostics.

We offer induction plasma-processed BNNTs (Prod. No. [802824](#)) with:

- Diameter of ~5 nm
- Surface area >100 m²/g
- BNNT >50%
- No metal catalyst



For the complete nanomaterials offering, visit
aldrich.com/nano